

# Simulation and Evaluation of the Hydroelastic Responses of a Tidal Current Turbine

A thesis accepted by the Faculty of Aerospace Engineering and  
Geodesy of the University of Stuttgart in partial fulfillment of the  
requirements for the degree of Doctor of Engineering Sciences (Dr.-Ing.)

by

Matthias Michael Arnold

born in Heidelberg

Main referee: Prof. Dr. Po Wen Cheng

Co-referee: Prof. Dr. Tim O'Doherty  
Prof. Dr.-Ing. Kai-Uwe Bletzinger

Date of defense: November 10<sup>th</sup> 2016

Institute of Aircraft Design  
University of Stuttgart

2017



## **ACKNOWLEDGEMENTS**

My work on this thesis was supported by many people and I would like to thank all who helped me, tried to help me and those who didn't even knew that they are helping me. It is only possible to list the most important among those. Namely, I would like to thank my professor Po Wen Cheng and the colleagues at Voith Hydro Tidal Current Technologies, especially Frank Biskup and Raphael Arlitt, for the scientific, engineering and personal guidance. My thanks further goes to the colleagues at Stuttgart Wind Energy and University Stuttgart, to my friends and to my family for the years of personal, logistic and mental support, and finally also to all the students participating in the Tidal Energy research at the University Stuttgart and to the InVentus wind car racing team for a great time together.



---

**TABLE OF CONTENTS**

NOMENCLATURE .....	VII
ABSTRACT.....	XI
ZUSAMMENFASSUNG.....	XIII
1. INTRODUCTION .....	1
1.1. State-of-the-Art for Tidal Current Turbine Hydroelasticity	3
1.2. Aims and Objectives	4
1.2.1 Aims	4
1.2.2 Objectives	4
1.3. Structure of the Thesis	5
2. FUNDAMENTALS OF TIDAL ENERGY.....	7
2.1. Tidal Resources	7
2.1.1 Sea-Water Level	8
2.1.2 Tidal Currents	9
2.2. Tidal Current Turbines	10
2.2.1 Fundamentals of Energy Extraction	11
2.2.2 Design Challenges	13
2.2.3 Turbine Concepts	16
2.2.4 Investigated Turbine System Voith HyTide <sup>®</sup>	18
3. SIMULATION METHODOLOGY .....	21
3.1. State-of-the-Art Hydroelastic Simulation Methods	21
3.1.1 Fluid Simulation Methods	21
3.1.2 Structural Simulation Methods	25
3.1.3 Multi-Physic Simulation Methods	27
3.1.4 Discussion of the Available Hydroelastic-Tools	28
3.2. Fluid-Multibody-Interaction-Method (FMBI)	29
3.2.1 Overview	29
3.2.2 Basis for Communication Interface	32
3.2.3 Structural Translator	33
3.2.4 Fluid Translator	33
3.2.5 FMBI Implementation	39

3.2.6	Summary of the FMBI-Method	41
3.3.	Validation and Verification of the FMBI	42
3.3.1	Methodology of Validation	42
3.3.2	Developed Validation Cases	44
3.3.3	Experimental and Numerical Setup	47
3.3.4	Comparison of the Experimental and Numerical Results	52
3.3.5	Validation of Simpack and CFX for Tidal Turbines	55
3.4.	Summary of Simulation Methodology	57
4.	HYDROELASTIC SIMULATIONS .....	59
4.1.	Simulation Setup	59
4.1.1	Fluid Model	59
4.1.2	Structural Model	64
4.1.3	FMBI Model	66
4.2.	Rotor-Foundation-Interaction	67
4.2.1	Simulated Cases	67
4.2.2	Qualitative Analysis of the Flow Field	69
4.2.3	Quantitative Analysis of the Hydrodynamic Loads	73
4.2.4	Impact of Numerical Simplifications	74
4.3.	Impact of Flexibility on Loads	76
4.3.1	Flexible Turbine Motion	76
4.3.2	Simulated Configurations	78
4.3.3	Variation of Drivetrain Flexibility	79
4.3.4	Variation of Blade Flexibility	82
4.3.5	Variation of Fixed-Structure Flexibility	83
4.4.	Operation in Point of Resonance	87
4.4.1	Steady Resonance Operation	87
4.4.2	Transient Ride-Through of Resonance	90
4.5.	Summary of Hydroelastic Results	92
5.	EVALUATION OF THE LOAD REDUCTION POTENTIAL .....	95
5.1.	Assessment of Potential	95
5.1.1	System Damping	96
5.1.2	Geometric Modifications	99
5.1.3	Operational Modifications	100

---

5.2. Underspeed Controlled Operation	100
5.2.1 Controller Concept	101
5.2.2 Discussion of Stability	103
5.2.3 Operational Loads	107
5.2.4 Performance Evaluation of the Underspeed Controller	110
5.3. Hydroelastic Behavior with the Underspeed Controller	112
5.3.1 Simulation Setup	113
5.3.2 Hydroelasticity in Stall	113
5.4. Discussion of the Conceptual Strategy	116
6. CONCLUSIONS .....	117
6.1. Summary	117
6.2. Future Work and Recommendations	119
6.3. Concluding Remarks	120
REFERENCES .....	121
LIST OF PUBLICATIONS .....	129
LIST OF FIGURES .....	131
LIST OF TABLES .....	137
APPENDIX A) DETAILS ON THE IMPLEMENTATION OF THE FMBI .....	139
APPENDIX B) DERIVATION OF EQUATIONS .....	145
CURRICULUM VITAE .....	151





---

**NOMENCLATURE**

$a$	$[m/s^2]$	Acceleration
$a_{ax}$	-	Axial induction factor
$a_{tan}$	-	Tangential induction factor
$A$	$[m^2]$	Cross-sectional area
$c_a$	-	Added mass coefficient
$c_d$	-	Drag force coefficient
$c_l$	-	Lift force coefficient
$c_p$	-	Power coefficient $c_p = P/(\rho/2 \cdot A \cdot v_1^3)$
$c_{th}$	-	Thrust force coefficient $c_{th} = F_{thrust}/(\rho/2 \cdot A \cdot v_1^2)$
$c_{th\ blade}$	-	Thrust force coefficient of a single rotor blade
$D$	$[m]$	Rotor diameter
$f$	$[Hz]$	Frequency
$f(s_f)$	-	Spline function along the parameter $s_f$
$F_{()}$	$[N]$	Force at location ( )
$F_{ax}$	$[N]$	Axial force
$F_d$	$[N]$	Drag force
$F_l$	$[N]$	Lift force
$f_{\vec{n}}$	-	Face normal flux
$F_{tan}$	$[N]$	Tangential force
$F_{thrust}$	$[N]$	Axial thrust force
$G_{a \rightarrow b}$	-	Transfer function from $a$ to $b$
$J$	$[kg\ m^2]$	Rotational inertia
$k_p, k_I$	-	Proportional and integral controller gain
$k_t$	$[m^2/s^2]$	Turbulence kinetic energy
$l$	$[m]$	Geometric dimension
$m$	-	Inverse Wöhler-exponent

---

$m_{()}$	[Kg]	Mass at ( )
$\mathbf{M}$	[Kg]	Mass matrix
$M_{()}$	[Nm]	Local bending moment at ( )
$\dot{m}$	[kg/s]	Mass flow
$n$	[rpm]	Speed of revolution
$n_{()}$	-	Number count of ( )
$N_{ref}$	-	Reference number of load cycles
$\vec{p}$	[m]	Location in space
$P$	[W]	Power
$P_{rated}$	[W]	Rated electrical power output
$Q_{()}$	[Nm]	Local torsional load at ( )
$Q_{Hydro}$	[Nm]	Hydrodynamic rotor torque $Q_{Hydro} = \frac{\rho}{2} \cdot A \cdot R \cdot v_1^2 \cdot c_p / \lambda_{TSR}$
$R$	[m]	Rotor radius
$Re$	-	Reynolds number
$r$	[m]	Local radius
$Sr$	-	Strouhal number
$t$	[s]	Time
$t_{chord}$	[m]	Rotor blade chord length
$T_P$	[s]	Wave peak period
$T_{PT_1}$	[s]	Time constant of $PT_1$ -low pass filter
$u, v, w$	[m/s]	Cartesian water velocities
$V$	[m <sup>3</sup> ]	Volume
$v_1, v_2, v_3$	[m/s]	Inflow velocity far ahead, in and far behind the rotor plane on hub height if not otherwise denoted
$v_{tan}$	[m/s]	Tangential velocity component
$x, y, z$	[m]	Cartesian coordinates

**Greek**

$\alpha, \beta, \gamma$	[deg]	Cardan transformation angles
$\vec{\alpha}$	[deg]	Vector of relative rotations
$\alpha_2$	-	Relative inflow angle in rotor plane $\sin(\alpha_2) = v_2/c$
$\alpha_{AoA}$	[deg]	Angle of attack
$\alpha_z$	-	Current shear exponent
$\delta$	-	Damping coefficient
$\Delta\vec{x}$	[m]	Vector of relative deformation
$\Delta\vec{r}$	[m]	Relative position vector
$\varepsilon$	-	Numerical error
$\zeta$	-	Damping ratio
$\theta$	[rad]	Phase shift
$\lambda_A$	-	Eigenvalues respectively poles of $A$
$\lambda_{TSR}$	-	Tip speed ratio $\lambda_{TSR} = 2\pi \cdot n \cdot R/v_1$
$\lambda_{TSR\ opt}$	-	Design point tip speed ratio
$\mu$	[kg/(s m)]	Dynamic viscosity
$\mu_t$	[kg/(s m)]	Turbulent viscosity
$\rho$	[kg/m <sup>3</sup> ]	Fluid density
$\varphi$	[deg]	Rotor blade position in rotational direction, $\varphi = 0^\circ$ at top most
$\omega$	[rad/s]	Natural frequency
$\Omega$	[rad/s]	Rotational speed $\Omega = 2\pi \cdot n$

**Notations**

$d()$	Infinitesimal value of ()
$\overline{()}$	Mean value of ()
$()'$	Disturbance from mean value of ()
$\vec{()}$	Vector of values ()

---

$A$	Matrix of values $A$
$1\Omega, 2\Omega, \dots$	Harmonic excitations as multiple of rotational frequency $\Omega \hat{=} n$ in [Hz]
$DEL()$	Damage equivalent value of $()$
$\sigma()$	Standard deviation of $()$
<b>Locations and Coordinate Systems</b>	
OoP	Blade out-of-plane direction
fore-aft	Axial direction of nacelle motion
Hub	Connection point of main shaft and hub, $x$ in flow direction, $z$ vertical
Tower bottom	Intersection point of tower and seabed, $x$ in flow direction, $z$ vertical
Tower top	Upper end of transition piece, $x$ in flow direction, $z$ vertical

### Abbreviations

BEMT	Blade Element Momentum Theory
BRF	Body Reference Frame
CFD	Computational Fluid Dynamics
DEL	Damage Equivalent Load
DoF	Degree of Freedom
FEM	Finite Element Method
FMBI	Fluid-Multibody-Interaction simulation (defined here as MBS and CFD)
FSI	Fluid-Structure-Interaction simulation (typically with FEM and CFD)
HyTide <sup>®</sup>	Product name of the tidal current turbine device developed by Voith
MBS	Multibody System
SST	Shear Stress Transport turbulence model
TSR	Tip Speed Ratio
Voith	Company Voith Hydro Ocean Current Technologies GmbH & Co. KG within Voith Group

## ABSTRACT

To counter the ongoing climate changes, it is required to find a suitable mix of renewable energies. Among the available technologies for this mix of energies, the tidal current energy has a unique character. The timing and amount of power production are predictable for a long time in advance, while, e.g., wind and solar energy have only a short-term predictability. This dependability is a key feature for a stable and cost effective energy supply. However, tidal current turbines are installed to a harsh, oceanic operating environment, which is quite complex and challenging for the turbine design. Thus, the concepts and technology of tidal current turbines still face large uncertainties. These are intended to be reduced with this thesis.

Due to the physical similarity of wind and tidal turbines, the conceptual design is often similar: A horizontal axis lift-driven open rotor mounted to a nacelle on top of a tower structure. Thus, also experience made in the wind energy research is transferred to tidal energy. Yet, due to the high fluid and power density, the resulting turbine geometry differs significantly from a wind turbine and is much sturdier. Subsequently, the structural response and interaction with the fluid loading will differ. This leads to the central question of this thesis, whether the design assumption of wind turbines that the rotor blades and the tower dominate the aeroelastic response is also applicable for the hydroelastic response of a tidal turbine and if not, which components are relevant and how to identify them.

This question is addressed here in three steps with numerical simulations of the hydroelastic response of a tidal current turbine. In the first step, a simulation methodology is developed based on coupled CFD and multibody methods. In the second step, this toolchain is applied to the Voith HyTide<sup>®</sup> 1MW-tidal current turbine, which is used here as an exemplary turbine design, with varying levels of detail in the structural model. The thesis then concludes with an evaluation of the simulation results and the potential for optimization in the third step.

A literature review of the current state-of-the-art on simulation of tidal current turbines shows two central strategies: Either high-fidelity methods, e.g. CFD and FEM, are applied to investigate single components, or semi-empirical methods are used to simulate the turbine on a system level, relying on the assumptions from wind energy. Neither of these methods is suitable to identify the components relevant for the hydroelastic response. Thus, a new coupling methodology is developed within this thesis, connecting the CFD tool Ansys CFX and the multibody code Simpack bi-directional and implicit – the fluid-multibody-interaction

(FMBI) method. This setup is able to simulate the complete system of a tidal current turbine with a high enough level of detail and reasonable resources. In a follow-up step, the FMBI is successfully validated with a set of pendulum experiments, each optimized to validate a single section of the developed coupling code. The method can therefore be used to evaluate the components within a tidal current turbine with respect to their impact on the hydroelastic response.

In the second step, a model of the Voith HyTide<sup>®</sup> 1000-13 turbine is set up and analyzed in the FMBI toolchain. First, this analysis investigates the hydrodynamic properties of the rigid turbine to identify relevant vortex structures and load cases. The most severe point of operation is then investigated further with the maximal rotational speed at cut-out current velocity and operation in tower shadow. For this point of operation, the configurations of component flexibilities are varied strategically to identify the individual and combined impact of the tower, rotor blades, nacelle, main shaft, etc. on the hydroelastic response and loads. It can be summarized from the evaluation of these simulations that the tower and nacelle bending modes dominate the hydroelastic response. Often, only the rotor blades' flexibility is considered in literature. However, it is shown here that the flexibility of the rotor blades has a marginal impact on the hydroelasticity in case of the Voith HyTide<sup>®</sup> turbine, due to the high stiffness in the design of this device. The investigation of the hydroelastic responses concludes then with the simulation of additional points of operation in resonance of the tower structure. These results show that resonance can cause up to five times higher loads compared to a rigid configuration, but has only local effects and does not necessarily cause high loads on the full system.

In the last part of this thesis, the hydroelastic response is evaluated with respect to improvements in the conceptual design of the turbine. Here, the control strategy is found to be of the highest significance and a conceptual change from the current overspeed power limitation to an underspeed controller is recommended. The required controller algorithms are introduced and show an estimated system mass reduction of at least 13% in an initial performance analysis.

This thesis investigates the hydroelastic response of a tidal current turbine, offers a basis for future developments and simulation studies by identifying the tower and nacelle to be the most relevant components for the hydroelasticity, and introduces the underspeed controller as conceptual strategy for future turbines.

---

## ZUSAMMENFASSUNG

Um die Änderungen im weltweiten Klima zu bremsen, ist es dringend erforderlich eine sinnvolle Mischung erneuerbarer Energiequellen zu finden. Unter den verfügbaren Technologien hat die Gezeitenenergie dabei ein Alleinstellungsmerkmal. Im Gegensatz z.B. zur Wind- oder Solarenergie, die von einer stochastischen Umgebung abhängig sind, ist die Energieproduktion der Gezeitenströmungsenergie langfristig planbar – eine entscheidende Voraussetzung für eine zuverlässige und günstige Energieversorgung. Die Betriebsumgebung für Gezeitenenergie ist dabei jedoch komplex, wenig erfasst und stellt große Ansprüche an den Entwurf von Gezeitenströmungsturbinen. Die daraus resultierenden Unsicherheiten bei der Entwicklung sollen mit der vorliegenden Arbeit reduziert werden.

Wegen der physikalischen Ähnlichkeit in der Energiewandlung von Wind- und Gezeitenströmungsturbinen wird meist der gleiche Ansatz des horizontalachs-Auftriebsläufer-Rotors an einer Gondel auf einer Turmstruktur eingesetzt. Dementsprechend werden auch Erfahrungen aus der Windenergieforschung auf die Gezeitenströmungsenergie übertragen. Allerdings muss die Geometrie der Anlage durch die deutlich höhere Wasser- und Leistungsdichte stämmiger gebaut werden. Daraus ergibt sich die zentrale Frage dieser Arbeit, ob die Entwurfsannahme der Windenergie, dass der Turm und die Blätter die Aeroelastizität dominieren, auf die Hydroelastizität von Gezeitenströmungsturbinen übertragbar ist, bzw. welche Komponenten relevant sind und wie sie identifiziert werden können.

Diese Frage wird hier mit numerischen Simulationen des hydroelastischen Verhaltens in drei Schritten angegangen. Zunächst wird eine Simulationsmethodik basierend auf gekoppelten CFD und Mehrkörpersystemen entwickelt. Diese wird dann im zweiten Schritt auf die hier exemplarisch betrachtete Voith HyTide<sup>®</sup> 1MW Gezeitenströmungsturbine angewandt und mit variierender Detaillierungstiefe im Strukturmodell simuliert. Im dritten Schritt werden die Ergebnisse dieser Simulationen hinsichtlich des Optimierungspotentials ausgewertet.

Eine Betrachtung des Entwicklungsstandes in der Literatur zeigt, dass bislang grundsätzlich zwei Ansätze von hydroelastischen Simulationen zum Einsatz kommen: Entweder werden hochauflösende, rechenintensive Methoden wie gekoppelte CFD und FEM Methoden eingesetzt, um einzelne Komponenten zu analysieren, oder es kommen semi-empirische Verfahren auf Systemebene zum Einsatz, die aus den Annahmen der Windenergie abgeleitet wurden. Keine dieser Methoden ist jedoch sinnvoll geeignet, um die für die Hydroelastizität

relevanten Komponenten zu identifizieren. Daher wird hier ein neues Verfahren basierend auf einer impliziten, starken Kopplung des CFD-Programms Ansys CFX und der Mehrkörper-simulationsumgebung Simpack entwickelt – die Fluid-Multibody-Interaction Methode (FMBI). Dieser Ansatz ermöglicht es, das gesamte System der Gezeitenströmungsturbine mit ausreichend hoher Auflösung bei akzeptablem Ressourcenaufwand zu simulieren. Validiert wird die FMBI durch den Vergleich mit experimentellen Daten aus speziell entwickelten Pendelexperimenten.

Im zweiten Schritt wird ein Model der Voith HyTide<sup>®</sup>1000-13 Turbine in der FMBI aufgebaut und simuliert. Zunächst werden dabei die hydrodynamischen Eigenschaften der Anlage anhand eines Starrkörper-Models betrachtet, um relevante Wirbelstrukturen und Lastfälle zu identifiziert. Der Betrieb im Turmnachlauf mit höchster Drehzahl bei Abschaltgeschwindigkeit stellt dabei den kritischsten dar und wird exemplarisch im Weiteren näher betrachtet. Durch die gezielte Kombination von flexiblen und starren Komponenten wird der individuelle und kombinierte Einfluss des Turms, der Rotorblätter, der Gondel, der Hauptwelle, etc. auf die Hydroelastizität bewertet. Aus dieser Studie ergibt sich, dass die Biegemoden des Turms und der Gondel das hydroelastische Verhalten dominieren. In der Literatur werden zwar zumeist nur die Rotorblätter als flexibel betrachten, diese haben jedoch für die Voith HyTide<sup>®</sup> Turbine nur einen minimalen Einfluss auf die Lasten, was auf die hohe Steifigkeit der Blätter zurückzuführen ist. Um außerdem den Einfluss des Betriebspunktes zu bewerten, wird die Untersuchung abschließend um Betriebspunkte im Bereich der Turmresonanz erweitert. Hierbei ergibt sich eine Überhöhung der Lasten um bis zu das fünf-fache im Vergleich zum Starrkörper-Model. Dies wirkt sich jedoch nur lokal, nicht aber auf das Gesamtsystems aus.

Im letzten Teil der Arbeit wird das Optimierungspotential bewertet, das sich aus den Erkenntnissen zur Hydroelastizität ergibt. Dabei wird insbesondere die Regelungsstrategie als mögliche Verbesserung identifiziert, bei der von der aktuellen Überdrehzahlregelung auf einen Unterdrehzahlansatz gewechselt werden sollte. Dieser bietet, wie durch Laststudien gezeigt wird, ein Potential zu einer Massenreduktion der Anlage von mindestens 13%.

Die vorliegende Arbeit untersucht die Hydroelastizität an Gezeitenströmungsturbinen, stellt durch die Identifikation der Flexibilität des Turms und der Gondel als Haupteinfluss auf die Lasten die Basis für zukünftige Weiterentwicklungen und Simulationsstudien dar und führt die Unterdrehzahlregelung als Konzeptstrategie für zukünftige Turbinen ein.



## 1. INTRODUCTION

Covering over 70% of the earth's surface, the oceans have a high potential to be the source of the world's power supply in the future. However, the oceans have only been used on a minor scale up to now. The largest utilizations as energy source are the offshore wind turbines collecting energy above the sea's surface and the offshore oilrigs pumping deposits from below the seabed. Neither uses the ocean itself as a source, but only passes through the water with their foundations and pipes to set up the required devices. However, research has shown that the water contains a vast amount of energy, inducing high loads on any device installed offshore.

Analyzing this energy in the water and identifying the frequencies, Fig. 1-1 shows that ocean energy can be split in different types. Each peak in the spectrum has its own origin and its potential use as an energy source can be evaluated. Turbulence, caused by viscosity and currents, has the highest frequencies in this spectrum and is followed by waves. Waves are caused by the fetch of the wind on the sea surface and have a limited penetration depth to the ocean. The next three peaks in the spectrum form the group of tidal resources with semi-diurnal (twice a day) and diurnal (once a day) variations, and moon phases caused by the rotation of the earth and the gravity of the moon and sun, visible as ebb and flood. All longer periods refer to the climate, like long-term cycles due to thermal and salinity balances.

Despite the fact that each of those peaks represents significant energy potentials, only a few can be extracted from a technical point of view. The response time of the power extraction device must be of the same order of magnitude, or faster than the frequency of the energy source. Therefore, the size of the device must match the source, i.e. for a higher frequency, the device must be smaller. As with the device size, power output and cost per device also vary, the technical and economic use is limited to wave energy, tidal energy on the diurnal and semi-diurnal peak and to a lower extent ocean thermal energy with its very long periods. Ideas have been found for the remaining peaks, but the technologies are in an early stage of development and are far from commercial application.

The research on ocean energies has gained significant momentum in the past decade. However, it is interesting to observe that the ocean energies research community is becoming increasingly split into two groups: While wave energy is dominated by academia and startup companies, tidal energy development is mainly driven by heavy industry and energy

companies. The reasons for this can be explained by the nature of the two technologies: Wave energy devices are typically smaller and the technical concepts are widespread, allowing for academic curiosity. However, they operate in a stochastic environment associated with high investment risks. Tidal energy devices, on the other hand, are typically larger and installed in a more challenging environment, but harvest a predictable energy source. Furthermore, the concepts are much more predetermined due to the same energy extraction principles. This reduces the risks, while the investment is typically larger.

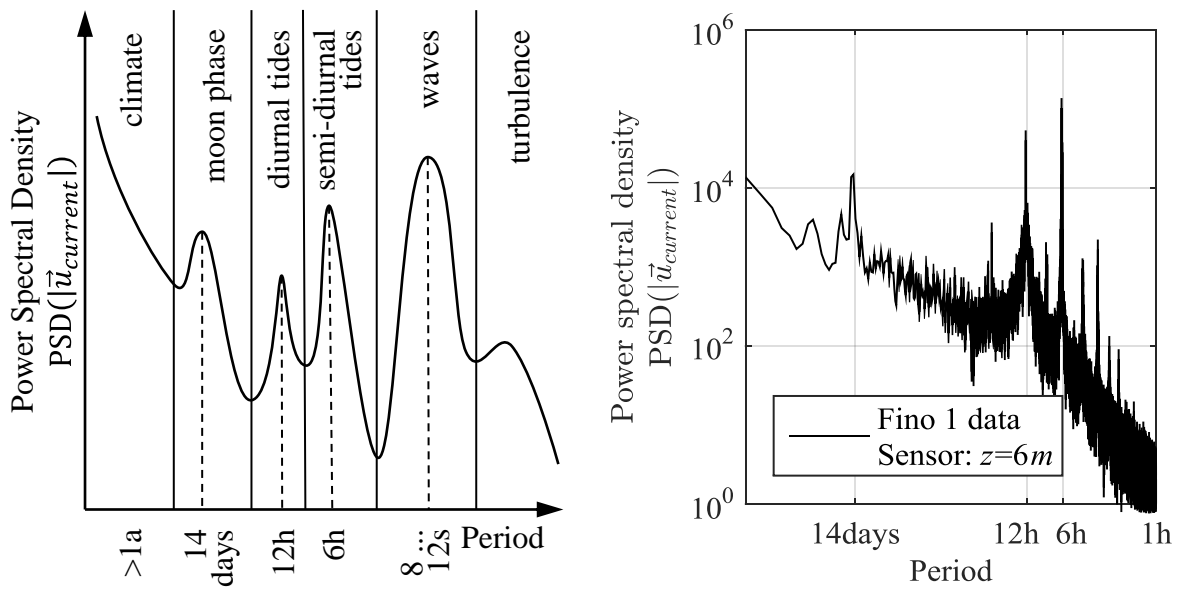


Fig. 1-1: Spectrum of the absolute value of current velocity  $|\vec{u}_{current}|$  sketched (left) and based on measured data from the Fino 1 met mast, [20] (period: 02.2004–12.2006, resolution: 10 minutes, missing data interpolated)

This thesis investigates the hydroelasticity of tidal current turbines. Tidal current energy and turbines are a subtype of tidal energy, extracting the kinetic energy inherent to mass displacements of ebb and flood. This type of device is also often referred to as ‘under water wind turbine’, as the underlying principle and the basic design are similar to wind turbines. However, they have the advantage of a higher predictability of the energy resource compared to wind energy at the cost of the disadvantage of operating in a more challenging environment. Due to this issue, the design of tidal current turbines still faces large uncertainties in the environmental conditions and the turbine development aspect. The interaction of elastic flexibilities of tidal current turbines with the surrounding flow, the hydroelasticity, especially requires further research.

## 1.1. State-of-the-Art for Tidal Current Turbine Hydroelasticity

In literature, two types of investigations on hydroelasticity can be found: On the one hand, detailed analyses of single components and load cases with high fidelity methods, and on the other hand, analyses of the full system with simplified methods for stochastic load cases. Some examples of the previous results are discussed here. The state-of-the-art methods applied will be detailed in Section 3.1.

The high fidelity methods are usually used to investigate ultimate load case scenarios. Often these investigations are focused on the rotor blades and use uni- or bi-directional coupled finite element methods (FEM) and computational fluid dynamics (CFD) or blade element momentum theory (BEMT). E.g., [42] used this approach to analyze the material strain within a rotor blade. [38] applied the same method to calculate the strain on the foundation. In difference to that, [57], [62] and [79] focused their analysis on the impact of the hydroelastic deformations and analyzed the changes in power production and thrust. This type of analysis was extended by [32] from the single blade to the rotational speed of the rotor system. However, all these investigations examined only a single component each, or a rigid set of components, based on the assumption that these are critical.

The other type of investigations considers the tidal current turbine as a full system. All of these analyses try to simplify the structural and hydrodynamic description to the bare minimum. To do so, they claim that the experience from wind energy can be transferred, [51], and use the same assumptions regarding the minimal requirements to the model. E.g., [15] and [89] apply the engineering tool Tidal Bladed, which describes the turbine dynamics with the tower and blade flexibility, to evaluate the stochastic and fatigue loads on a tidal current turbine. The same type of simulation is also used by, e.g., [1] to derive identification criterions for a rotor blade failure.

By comparing all those investigations, a missing link can be identified. For the simplified models, assumptions regarding the required level of detail are made. These are often transferred from wind turbine designs, due to the similarity of technology. However, the structural properties of wind and tidal turbines differ. Nevertheless, the fact that tower and rotor blades dominate the aeroelasticity on wind energy systems is taken as an assumption for the design of tidal current turbines. Investigations, which prove this assumption for tidal energy, are yet missing.

On the other end of the missing link, the high fidelity methods are limited to single components. These single components are chosen, similar to the simplified methods, based on the experience from wind energy. Thus, often only the rotor blade is investigated for hydroelasticity. However, it is yet to be shown that the rotor blade is the most relevant component. A first step into expanding the research to the full turbine was done by [81], showing the hydroelastic response with a coupled CFD and FEM model. However, this investigation still considers only a geometrically simplified setup and does not distinct between the different components of the turbine.

The here presented research closes this missing link by extending the high fidelity methods to a full system analysis. This is previously only done with the assumptions of simplified methods. With the results of this analysis, both the assumptions for the simplified system analysis and the scope of investigation for the high fidelity methods can be challenged and their applicability shown. This research therefore narrows the missing link between the two types of state-of-the-art hydroelastic investigations and is thus a further step towards a full understanding of tidal current turbines.

## **1.2. Aims and Objectives**

### **1.2.1 Aims**

The aim of this research is to increase the understanding of loads on a horizontal axis tidal current turbine by analyzing the hydroelastic response of the full system and narrowing it down to the key components to determine loads based on fluid-structure-interaction simulations.

### **1.2.2 Objectives**

This thesis has four main objectives. Each contains several work packages (WP), which are sketched here:

Objective 1: Tool development:

WP 1.1 Analyze the requirements to the simulation tools for the present application.

WP 1.2 Develop and validate a toolchain able to simulate the required level of detail with adequate resources.

Objective 2: Model development:

- WP 2.1 Create a structural and a hydrodynamic model of the tidal turbine including all required details and enable it for variations of structural properties.
- WP 2.2 Analyze the baseline behavior of the rigid turbine and identify a representative design driving load case for a detailed investigation.

Objective 3: Hydroelastic-Simulations:

- WP 3.1 Combine the structural and hydrodynamic model with the toolchain and perform hydroelastic simulations with varying combinations of flexibility.
- WP 3.2 Compare the results of the hydroelastic simulations and identify the components in the turbine with the highest impact on the loads based on their flexibility.
- WP 3.3 Evaluate the loads on further cases as necessary.

Objective 4: Conceptual Strategy:

- WP 4.1 Analyze the potential of conceptual strategies for load reductions based on the hydroelastic results and suggest structural, geometric and operational changes to the turbine design.
- WP 4.2 Evaluate the suggested changes regarding load reduction.

### **1.3. Structure of the Thesis**

The present document is structured according to the objectives given above. Initially in Section 2, the tidal energy and the physical properties and limitations of tidal current turbines are reviewed. Here the environmental conditions as well as the basics of the energy extraction are detailed. The energy extraction can be achieved with different conceptual approaches which are presented to classify the Voith HyTide<sup>®</sup>1000-13 turbine design investigated in the present research.

Section 3 is used to develop the toolchain. The requirements and results of state-of-the-art tools are analyzed, WP 1.1, and it will be shown that for the present application a combination of multibody methods and CFD is the most suitable one. The coupling of those tools is developed and implemented here, WP 1.2. This section closes with the validation of the developed fluid-multibody-interaction (FMBI) based on free decay experiments.

Section 4 starts with the model setup within each of the single tools based on the required sub-models, WP 2.1. The overview of the hierarchical structure of these models and its possibilities for variations in, e.g., the flexibilities is presented in Subsection 4.1.

Subsection 4.2 continues then with the simulation of the hydrodynamics of the rigid turbine to identify fluid effects like tower shadow and vortex structures, and evaluate them regarding their impact on the loads, WP 2.2. Based on the previously set up model and toolchain this is followed in Subsection 4.3 by simulations of the turbine with the combined fluid and structural model to identify the hydroelastic response, WP 3.1. This subsection also contains the result for a variation of flexible components, e.g. tower flexible and blades rigid, or main shaft and blades flexible. The results of these simulations are then compared to identify the impact of each component and find a ranking of the relevance of flexibility, WP 3.2. Section 4 ends with an extension to further operational points in Subsection 4.4 to evaluate the severity of possible resonance operation, WP 3.3.

Section 5 evaluates the results of the previous sections regarding optimization potential. As these evaluation results show that the highest potential is to avoid the resonance points of operation rather than optimizing the structure, WP 4.1, a conceptual change of the controller strategy is suggested. This strategy is developed and the stability is proven. This section then goes back into the hydroelastic simulations to evaluate the changes in the hydroelastic behavior due to the evolved concept, WP 4.2.

All results and recommendations of the thesis are summarized in the conclusion in Section 6.

## 2. FUNDAMENTALS OF TIDAL ENERGY

This chapter introduces the tidal energy by summarizing the origin of tides and a discussion of the fundamental physics of a tidal current turbine and its engineering challenges. From these challenges and their state-of-the-art solutions, three conceptual categories of tidal current turbines are deduced to classify the here investigated Voith HyTide<sup>®</sup> turbine concept with respect to competitive designs.

### 2.1. Tidal Resources

As it has been already mentioned in the introduction, the tides are a result of the gravity of the moon to earth. The balance of gravitational and centrifugal forces of the rotating earth-moon-system and the hydrostatic pressure forms two regions of increased water level, Fig. 2-1. These are called the lunar tides.

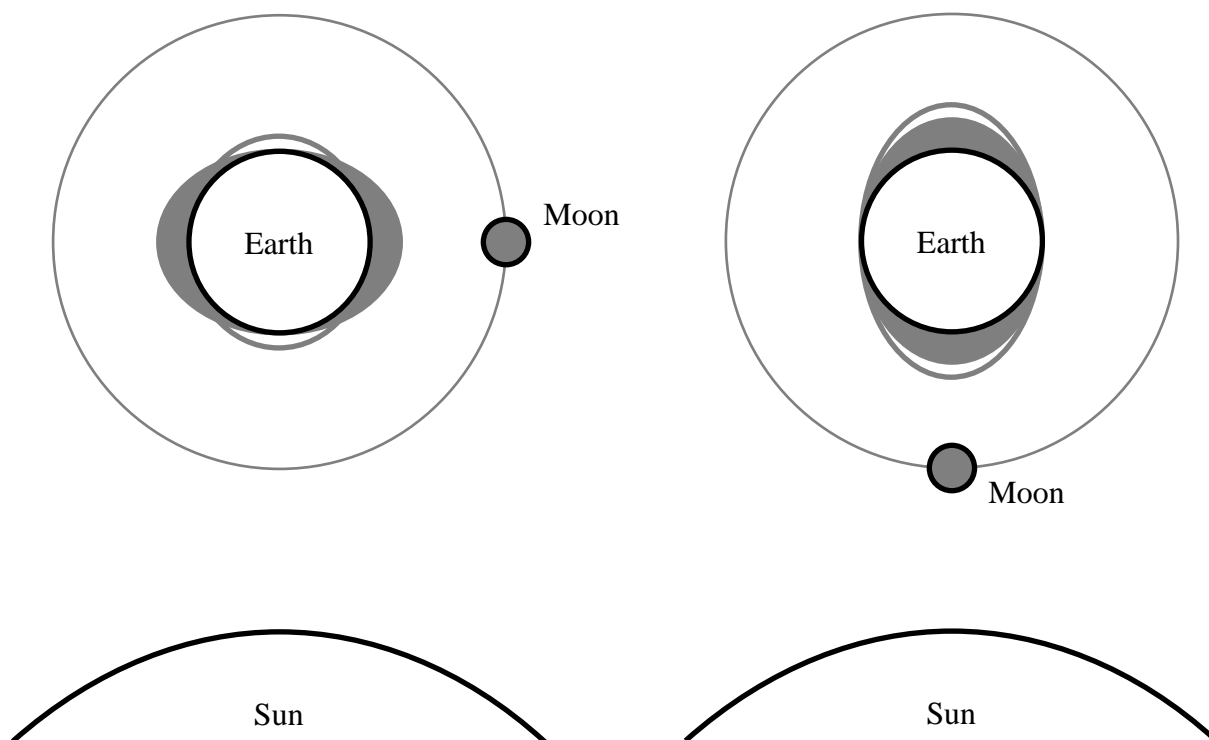


Fig. 2-1: Lunar tide (grey) and solar tide (white) due to earth-moon-sun alignment

The earth rotates relative to those flood regions, causing two ebb and flood cycles per day with different amplitudes. A similar system of ebb and flood, the solar tides, are caused by the sun. Based on the moon phases, the solar and lunar tides form a constructive or destructive interference. This results in bi-weekly variations in the tidal amplitude, the spring and neap

tide. In theory all other astronomical objects cause additional tides, however their impact is insignificant for most investigations.

### 2.1.1 Sea-Water Level

The two ebb and flood cycles are the theoretical result of semi-diurnal tides based on the assumption of a spherical surface of earth without continents. Obviously, this assumption is incorrect and in practice the tides can not travel around the globe undisturbed. Instead, whenever a lunar or solar tide reaches a coastline it is deflected. As shown in Fig. 2-2 (left), this results in the amphidromic points, which are locations on the ocean without tidal changes in the water level. Around each of those points, the tides circle as a standing wave in either clockwise or counter-clockwise direction, [70].

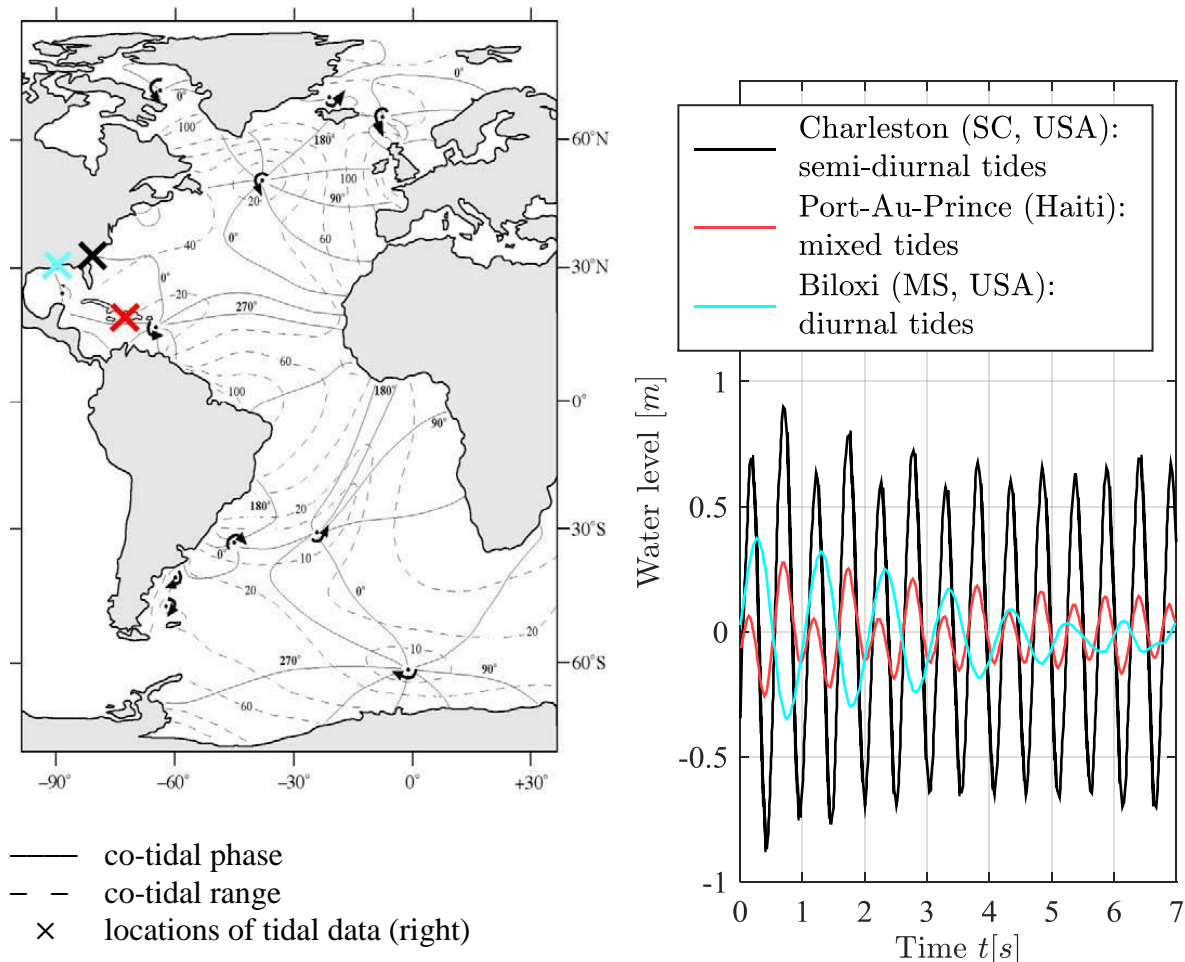


Fig. 2-2: Co-tidal map of Atlantic ocean, [62], and tidal data for three exemplary locations for 1<sup>st</sup> till 7<sup>th</sup> Nov 2015, reproduced from [63]



This behavior is frequency dependent, as the standing wave response of, e.g., an inlet or a coastline changes with the frequency. Therefore, different amphidromic points exist for solar and lunar tides. The combination of those sets of amphidromic points results in large local deviations in magnitude and shape of the tides. Fig. 2-2 (right) shows the tides for three locations on the North American east coast with semi-diurnal, mixed and diurnal tides. Retrieving Fig. 1-1, this means that the intensity of the semi-diurnal and diurnal peaks vary and either of them might even vanish under ideal conditions depending on the location.

This potential energy could be used directly for tidal energy production by building a dam or barrage, e.g., on the entrance of an estuary, which causes a water level difference on the both sides. The resulting pressure difference can then be transformed with ultra-low-head water turbines to electrical energy. However, the required large dam causes, among other issues, a change in the amplitude of the tides in the estuary. This can result in significant adverse impacts on the ecosystem. Therefore, this type of technology is considered outdated, despite its high potential for energy production, and not discussed further here.

### **2.1.2 Tidal Currents**

Tides are as any other mass displacement coupled to a velocity and kinetic energy. In case of tides, this results in large site dependent current velocities with typically two dominant directions associated to ebb and flood respectively. These currents can be used for energy extraction with tidal current turbines and will be detailed below.

Extracting the kinetic energy from tides with tidal current turbines requires sufficiently high current velocities. However, locating a possible site for this type of tidal energy is delicate, due to the difficult measurements. Compared to wind with its worldwide network of weather stations with permanent measurement equipment, no such wide spread system exists for tidal currents. Tidal current measurements are conducted on selected locations for a selected period only. The sole basis for site assessment is subsequently often the tidal table of nearby harbors giving the amplitude of tides. High amplitudes indicate possible locations for tidal current energy nearby, but the currents are highly dependent on the local bathymetry.

Aerial surveys can be used to solve this issue of localizing sites, Fig. 2-3. Due to the hydrodynamic wave-current interaction, the waves on the sea-surface are influenced by changes in the current velocities. Thus, local increases and decreases in the current velocity are visible as darker or lighter areas on an aerial image. Nevertheless, this method of site

assessment requires much experience and is only possible with suitable weather conditions. Therefore, it is extended with simulations. These depend on sufficient data of the local bathymetry and tides, as well as computational resources. To compensate for the inherent numerical uncertainty, the final step in a site assessment is the costly placement of a measurement device to evaluate the potential at the specified position of the planned tidal current turbine.

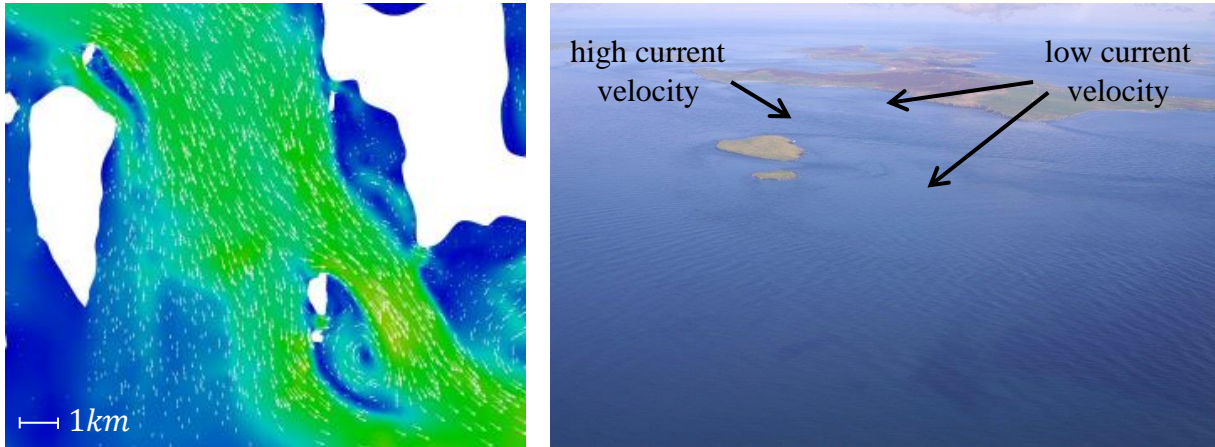


Fig. 2-3: Current velocity in Fall of Warness, Orkney, from simulation (left), [71], and aerial view on Muckle Green Holm Island in south-east of simulation (right), [28]

Furthermore, the current speed and its direction at a site are not the only parameter, which have to be taken into account. Additionally, political, economic and ecological issues need to be considered; i.e. the space in the oceans is allocated to several parties, including fishery, ship travels, environmental protection zones, military, etc. and none of them is eager to pass on a part of its share to the ‘newcomer’ tidal current energy.

Due to this difficult procedure of site assessment, the worldwide potential of tidal current energy is still unknown. Predictions of the potential range from at least  $25GW$ , [3], over  $135GW$ , [50], up to several hundred  $GW$ , rising with the knowledge and state-of-the-art of tidal current energy. Comparing this to the world electricity consumption of about  $2400GW$ , tidal current energy could be a worthy contributor of renewable energy.

## 2.2. Tidal Current Turbines

Due to the similarity of wind and tidal currents, the technology of wind turbines and tidal current turbines are based on the same energy extraction principle. However, the design of tidal turbines faces a list of additional design challenges, which need to be addressed. The

following subsection discusses the engineering basics and challenges for tidal current turbines. Furthermore, it introduces the Voith HyTide<sup>®</sup> turbine concept, which is investigated in this research.

### 2.2.1 Fundamentals of Energy Extraction

The kinetic energy in the current is bound to the current velocity. Extracting energy from the currents with a device of yet unspecified shape and type reduces this velocity. Based on the inviscid stream tube concept, this velocity variation ranges from  $v_1$  far ahead of the device to  $v_3$  far behind the device, Fig. 2-4, and is described by the axial induction factor  $a_{ax}$ , (2-1).

$$a_{ax} = \frac{v_3 - v_1}{2 \cdot v_1} \quad (2-1)$$

$a_{ax}$  is a result of the axial thrust force  $F_{thrust}$  according to the change in momentum, (2-2), with the mass flow  $\dot{m}$  passing the device.

$$F_{thrust} = \dot{m} \cdot (v_1 - v_3) \quad (2-2)$$

By applying the Froude-Rankine-Theorem, (2-3), to calculate the velocity in the plane of the device  $v_2$  and with the cross-section of the device  $A$  and the fluid density  $\rho$ , the thrust can be defined as the non-dimensional thrust coefficient  $c_{th}$ , (2-4).

$$v_2 = \frac{v_1 + v_3}{2} = v_1 \cdot (a_{ax} - 1) \quad (2-3)$$

$$c_{th} = \frac{F_{thrust}}{\frac{\rho}{2} \cdot v_1^2 \cdot A} = 4 \cdot a_{ax} \cdot (a_{ax} - 1) \quad (2-4)$$

Similar to the thrust coefficient, also the power extracted by the device  $P$  can be given in a non-dimensional form with the power coefficient  $c_P$ , (2-5).

$$c_P = \frac{P}{\frac{\rho}{2} \cdot v_1^3 \cdot A} = \frac{F_{thrust} \cdot v_2}{\frac{\rho}{2} \cdot v_1^3 \cdot A} = 4 \cdot a_{ax} \cdot (a_{ax} - 1)^2 \quad (2-5)$$

In the momentum analysis this power results directly from the thrust,  $P = F_{thrust} \cdot v_2$ . Optimizing the power results in the Betz optimum, (2-6), [12], the highest possible extraction rate according to the 1-dimensional momentum theory.

$$a_{ax,Betz} = \frac{1}{3} \quad c_{P,Betz} = \frac{16}{27} \quad c_{th,Betz} = \frac{8}{9} \quad (2-6)$$

So far, the energy-extracting device has not been further defined. It could be any type of technology creating an axial thrust force to the fluid. However, the usual approach is a turbine

with lifting airfoils in either planar or axial motion, Fig. 2-5. Typically this motion is caused by a rotation with the rotational speed  $n$  and described with the tip speed ratio  $\lambda_{TSR}$  based on the rotor radius  $R$ , (2-7).

$$\lambda_{TSR} = \frac{v_{tip}}{v_1} = \frac{2\pi \cdot n \cdot R}{v_1} \quad (2-7)$$

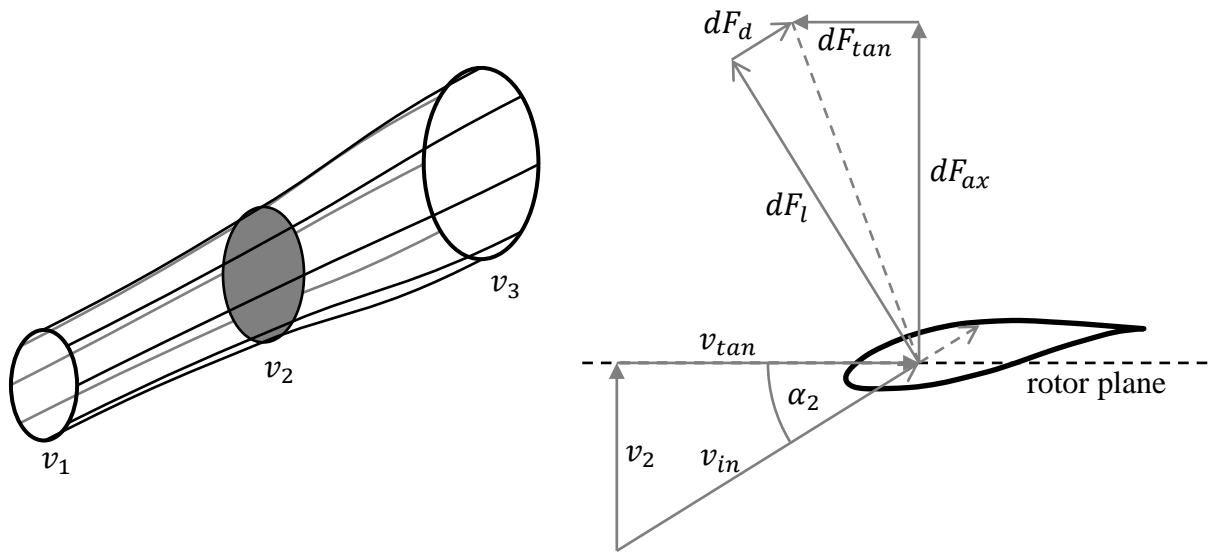


Fig. 2-4: Stream tube model of axial velocities ahead,  $v_1$ , in the rotor disc,  $v_2$ , and far behind,  $v_3$ , (left) and airfoil theory for lifting rotor blades (right)



Fig. 2-5: Examples for tidal current turbine devices – Voith HyTide<sup>®</sup> 110 (left), [84], OpenHydro (middle), [67], and BlueTEC (right), [17]

As sketched in Fig. 2-4, the local velocity  $v_2$  combines with the motion velocity  $v_{tan}$  to the inflow velocity  $v_{in}$ . This inflow results then in a drag force,  $dF_d$ , aligned to the inflow and a lift force,  $dF_l$ , perpendicular. Those can be split into an axial,  $dF_{ax}$ , and tangential,  $dF_{tan}$ , force component. The sum of all axial components is equivalent to the device thrust value

$F_{thrust} = \int dF_{ax} \cdot dr$  and the produced power is given by the tangential component,  $P = \int dF_{tan} \cdot 2\pi \cdot n \cdot r \cdot dr$ . The efficiency of the turbine depends on the losses due to drag, vortex shedding, blade tip vortices and many more.

### 2.2.2 Design Challenges

Besides the challenge of designing a low-cost high-efficiency turbine for extracting energy, the real world applications of wind and tidal current turbines yield many further engineering challenges. Many solutions for those can be drawn from the experiences made in wind energy technology. However, the tidal current energy faces several issues going beyond the scope of normal wind energy applications.

#### 2.2.2.1 Loads

While the density  $\rho$  of water is about 800 times higher than that of air, the typical rated current speed  $v_{rated}$  is about four times smaller for a tidal current turbine than for a wind turbine with the same rated power  $P_{rated}$ . With those scaling factors in mind, the required rotor diameter  $D$ , (2-8), assuming the same system efficiency and power coefficient  $c_p$ , is much smaller for a tidal current turbine than for a wind turbine of the same rated power; with the given values about 3.5 times smaller, (2-9).

$$D = \sqrt{\frac{8 \cdot P_{rated}}{\pi \cdot \rho \cdot v_{rated}^3 \cdot c_p}} \quad (2-8)$$

$$\frac{D_{tidal}}{D_{wind}} = \sqrt{\frac{\rho_{air}}{\rho_{water}} \cdot \left(\frac{v_{rated\ wind}}{v_{rated\ tidal}}\right)^3} \quad (2-9)$$

The same scaling method as for the rotor diameter can be applied to the rotor thrust  $F_{thrust}$ , (2-10), with the thrust coefficient  $c_{th}$ , showing that the tidal turbine has to withstand approximately four times higher thrust at rated operation, (2-11). This ratio of loads only depends on the ratio of current speed, as the high density-ratio and the smaller rotor diameter compensate each other. Subsequently, a tidal turbine requires a much sturdier nacelle and design than the comparative wind turbine.

$$F_{thrust} = \frac{\rho}{2} \cdot \pi \frac{D^2}{4} \cdot v^2 \cdot c_{th} \quad (2-10)$$

$$\frac{F_{thrust\ tidal}}{F_{thrust\ wind}} = \frac{v_{rated\ wind}}{v_{rated\ tidal}} \quad (2-11)$$

This scaling of loads is not straightforward. E.g., the out-of-plane bending loads  $M_{OoP}$  on the blades can be approximated to be proportional to  $F_{thrust} \cdot D$ . The increase in the thrust  $F_{thrust}$ , (2-11), is partially compensated by the reduced rotor diameter  $D$ , (2-9). Thus, the out-of-plane bending load  $M_{OoP}$ , (2-12), shows an increase of only 10%, based on the above given scaling ratios, despite the thrust force is increased by a factor of four.

$$\frac{M_{OoP\ tidal}}{M_{OoP\ wind}} = \sqrt{\frac{\rho_{air}}{\rho_{water}} \cdot \left(\frac{v_{rated\ wind}}{v_{rated\ tidal}}\right)^5} \quad (2-12)$$

A similar behavior occurs also for the rotational speed  $n$ , (2-13), showing an about 10% smaller rotational speed and thus 10% lower number of load cycles, assuming the same fluid dynamic design, properties and environmental conditions. However, due to other issues like cavitation, discussed below, the design of tidal turbines has typically a two times lower design tip speed ratio and thus a ca. two times lower number of load cycles.

$$\frac{n_{tidal}}{n_{wind}} = \sqrt{\frac{\rho_{water}}{\rho_{air}} \cdot \left(\frac{v_{rated\ tidal}}{v_{rated\ wind}}\right)^5} \quad (2-13)$$

Summarizing this comparison of loads between tidal and wind energy, it can be said that a tidal turbine is from an idealized point of view subject to higher design and extreme loads, but lower number of fatigue load cycles.

### 2.2.2.2 Environmental Conditions

The inflow conditions to tidal turbines consist of two major high frequency transients. On one hand, the turbulence caused by small-scale disturbances in the current and bathymetry, and on the other hand the waves. The turbulence is purely stochastic with a broadband spectrum. However, due to the inhomogeneity of the turbulent inflow, the rotating rotor blades are subject to additional changes in loads during the revolution with the rotational speed  $n$ . This effect is called rotational sampling and causes additional load variations, with dominant excitation frequencies on the multiples of the rotational frequency  $1\Omega$ . In case these frequencies match structural eigenfrequencies of the turbine, strong load responses can be expected.

The wave spectrum is in comparison much narrower and typically with a peak period of  $T_p = 8 \dots 12s$ . Due to the water surface motion, beneath the sea surface orbital velocities are induced within the penetration depth of the wave. Those orbital velocities are causing

additional fatigue loading, as they impact on the rotor similar to a time dependent current shear.

Beyond those external environmental impacts, the turbine is also triggering an additional local effect itself. If the velocity is locally accelerated, the static pressure can drop below the vapor pressure. Thus, the water forms steam bubbles, the cavitation, which collapse when reaching a region of higher static pressure. This process is known from shipbuilding and classical water turbines to be highly damaging for the structure. The maximum velocity of the rotor blades therefore needs to be limited.

### 2.2.2.3 Interference

Besides the technical environment, the tidal current turbine also has interferences with other technical and natural appearances in the ocean. E.g., for the interaction with ships the turbine needs to be either reliably visible from above the sea surface or submerged deeply to prevent collisions.



Fig. 2-6: Fish swarm approaching the nacelle of the Voith HyTide<sup>®</sup> 1000-13 tidal current turbine at EMEC during operation with  $n \approx 8.1rpm$  to feed from the marine growth, [84], Sept. 2014

Also, the impact on the local wildlife needs to be considered, e.g. noise could scare of animals leading to a change in their behavior. Furthermore, the issue of possible ‘fish strikes’, similar to the bird strike issue in wind energy, needs to be considered for the sake of both, the fish and possible damages to the turbine. The latter is even emphasized for human interaction, as

some people illegally dump garbage into the ocean leading to a load case which is sometimes called ‘refrigerator strike’ in discussions. However, those impacts and animal interferences are highly stochastic, and hard to predict and observe in their occurrence and possible result, Fig. 2-6.

An interference, which is more predictable, is a subtopic of site assessment. A too large number of tidal current turbines in a park installation could partially block a passage between islands deflecting the tidal currents from the park. Extensive research has been done on this topic within the field of site simulations, e.g. [71].

#### 2.2.2.4 Accessibility

The last big challenge mentioned here is the accessibility of the turbine. For both, installation and maintenance, the limits of operation for cranes and divers are given by the current velocity, wave and wind conditions, etc. Especially the current velocity is an issue here. As the site of installation generally has high current velocities, only a short period per day with current velocities below the critical value is available for maintenance activities. Therefore, access to the turbine is limited and even small malfunctions of the turbine can cause long down times. Thus, the design of the turbine needs to include a full maintenance strategy, which can be either a high reliability with minimum maintenance, or a strategy to access the system.

### 2.2.3 Turbine Concepts

Each concept on the market is taking a different approach to solve the design challenges. Even so, the turbine concepts can be grouped into three categories: Robustness, load reduction and unconventional concepts.

#### 2.2.3.1 Robustness Concepts

Turbine designs following the robustness concept aim for maximum reliability. This is achieved by simplifying the turbine system and neglecting any component, which might fail, or include redundant systems to avoid down times or further damages on a partial malfunction. Typically, this approach results in a high system weight, as high extreme and fatigue loads need to be survived.



### 2.2.3.2 Load Reduction Concepts

The load reduction concept is the typical approach in wind energy. By using active systems and controllers, extreme and fatigue loads are significantly reduced. Therefore, the system can be built with a lower system weight, however with higher risk of component failures and thus down times. This concept has therefore the potential to yield a better cost of energy, although with a higher risk.

### 2.2.3.3 Unconventional Concepts

The last group of concepts spans over the system designs, which leave the classical design of turbines, e.g. oscillating wing or kite concepts, to avoid one or more of the above mentioned design challenges. However, those approaches often have drawbacks on other aspects of the design challenges as e.g. higher loads, increased system complexity or pulsating power output.

### 2.2.3.4 Technological Share of the Market

Determining the share of the market of the three concepts is difficult. Especially between the robustness and load reduction concept many hybrid designs exist, which have, e.g., a yaw, but no pitch actuator. Therefore, it is more straightforward to show the share of the market by the rotor type, Fig. 2-7.

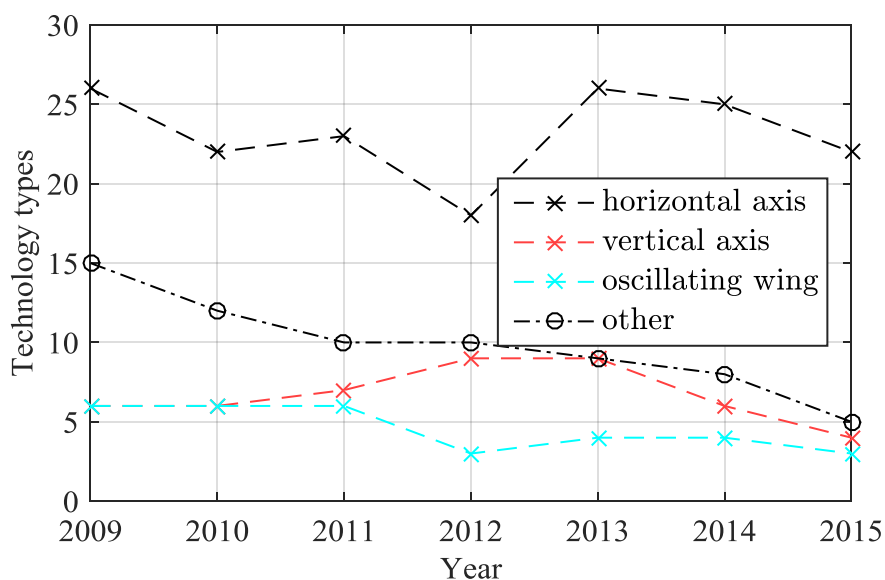


Fig. 2-7: Number of tidal current turbine technologies for different types of turbines, reproduced from [49]

The market data shows, that the technology of tidal current turbines consolidates and converges towards horizontal axis turbines, but it is still too premature to make a definitive judgement and further experience and research on tidal current turbines is required.

#### 2.2.4 Investigated Turbine System Voith HyTide<sup>®</sup>

The Voith HyTide<sup>®</sup> tidal current turbine, Fig. 2-8, [84], is a typical representative of the robustness concept. During the design of the system, the focus was on the reliability. Therefore, any active component not essential for operation was removed leading to a system with a low number of moving parts. The conceptual solutions for the key subsystems resulting from this process are shown in Table 2-1.

The turbine investigated in the present research is the HyTide<sup>®</sup>1000-13 version. This is the first full scale version of the turbine concept with a rated power output of  $P_{rated} = 1000kW$  and a rotor diameter of  $D = 13m$ . This device was installed at the European Marine Energy Center (EMEC), [28], in 2013. The geometric and design specifications are detailed in Table 2-2 and in the simulation setup, Section 4.1.

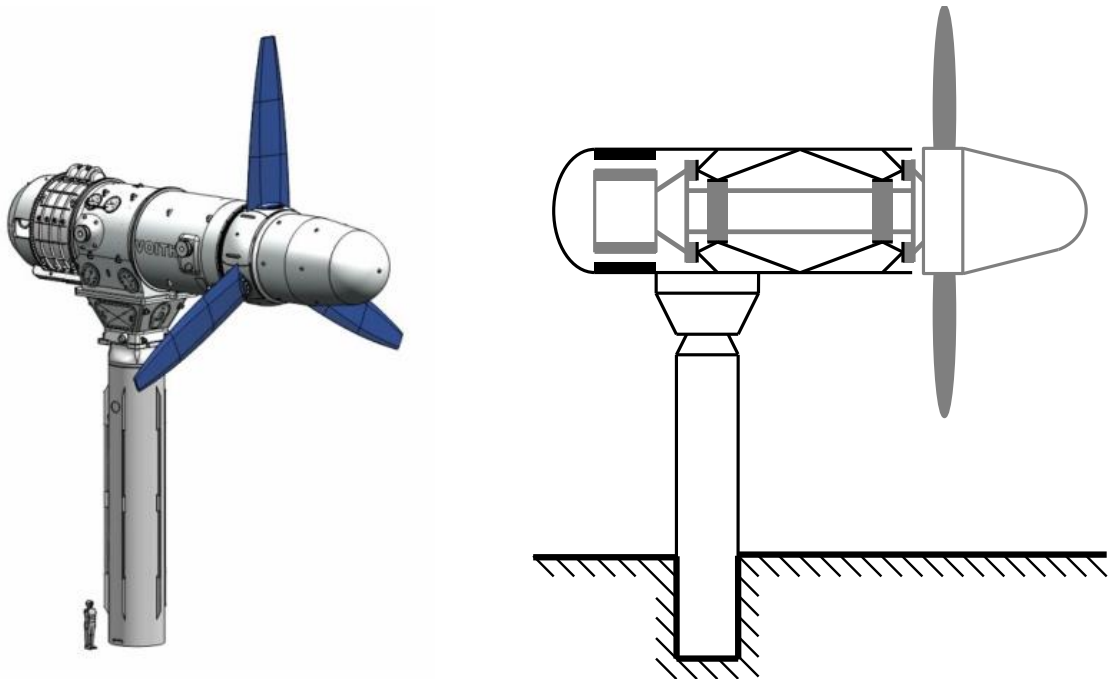


Fig. 2-8: CAD image of Voith HyTide<sup>®</sup> 1MW tidal current (left, [84]) and conceptual sketch of turbine (right)

Table 2-1: Summary of Voith HyTide<sup>®</sup> tidal current turbine concept

Rotor blades	Fixed pitch, bi-directional design, double symmetric hydrofoils
Load limitation	Variable speed, overspeed controller
Drivetrain	Direct-drive, without gearbox
Bearings	Axial and radial fluid dynamic bearings, seawater lubricated
Nacelle	Load carrying shell, flooded, without dynamic sealing
Current alignment	Fixed yaw, upstream and tower wake operation
Foundation	Monopile structure, drilled into seabed
Generator	Permanent magnet synchronous generator (PMSG), flooded
Grid connection	Land based AC-DC-AC converter
Installation and maintenance	Crane installation, plug connection of tower and nacelle

Table 2-2: Voith HyTide<sup>®</sup> 1000-13 turbine data

Rated power	$P_{rated} = 1MW$	Rotor diameter	$D = 13m$
Hub height	$h_{hub} = 15m$	Nacelle diameter	$D_{nacelle} = 3.8m$
Nacelle length	$l_{nacelle} = 17.8m$	Rotor tower distance	$l_{rotor-tower} = 6.63m$
Blade root chord length	$l_{blade\ root} = 1.95m$	Blade tip chord length	$l_{blade\ tip} = 0.98m$
Tower diameter	$D_{tower} = 2m$	Cut-out speed	$v_{cut-out} = 4m/s$
Nacelle mass	$m_{nacelle} \approx 195t$	Total system mass	$m_{total} \approx 280t$



---

### 3. SIMULATION METHODOLOGY

Within this chapter, the simulation methods for analyzing fluid-structure-interaction (FSI) will be introduced. First, the requirements to simulations of the hydroelastic effects on tidal current turbines as well as the state-of-the-art of simulation methods are discussed, including the applied CFD and multibody methods. This is followed by a detailed description and specification of the here developed fluid-multibody-interaction methodology. The chapter concludes with the validation procedure and the approval of the toolchain for the present application.

#### 3.1. State-of-the-Art Hydroelastic Simulation Methods

A simulation method for hydroelastic effects must fulfill two main requirements: The method needs to simulate all relevant effects accurately with the required level of detail and reliability, and the method should be limited to a reasonable usage of computational resources. These requirements are connected to each other, as more details in the model usually mean more computational resources are required. It is therefore necessary to find an optimal setup, which is accurate and detailed enough for the questions to be addressed, but still manageable with the available computing power. Furthermore, the available level of detail in the input data can be a limitation for the setup of the model.

In the following subsections, a summary of the current state-of-the-art methods, their application and limitations is presented. This discussion is split into the topics of fluid, structural and multi-physic simulation.

##### 3.1.1 Fluid Simulation Methods

For the simulation of fluid loads either general-purpose methods as the computational fluid dynamics (CFD) or dedicated semi-empirical models can be used. The latter approach splits the problem by the hydrodynamic effects and simulates each of them independently with, e.g., the blade element momentum theory (BEMT) for the rotor hydrodynamics and the Morison-equation for the added mass. Compared to the general-purpose methods this approach is fast and numerically efficient, but it leads to a reduced level of detail in the results, as interactions of hydrodynamic effects are not taken into account.

### 3.1.1.1 Blade Element Momentum Theory (BEMT)

The BEMT is a method adopted from wind energy, [34], and is nowadays for both, tidal and wind turbines, the most common method for simulation of the rotor's aero- and hydro-dynamics respectively, [11]. The reason for this is its high computational efficiency, making it feasible for large amounts of stochastic load simulations, while giving relatively accurate results for most standard operational cases. This method is therefore used mainly for design iterations and basic load evaluations, e.g. [14], [35] and [60]. However, the method is limited by the physical assumptions on the derivation of the fundamental equations.

The theory of the BEMT is a generalized form of the momentum-actuator disc approach used by Betz and discussed in Section 2.2.1. While Betz simplified the actuator disc to a device of unspecified type applying a force to the fluid, the BEMT defines this device to be a rotating horizontal axis rotor with lifting airfoils and  $n_{Blades}$  blades, cf. Fig. 2-4, rotating with the rotational speed  $\Omega$ . For each annulus of the rotor with radius  $r$  the equilibrium of the momentum forces and blade loads is solved in axial and tangential direction, (3-1), (3-2), [22]. This results in the axial and tangential induction factors  $a_{ax}$  and  $a_{tan}$ , (3-3). The blade forces are calculated with the local lift  $c_l$  and drag coefficient  $c_d$ , depending on the inflow velocity  $v_{in}$ , the chord length  $t_{chord}$  and angle of attack  $\alpha_{AoA}$ , which is defined to be the difference of the inflow angle  $\alpha_2$  and the twist angle  $\alpha_{twist}$ .

$$a_{ax} = \frac{8\pi r \cdot v_1^2 \cdot (1 - a_{ax})}{n_{Blade} \cdot t_{chord} \cdot v_{in}^2 \cdot [c_l \cdot \cos(\alpha_2) + c_d \cdot \sin(\alpha_2)]} \quad (3-1)$$

$$a'_{tan} = \frac{8\pi r \cdot (v_1 \cdot (1 - a_{ax}))^2}{n_{Blade} \cdot t_{chord} \cdot v_{in}^2 \cdot [c_l \cdot \sin(\alpha_2) - c_d \cdot \cos(\alpha_2)]} \quad (3-2)$$

$$a_{ax} = \frac{v_3 - v_1}{2 \cdot v_1} \quad a_{tan} = \frac{v_{tan}}{2 \cdot \Omega \cdot r} \quad (3-3)$$

The flow in the annuli is assumed to be stationary with a homogenous undisturbed inflow velocity  $v_1$ , without radial velocity components and independent from neighboring radii. Subsequently, the method is not able to take transient and yawed inflow, turbulent wake states, blade tip vortices, 3d-stall, rotor-foundation-interaction, etc. into account, [11]. For each of those issues empirical correction models have been developed. Still, these empirical modifications rely on accurate parameter calibration, which changes with every new rotor design. This method is therefore only applicable to calculate the rotor in simple cases with reference data available for calibration, but not to investigate detailed rotor flow phenomena.

## 3.1.1.2 Morison Equation

Besides the rotor hydrodynamics, the added mass is the second most important hydrodynamic source of loads on a tidal turbine. To simulate this effect, the Morison equation, (3-4), [56], shown here in its 1-dimensional form, is adapted to the tidal energy technology from offshore engineering. It describes the load on a structure of volume  $V$  with the velocity  $v$  in a homogeneously accelerated fluid with velocity  $u$  and density  $\rho$ , based on the added mass coefficient  $c_a$  and the drag coefficient  $c_d$ .

$$F = \underbrace{\rho V \dot{u}}_{\text{Froude-Krylov force}} + \underbrace{\rho c_a V (\dot{u} - \dot{v})}_{\text{hydrodynamic mass force}} + \underbrace{\frac{\rho}{2} c_d A (u - v) |u - v|}_{\text{drag force}} \quad (3-4)$$

The method is usually used to simulate the added mass effect and wave loads on offshore structures. It is one of the most common methods to calculate hydrodynamic loads on moving objects in homogenous flow conditions. The tidal energy is only a small subset in the range of usual applications, which cover offshore wind energy, [41], ship design, [61], wave energy, [88], among many others. However, the aforementioned assumption of a homogeneously accelerated fluid is the main limitation of the method. Due to this assumption, the method is not applicable in case of, e.g., structures with large geometrical dimensions compared to the wave length or size of disturbance. In addition, the interaction of bodies is not taken into account, but they are simulated separately.

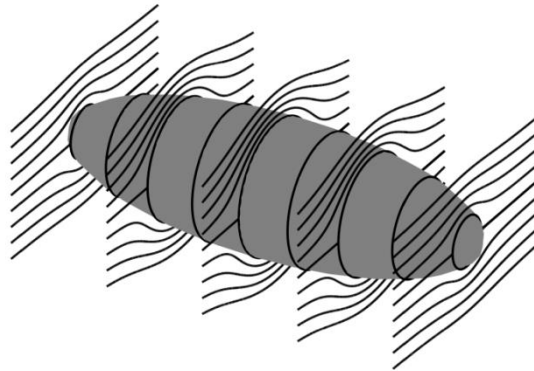


Fig. 3-1: Slender body theory applied to an ellipsoid perpendicular to main axis

The values of  $c_a$  and  $c_d$  are shape dependent and often empirically obtained. For most simple geometries the values are tabulated, [16]. For complex geometries the boundary element method (BEM), [6], or the slender body theory, Fig. 3-1. [61], are applied. The BEM can be used to calculate the 6x6 added mass tensor and the response amplitude operators (RAO) of

almost any geometry by discretizing its surface and applying the potential flow theory. However, the BEM is limited to rigid objects, [24].

On the other hand, the slender body theory (SLB) assumes the geometry consists of isolated slices aligned perpendicularly to the motion. The SLB is therefore able to simulate the added mass on flexible objects, however neglects similar to the BEMT the 3-dimensionality of the geometry.

### 3.1.1.3 Computational Fluid Dynamics (CFD)

The computational fluid dynamics (CFD) is a general-purpose solution strategy for the Navier-Stokes equations, describing the conservation of mass, momentum and energy in a flow field. Most commonly, CFD relies on the finite volume method (FVM). This approach discretizes the fluid volume with a grid and solves the continuity equations by evaluating the mass, momentum and energy fluxes  $f_{\vec{n}}$  between neighboring elements. The quality of this grid, defined by resolution, distribution and shape of the elements, is essential for accurate results and requires an appropriate setup. This will be discussed in Section 4.1.1.1.

Within the Navier-Stokes equations, almost any disturbance in the fluid field is described. However, computing all of those fully resolved with the direct numerical simulation (DNS) approach, Fig. 3-2, would require an extremely fine grid and time step resolution, and consequently it would require computational resources not appropriate for technical applications. Therefore, the velocities are split into a time averaged value  $\bar{u}_i$  and a disturbance  $u'_i$  with  $u_i = \bar{u}_i + u'_i$ . Based on this distinction the momentum equilibrium equations within the Navier-Stokes equations are transformed into the Reynolds-averaged-Navier-Stokes equations (RANS) with the Reynolds stress  $\overline{\rho u'_i u'_j}$ . With the approximation of  $\bar{u}_i$  changing slowly over time compared to the time resolution, the transient solution can be obtained with the unsteady-RANS equations (URANS), (3-5), shown here in the incompressible form with the fluid density  $\rho$  and viscosity  $\mu$ .

Further intermediate levels of idealization for the CFD methods such as large eddy simulation (LES) or detached eddy simulation (DES) are not described here and can be consulted in the relevant literature.

To solve the Reynolds stress the most common approach in RANS and URANS is the eddy viscosity  $\mu_t$  proposed by Boussinesq, (3-6), [18]. The calculation of the eddy viscosity and the turbulence kinetic energy  $k_t$  is under ongoing research and based on empirical turbulence



models, e.g. the Shear-Stress-Transport (SST) model, [52], or the Scale Adaptive Simulation (SAS), [53].

$$\nabla \cdot \bar{u} = 0$$

$$\rho \left[ \underbrace{\frac{\partial \bar{u}_i}{\partial t}}_{\text{Variation}} + \underbrace{\bar{u}_j \frac{\partial \bar{u}_i}{\partial x_j}}_{\text{Convection}} \right] = - \underbrace{\frac{\partial \bar{p}}{\partial x_j}}_{\text{Source}} + \frac{\partial}{\partial x_j} \left( \underbrace{\mu \frac{\partial \bar{u}_i}{\partial x_j}}_{\text{Diffusion}} - \underbrace{\overline{\rho u'_i u'_j}}_{\text{Reynolds stress}} \right) \quad (3-5)$$

$$\overline{\rho u'_i u'_j} = -\mu_t \cdot \left( \frac{\partial \bar{u}_i}{\partial x_j} + \frac{\partial \bar{u}_j}{\partial x_i} - \frac{2}{3} \frac{\partial \bar{u}_k}{\partial x_k} \delta_{ij} \right) + \frac{2}{3} \rho k_t \delta_{ij} \text{ with } i, j, k \in [x, y, z] \quad (3-6)$$

Being a general-purpose method, the CFD considers the various fluid effects on a tidal turbine inherently. Therefore, no extension with further models is required to take added-mass, rotor-foundation-interaction, rotor hydrodynamics, etc. into account. This makes the CFD the most used fluid-dynamic method in the full spectrum of technical applications. However, due to the level of detail of the URANS solution, the required computational resources are several orders of magnitude larger than for the previously presented semi-empirical methods.

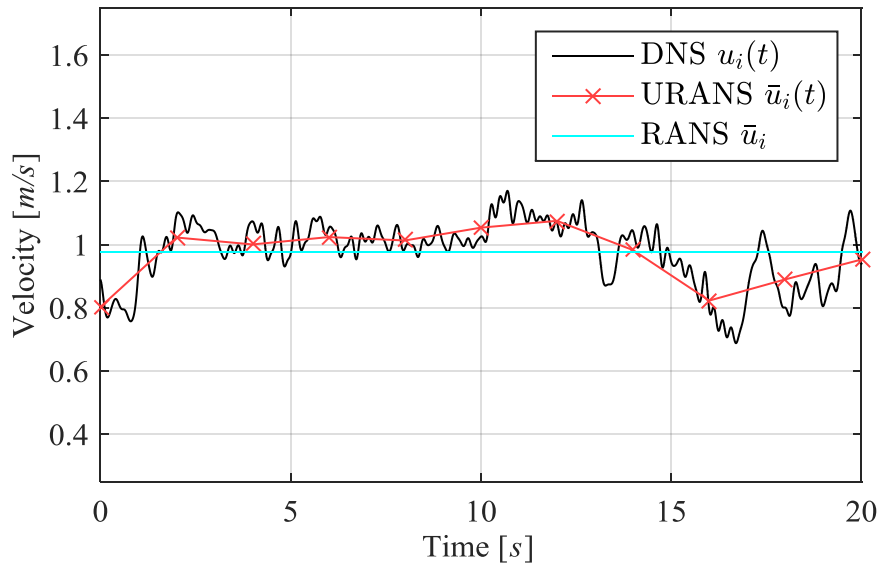


Fig. 3-2: Comparison of DNS, RANS and URANS on an artificial velocity time series

### 3.1.2 Structural Simulation Methods

For modelling the structural response of a tidal turbine, the properties of the turbine need to be described with equations of motion. The complexity of these equations depends on the available information, as well as on the desired level of detail in the simulation results. While the finite element method (FEM) requires the full structural and geometric details and

calculates the local stress distribution, the multibody method requires only the mass and stiffness distribution and results in the macroscopic deformation and loads.

### 3.1.2.1 Multibody Method

The multibody method reduces the structural behavior of a system to a mostly small number of degrees of freedom (DoF) each correlated to an equation of motion. Combined, the equations form a system of partial differential equations with the state vector  $\vec{x}$  containing the position of each DoF. In the linearized form, the system properties are described by the mass matrix  $\mathbf{M}$ , damping matrix  $\mathbf{D}$  and stiffness matrix  $\mathbf{C}$ , (3-7).

$$\mathbf{M} \cdot \ddot{\vec{x}} + \mathbf{D} \cdot \dot{\vec{x}} + \mathbf{C} \cdot \vec{x} = \vec{F}(t, \vec{x}, \dot{\vec{x}}) \quad (3-7)$$

In case of a non-linear system, the mass, damping and stiffness matrix can be time and position dependent with e.g.  $\mathbf{M} = \mathbf{M}(t, \vec{x}, \dot{\vec{x}})$ .

On the right hand side of the equation is the load vector  $\vec{F}$ , containing in the case of a tidal turbine the hydrodynamic loads, the added mass, etc. as a function of time  $t$ , the state vector  $\vec{x}$  and its derivatives. By transforming the system to a diagonal mass matrix, [33], the state accelerations  $\ddot{\vec{x}}$  can be solved with a time integration algorithm, [59].

Due to the reduced number of DoF, the multibody simulation methods offer a speed advantage compared to other methods, and the suitability for linearization of the system equations makes it a common tool for controller design. However, as the structural properties are simplified to the values of mass and stiffness, the multibody method can not be used to analyze the detailed stresses and fatigue of components.

### 3.1.2.2 General Multibody Systems (MBS)

The general multibody system (MBS) extends the equations of motion from the multibody method by taking not only the mass and stiffness of a component into account, but also its dynamic properties. These properties are typically described by an eigenvalue analysis and subsequent modal reduction of the component, [9]. This process can be based either on a beam theory description, [25], or on a FEM model, [26], resulting in additional partial differential equations with the modal DoF  $\vec{x}_m$  coupled to the state vector  $\vec{x}$ . By transforming the state vector  $\vec{x}_m$ , the mass matrix  $\mathbf{M}_m$  can be setup as diagonal matrix and added to the overall structural system. As the modal reduction linearizes the deflection, this method is limited to the assumption of small deflections. However, this issue can be overcome, if

required, by splitting the component into multiple adjacent components, each subject to small local deflections, [29].

Based on the methodology of introducing the modal DoF into the set of equations the number of eigenmodes taken into account can be easily changed within the model making it suitable for sensitivity analyses. Also, the actual geometry of the component is not required, especially in case of the beam theory, but only the structural properties of mass and stiffness distribution, which can be translated into the dynamic properties with, e.g., the beam theory. The general multibody method therefore provides a low level of detail with respect to local stresses, but is well suited for system engineering applications. It is subsequently used in many system analysis and optimization processes, e.g. in wind energy research.

### 3.1.2.3 Finite Element Methods (FEM)

In contrary to the MBS, which analyzes a system top-down based on its integral properties, the finite element method (FEM) subdivides each component into a typically large number of elementary objects, the finite elements, with a simpler, 'known' solution. The FEM is therefore a bottom-up approach. Each elementary object is described by the elasticity and a basis function. With the continuity condition, the basis functions combine to a system of equations, which is then solved with respect to the boundary conditions.

The large number of elements and thus DoF within the FEM model increase the required computational resources. However, as it produces detailed results regarding local stress and deformations, it is the standard method for mechanical simulations and a large number of tools are available.

Depending on the level of detail of results, the required level of detail for the model input can be very high. Therefore, the full geometric and material data of a component or system is required in order to carry out an FEM analysis. However, these information may not be available during the conceptual design phase of a project, making the application of the FEM difficult at early design stages or in system analysis and more suitable for the final analysis of a design, where highly detailed results are required.

### 3.1.3 Multi-Physic Simulation Methods

Multi-physic methods combine two or more simulation tools to find a solution for the interaction of effects. E.g., a flexible structure of a rotor blade will result in different

hydrodynamic loads than a rigid rotor. Therefore, it is required to combine fluid and structural simulation solvers.

The available multi-physic simulation methods, relevant for the present type of application, can be split into two groups: The engineering tools, and the fluid-structure-interaction (FSI) methods. Further hybrid methods between these two exist, but are most often used within the same type of application.

#### 3.1.3.1 Engineering Tools

The category of engineering tools is characterized by a combination of semi-empirical methods with a focus on the efficient simulation of stochastic loads. In wind and tidal energy they are often implemented as a combination of BEMT and the Morison equation for the fluid and the MBS for the structural representation, e.g. GH-Bladed, [33], and NREL-FAST, [40]. Despite of the limitations, the approach provides reasonable results for most applications and points of operation. Therefore, the engineering tools can be used for design load calculations, but are not feasible for applications requiring high level of detail, or transient calculations.

#### 3.1.3.2 Fluid-Structure-Interaction (FSI)

FSI-tools focus on a high level of detail for the solution of multi-physic problems. Typically, they are based on combined CFD and FEM methods in an either coupled solver approach, e.g. Ansys, [5], or monolithic solver, e.g. AcuSolve, [2]. The FSI methodology is only feasible for deterministic load cases due to their high demands on computational resources. Also, the FSI require full details on the geometric and structural properties. Therefore, the results of these models can be expected to represent the physics in greater detail, but their application is limited to well-defined and often small set of load cases. In tidal energy, the FSI is therefore limited to the simulation of, e.g., a single rotor blade as shown by [42], [57], [62] and [79] with a strong (bi-directional) coupling, or the tower with a weak (uni-directional) coupling, [38].

#### 3.1.4 Discussion of the Available Hydroelastic-Tools

For the present application of evaluating the impact of flexible structural components on the hydrodynamic and operational loads on a tidal turbine, neither the engineering tools, nor the FSI-tools are suitable. On the hydrodynamic representation, a detailed solution is required in order to simulate the transient rotor hydrodynamics, the added mass and damping of the

moving surfaces, as well as the interaction between neighboring components. This is fulfilled only by the CFD methodology.

On the other hand, the structural representation is limited by the available computational resources and data of the turbine structure. For many components, only the macroscopic properties are available within this research project, and subsequently the setup of a full FEM model is not possible. The structural representation therefore needs to be idealized and the MBS was found to be the most suitable approach here. This method has also the advantage of being easily adaptable regarding the combination of flexible and rigid objects.

Hence, the optimal tool for the present application is therefore a hybrid of an engineering tool on the structural side and a high fidelity method on the fluid side.

### **3.2. Fluid-Multibody-Interaction-Method (FMBI)**

Based on the above given discussion of the requirements to the hydroelastic-tool and the lack of a suitable method, a new method consisting of CFD and MBS is developed and implemented. This combination of tools is referred to as the fluid-multibody-interaction (FMBI).

#### **3.2.1 Overview**

For the FMBI-Method, two industry-standard software packages are coupled here via a method developed in this research and presented in the following section. The structural representation is modeled by using the MBS-solver Simpack, [77]. It relies on a greatly reduced number of degrees of freedom compared to FEM, but calculates results only at a discrete number of locations. The fluid is simulated with the CFD code Ansys CFX, [6]. It solves the URANS equations on structured or unstructured grids, using the finite volume method (FVM).

##### **3.2.1.1 Previous Approaches to the FMBI-Method**

A similar methodology was also developed by [7] for aircraft wings, and by [54] and [80] for the simulation of helicopter and wind turbine rotor blades. Both of these previous approaches to the FMBI used the MBS-solver Simpack and research codes for the CFD. However, while on the development of [7] not much information is available, the implementation of [54] and [80] was used by, e.g., [37]. This approach utilizes the compressible CFD code Flower, [27]. However, this implementation of the FMBI is limited by its coding to the coupling of rotor

blades and it is bound to an outdated version of Flower. In addition, the communication is based on a known radial grid distribution in CFD, which requires the CFD grid to be matched with the communication markers in Simpack, making it difficult to match the CFD and MBS model during the setup. Subsequently, it is not feasible for the present application of simulating the rotor, nacelle and tower of the tidal current turbine. Therefore, only the basic idea of those previously implemented couplings can be used for the present development.

### 3.2.1.2 Scope of Development

For the coupling, seven additional functionalities in the CFD and MBS codes are required. These are, as shown in Fig. 3-3, a receiver and a sender unit for each code, which are responsible for transferring the coupling data from one memory space to the other, and the translators, responsible for the transformations between the different definitions of loads, motion and coordinate systems. The simulation is controlled by the seventh functionality, which is implemented in the moderator block. This block controls the iteration process and instructs CFX and Simpack, whether to wait for the other code, continue with the current time-step iteration, or advance in time.

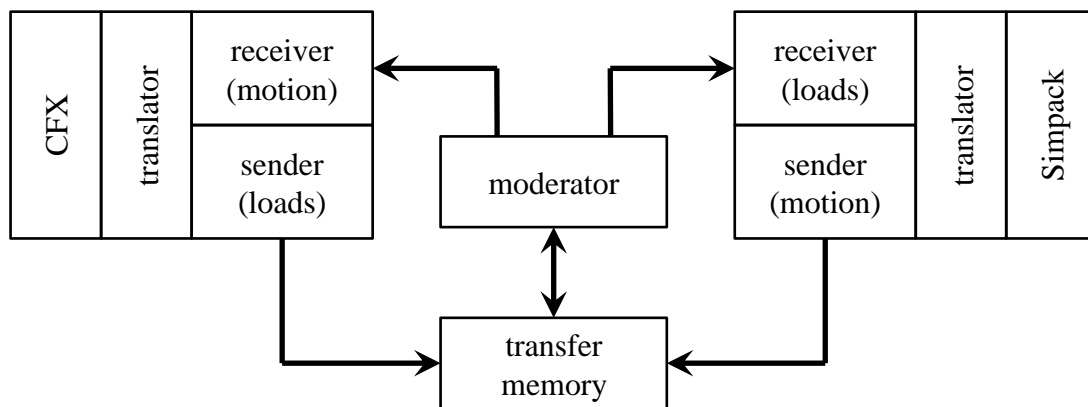


Fig. 3-3: Basic structure of the FMBI coupling code

### 3.2.1.3 Iteration Process

The iteration process performed within each time step is sketched in Fig. 3-4. As can be seen, a fully implicit, strong coupling method is applied; i.e. the toolchain transfers the loads and deformations bi-directionally and repeats every time step until convergence for that time step is reached.

Each time step iteration starts with a structural time integration, assuming the loads calculated in the previous time step to be constant in the current time step. The resulting deformations

are transferred to the fluid solver, which calculates the new loads for the current time step. With these updated loads, the structural time integration is repeated to calculate updated deformations. The updated deformations are then again fed into the fluid solver to further increase the precision of the loads. This iteration process of updating the structural deformations and fluid loads alternately is repeated until two subsequent communication iterations give same results within the desired tolerance level.

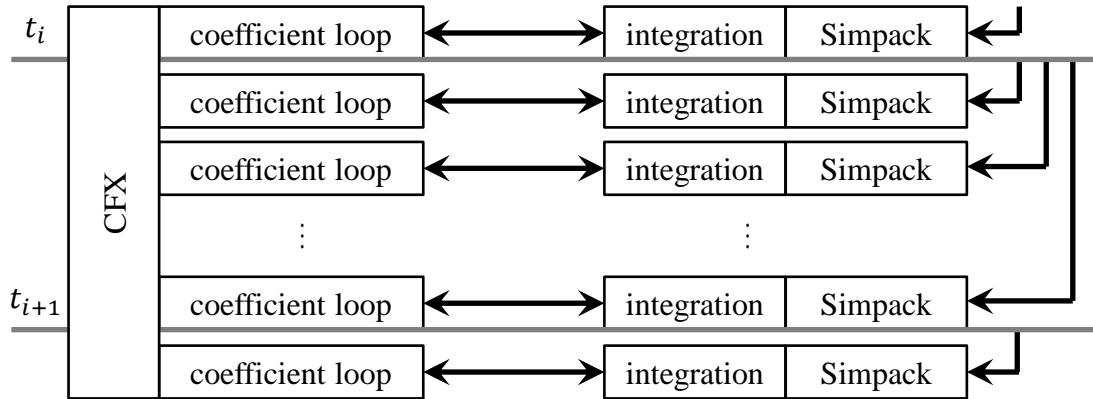


Fig. 3-4: Data flow structure of time step iterations

The iteration process requires the codes to return to the initial state of a time step upon request during a solver run. However, the closed codes for the fluid and structural solver do not offer this possibility, and thus special attention was required for the timing of the simulation. Therefore, CFX is interrupted within its built-in implicit iteration for the fluid solution and Simpack is restarted from the result of the last converged time step in each coupling iteration. Then Simpack integrates only a single coupling time step, which needs to be equal to the fluid time step, and stops. CFX continues with its next inner implicit iteration (coefficient loop) afterwards. Therefore, the coupled FMBI run consists of one CFX-Solver run and  $n_{timestep} \cdot n_{coeff.loops}$  Simpack runs. This repeated start-stop of Simpack produces some overhead, but is still the most efficient solution if a change in neither the CFX, nor the Simpack code structure is possible.

[7], [54] and [80] prevented this issue in their development by limiting the coupling to an explicit or predictor-corrector operation. The same development steps have been done in the preliminary stage of the present development. However, the explicit coupling requires the fluid density to be low compared to the structural density  $\rho_{fluid} \ll \rho_{structure}$  for stability. This condition is not fulfilled for a tidal current turbine and thus to achieve the stability of the fluid-structure-interaction simulation for a tidal current turbine, either the proposed implicit

scheme or very small time steps on an explicit scheme are required. This would increase the computational resources significantly. Therefore, the fully implicit method will be used in this research and is presented here. The issue of stability will be further discussed in Section 4.1.1.5.

### 3.2.2 Basis for Communication Interface

As stated above the MBS calculates the results only on a discrete number of locations, named markers. This impacts also on the communication within the FMBI compared to the FSI. In a classic FSI the surface deformation is calculated on the FEM grid as local deformation  $\Delta\vec{x}_{FEM}$  in each node, communicated and interpolated to the CFD grid. This local deformation contains inherently the combination of translation and rotation. In case of the FMBI the local deformations are unknown, but the translation vector  $\Delta\vec{x}_0$  and rotation vector  $\vec{\alpha}_0$  are calculated at the marker locations. Therefore, only those six values per location, three translations and three rotations, are transferred from the MBS to the CFD and the fluid translator needs to interpolate, respectively extrapolate the local deformations.

The same issue occurs for the hydrodynamic loads. The solution of the CFD inherently contains the surface pressure and wall shear distribution, which can be directly interpolated to the FEM surface in a classic FSI. In contrast, the MBS requires the macroscopic force and moment loads to be applied to the markers. These have to be integrated by the CFD translator, as the MBS has no information on the surface geometry. The communication from CFD to MBS therefore reduces to six values per marker, three forces and three moments.

For integrating the loads, the surface of the simulated object has to be split into regions within the CFD. Each of these regions is then associated with one of the communication markers within the MBS. The location of the markers relative to their respective region is discussed in Section 3.2.4.4.

For the communication itself, several options exist, which are grouped here by their persistency. Volatile memories like communicating on a shared RAM memory, via TCP/IP interfaces, etc. offer the advantage of being fast and applicable for, e.g., transferring arrays. However, this advantage comes with the cost of increased difficulties in debugging and monitoring the communication, as it is reset at each communication. Furthermore, the TCP/IP interface can result in system dependencies, as the libraries for TCP/IP usage in Fortran, cf. Section 3.2.5.2, differ between Linux and Windows. On the other hand, the option of



implementing the communication with ASCII-files on the hard drive, a non-volatile memory, is slower on access than a volatile memory and requires additional resources for the translation between binary and ASCII-format. However, accepting this drawback comes with the advantage of platform independency, simple codes based on well-known file access methods, and a human read- and modifiable communication. The latter is especially useful during the development process to identify bugs and to recover the simulation in case of a crash. Therefore, this option of file-based communication is chosen for the FMBI interface. By locating the communication files in an out-of-the-box RAM-disk or network storage drive, it can be further extended to increase speed or to enable distributed parallel computing, without any changes to the code.

### 3.2.3 Structural Translator

The structural translator is the interface between the communication of the coupling and the structural solver. It is therefore responsible for collecting the deformations in the communication reference system and preparing it for the sender unit. On the incoming data, its task is to match and transform the loads from the CFD output to its corresponding markers in the Simpack model. The transformation of the force  $\vec{F}$  and moment  $\vec{Q}$  vector from the communication reference frame (*REF*) to the body reference frame (*BRF*), required for the load application in Simpack, can be summarized as (3-8).

$$\begin{aligned}\overrightarrow{F}_{BRF} &= \mathbf{A}_{TR:REF \rightarrow BRF} \cdot \overrightarrow{F}_{REF} \\ \overrightarrow{Q}_{BRF} &= \mathbf{A}_{TR:REF \rightarrow BRF} \cdot (\Delta \vec{r}_{REF \rightarrow BRF} \times \overrightarrow{F}_{REF} - \overrightarrow{Q}_{REF})\end{aligned}\tag{3-8}$$

### 3.2.4 Fluid Translator

As described in the section of the structural translator, also the fluid translator has the same two tasks of organizing and interpreting the incoming and outgoing data. For the outgoing data, the required force and moment values are calculated here based on the build-in functions of CFX. These functions integrate the pressure and wall shear on the object's surfaces in the communication reference frame. Therefore, no further transformation is required and this task of the translator simplifies to a pass-through.

The second task of translating the incoming data of discrete deformations and rotations is far more complex. The process is divided here into the coordinate transformations and the surface mapping.

### 3.2.4.1 Coordinate Transformations

The coordinate transformation calculates the translational motion  $\Delta\vec{x}_{loc}$  of an arbitrary point in space  $\vec{p}_{loc}$  based on the translation  $\Delta\vec{x}_0$  and rotation in Cardan angles  $\vec{\alpha}_0 = [\alpha, \beta, \gamma]$  at the reference location  $\vec{p}_0$  received from the structural solution, (3-9), with the abbreviation  $s_\alpha, s_\beta, s_\gamma$  and  $c_\alpha, c_\beta, c_\gamma$  for the *sin* and *cos*, respectively.

$$\Delta\vec{x}_{loc} = \mathbf{A}_{TR} \cdot (\vec{p}_{loc} - \vec{p}_0) + \Delta\vec{x}_0$$

$$\mathbf{A}_{TR} = \begin{bmatrix} c_\beta c_\gamma & -c_\beta s_\gamma & s_\beta \\ s_\alpha s_\beta c_\gamma + c_\alpha s_\gamma & -s_\alpha s_\beta s_\gamma + c_\alpha c_\gamma & -s_\alpha c_\beta \\ -c_\alpha s_\beta c_\gamma + s_\alpha s_\gamma & c_\alpha s_\beta s_\gamma + s_\alpha c_\gamma & c_\alpha c_\beta \end{bmatrix} \quad (3-9)$$

### 3.2.4.2 Surface Mapping Strategies

For rigid objects the coordinate transformation can be applied to all surface points with the same set of  $\Delta\vec{x}_0, \vec{\alpha}_0, \vec{p}_0$ , and the reference location at the sole marker location  $\vec{p}_0 = \vec{p}_{marker}$ . However, for flexible objects, this is not the case and for any point on the object's surface, the local deformation is required. In classical FSI simulations, this is achieved by mapping the FEM grid onto the CFD grid as sketched in Fig. 3-5 (left).

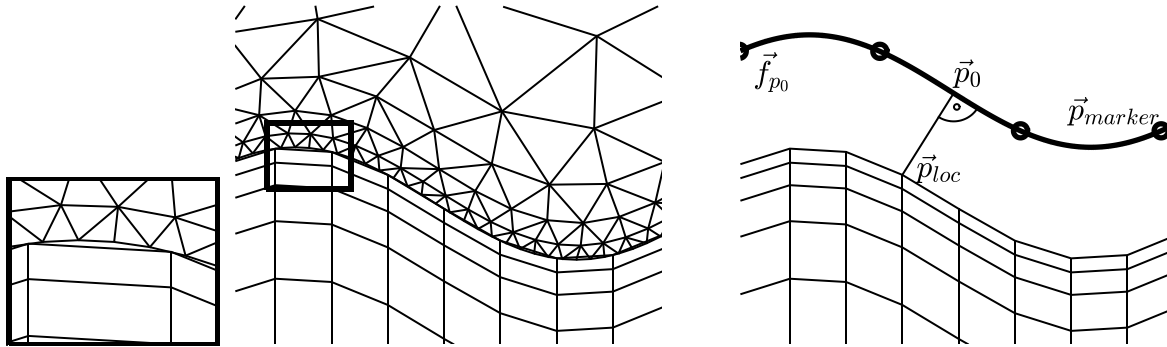


Fig. 3-5: Surface mapping strategy from FEM (tetra) to CFD (quad) grid (left) and spline interpolation method (right)

This approach is able to transfer the detailed surface deformations to the CFD grid, but relies on high-resolution structural deformations. In case of a MBS-CFD-coupling, this high resolution of structural deformations is not available and subsequently a workaround had to be found. Possible solutions are either to interpolate within the structural model and subsequently increase the number of locations for communication, or to interpolate the required data on the CFD side. Increasing the number of locations also increases the effort for setting up the simulations, as the locations in the structural and the fluid model must match. This is not automatically the case and needs to be done manually during the setup.

Furthermore, the required computational effort for the coupling increases as the amount of transferred data rises by typically four orders of magnitude with interpolation on the structural side instead of the CFD side.

Therefore, the latter approach of interpolating the required data within the fluid translator is chosen here. The fluid translator also performs the required coordinate transformations. These operations are merged together. Based on the coordinate transformation (3-9), a set of 9 values, contained in  $\Delta\vec{x}_0$ ,  $\vec{\alpha}_0$  and  $\vec{p}_0$ , is required for each point on the surface, which is interpolated here based on splines.

### 3.2.4.3 Spline-based Interpolation

The spline-based interpolation relies on the assumption that the deformation of the object under investigation can be approximated by slices with constant deformation parameters,  $\Delta\vec{x}_0$ ,  $\vec{\alpha}_0$  and  $\vec{p}_0$ . Each slice is defined to be normal to the central curve  $\vec{f}_{p_0}$ , which is calculated as a spline through the reference locations  $\vec{p}_{marker}$ , used for communication along the flexible object, Fig. 3-5 (right). Each slice of the object is then associated to a location  $\vec{p}_0$  on the spline  $\vec{f}_{p_0}$ , and the deformation parameters  $\Delta\vec{x}_0$  and  $\vec{\alpha}_0$  are interpolated onto the complete cross-section of the object. Therefore, this method is applicable for, e.g., a beam under bending load or a cube under shear, but not for a surface with buckling or in-plane bending modes of ring cross-sections. Those deformations would require multi-dimensional interpolation methods, which re-approximate the complete surface and not only the centerline.

The spline-based interpolation leads to a group of 9 splines, one for each component of the set  $\Delta\vec{x}_0$ ,  $\vec{\alpha}_0$  and  $\vec{p}_0$ . Each spline  $f(s_f)$  is here defined by piecewise cubic sections  $f_i(s_f)$  over the discrete values  $F_i$  and with the spline parameter  $s_f$ , (3-10).

$$f_i(s_f) = a_i + b_i \cdot s_f + c_i \cdot s_f^2 + d_i \cdot s_f^3 \quad \forall s_f \in [i, i + 1) \quad (3-10)$$

The assumption of cubic sections correlates with a bending shape according to beam theory. With the condition of continuity up to the 2<sup>nd</sup> derivation, a linear set of equations is defined for the coefficients  $a_i \sim d_i$ , (3-11).

$$\begin{aligned} f_i(s_f = i) &= F_i, \quad f_i(s_f = i + 1) = F_{i+1} \\ \frac{df_{i-1}}{ds_f} &= \frac{df_i}{ds_f}(s_f = i), \quad \frac{d^2f_{i-1}}{ds_f^2} = \frac{d^2f_i}{ds_f^2}(s_f = i) \end{aligned} \quad (3-11)$$

Special attention has to be paid to the endpoints of the spline  $s_{end} \in \{1, n_{Marker}\}$ . A natural spline with 0 curvature at the endpoints, (3-12), as closure condition is used for the reference point splines  $\vec{f}_{\vec{p}_0}$  and the rotation splines  $\vec{f}_{\vec{\alpha}_0}$ .

$$\frac{d^2 f_i}{ds_f} = 0 \quad (3-12)$$

However, using a natural spline as closure condition for the translational splines  $\vec{f}_{\Delta\vec{x}_0}$  would result in a change in the angle between two adjacent objects as sketched in Fig. 3-6. This would lead to an unphysical change in the flow pattern within this area for bend-dominated structures. Therefore, a more sophisticated definition is required. With the aim to maintain the adjacent angle, the gradient  $grad(\vec{f}_{\Delta\vec{x}_0})$  could be defined based on the local rotation  $\vec{\alpha}_0$ , but the absolute value of the gradient  $|grad(\vec{f}_{\Delta\vec{x}_0})|$  remains undefined. As sketched in Fig. 3-6 for three different absolute values of the gradient, the interpolated shape is subsequently not distinct.

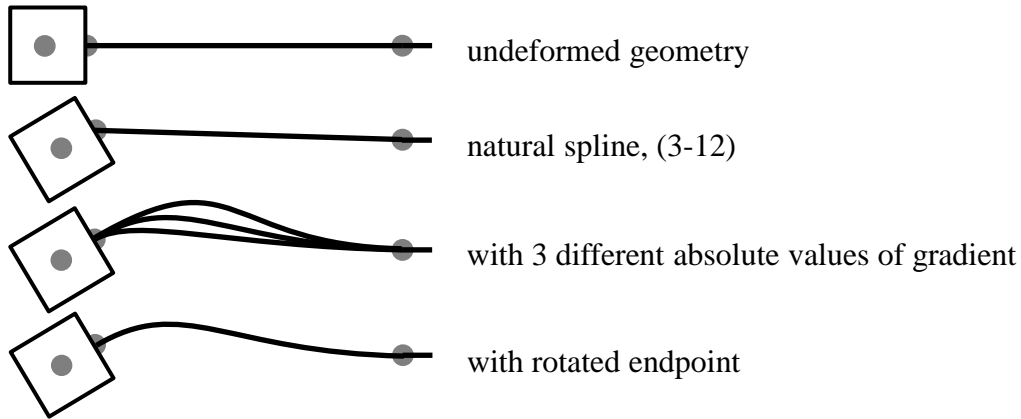


Fig. 3-6: Change of angle between adjacent objects with different spline definitions under deformation

Therefore another approach was chosen here, defining a location  $\vec{p}_{dir}$  in a finite distance  $ds \rightarrow 0$  to the endpoints of the splines,  $\vec{p}_{dir} = \vec{f}_{\vec{p}_0}(s_{end} + ds)$ . This virtual location is then treated as being a rigid object and transformed based on the above given coordinate transformation, (3-9), with the transformation parameters of the endpoint, (3-13). This result is then used to calculate the location's translation  $\Delta\vec{x}_{s_{end}+ds}$  as passage point for the translational splines  $\vec{f}_{\Delta\vec{x}_0}$ , (3-14).

$$\Delta\vec{x}_{s_{end}+ds} = \mathbf{A}_{TR}(s_{end}) \cdot (\vec{p}_{dir} - \vec{p}_0(s_{end})) + \Delta\vec{x}_0(s_{end}) \quad (3-13)$$

$$\vec{f}_{\Delta\vec{x}_0}(s_{end} + ds) = \Delta\vec{x}_{s_{end}+ds} \quad (3-14)$$

This method treats the end of the spline therefore not as being rotated, but like a beam with two support points close together at the endpoint. Due the similarity of the cubic splines and the solution of the beam theory, the interpolated shape approximates the bending of a beam, and the issue of the undefined absolute value of the directional vector subsequently does not occur.

To identify the local interpolated values for an arbitrary location  $\vec{p}_{loc}$ , a value  $s_{loc}$  has to be found, indicating the corresponding location on the splines. This value  $s_{loc}$  is defined here to be the closest location from  $\vec{p}_{loc}$  to the interpolated reference location  $\vec{p}_0$ , and thus the closest point on the spline set  $\vec{p}_0(s_{loc}) = \vec{f}_{\vec{p}_0} = [f_{x_0}, f_{y_0}, f_{z_0}]$ , (3-15).

$$\frac{\partial}{\partial s_{loc}} |\vec{p}_0(s_{loc}) - \vec{p}_{loc}| = 0 \quad (3-15)$$

This closest point is found by solving the equation with a Regula Falsi bi-section solver. Using the  $s_{loc}$  value as location, the deformation parameter set  $\Delta\vec{x}_0$ ,  $\vec{\alpha}_0$  and  $\vec{p}_0$  can be derived, (3-16). As the reference location is defined to be constant over time, the value  $s_{loc}(\vec{p}_{loc})$  is also constant. Therefore, it can be calculated once in the initial iteration, stored in the memory and only  $\Delta\vec{x}_0$  and  $\vec{\alpha}_0$ , and its splines need to be recalculated.

$$\begin{aligned} \Delta\vec{x}_0(\vec{p}_{loc}) &= \vec{f}_{\Delta\vec{x}_0}(s_{loc}) = [f_{\Delta x_0}, f_{\Delta y_0}, f_{\Delta z_0}] \\ \vec{\alpha}_0(\vec{p}_{loc}) &= \vec{f}_{\vec{\alpha}_0}(s_{loc}) = [f_{\alpha_0}, f_{\beta_0}, f_{\gamma_0}] \end{aligned} \quad (3-16)$$

#### 3.2.4.4 Limitations and Practical Application of the Mapping Strategy

The methodology of spline-based interpolation has been described above for a single object. However, typically multiple objects are connected in practical applications, e.g. three rotor blades are attached to the hub, or the nacelle is attached to the tower. To use the method in such cases the spline methodology would have to be extended into the multi-dimensional space with a spline parameter vector  $\vec{s}_f$  with two or more components. This step would increase the complexity of the calculation significantly. Therefore, it is preferably to find a workaround for this issue. The method used in the present research, is to define connecting objects as sketched in Fig. 3-7. The surface of this connecting object is assumed to be in a rigid motion. The structural flexibility of the connecting object is still taken into account in the structural solution, however not on the local grid motion in the CFD.

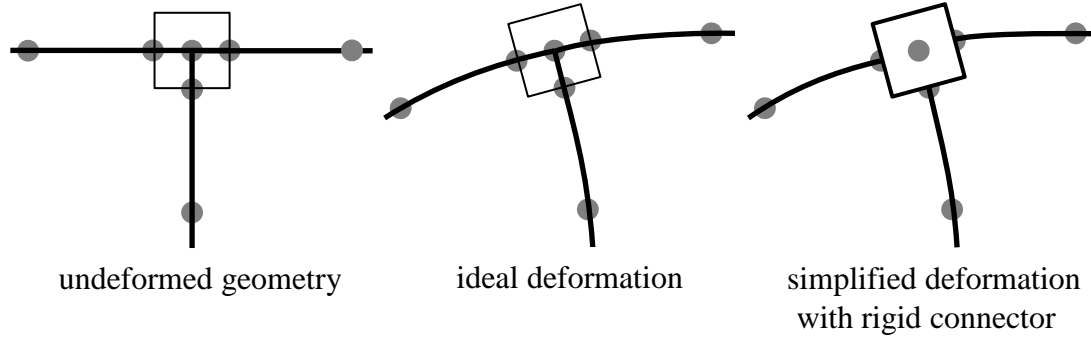


Fig. 3-7: Mapping strategy for interconnecting beam-shaped objects

This is a workaround, which will lead to small errors in the surface location. The error increases with the flexibility of the object modelled as rigid motion. However, this error is limited to the first section of the spline and the flexibility of those interconnecting objects is usually small compared to the neighboring parts. Therefore, considering also the inherent inaccuracy level of the spline approach, this error is assumed acceptable small for the present research.

Another source of errors within the application of the spline mapping strategy is the size and relative position of the surface regions, associated to the communication marker locations. The intuitive position would be to place each marker in the center of the region, Fig. 3-8 (left). Yet, for the first and last section of the spline this leaves an area out of range of the spline, which has subsequently no interpolated data associated. In the present implementation, missing data is extrapolated by associating all surface locations out of range of the spline to the spline's endpoint if required, resulting in a rigid body motion of those regions.

This extrapolation does not match the calculated motion in the structural solution. Especially in the case of adjacent objects, this would result in jerks and overlaps of the surface and the grid. The extrapolation is therefore prevented in the present research by setting the marker location not in the center of the surface region, but at its outer limit. The additional bending moment caused by this displacement can be countered by another moment as shown in the structural translator. In spite of the global loads being the same, the local inner bending loads tend to be under predicted. Thus, the local deformation of the structure is smaller. Fig. 3-8 (right) shows an example for the relative error  $\varepsilon$  in the tip deflection  $\Delta x_{tip}$  of a cantilever beam with constant distributed load. In both cases, with central or excentrical marker locations, the deflection of the beam is smaller than the theoretical prediction. This discretization error can be reduced by increasing the number of markers  $n_{marker}$ . The choice

of the number of markers is therefore a tradeoff between the intended precision of communication and effort to set up the simulation as will be further discussed in Section 4.1.

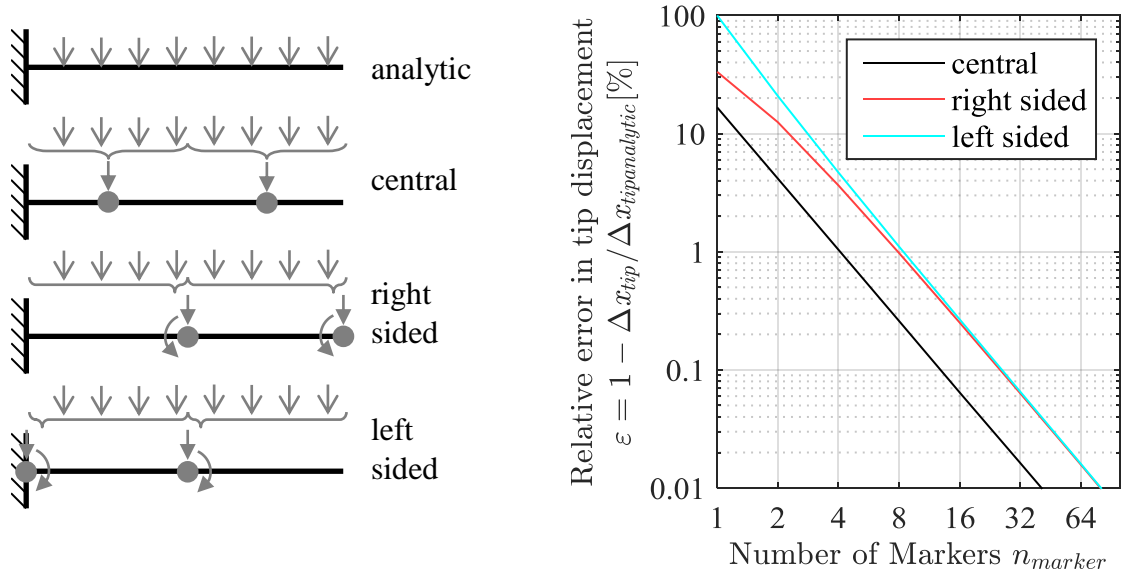


Fig. 3-8: Relative error  $\varepsilon$  due to change in relative position of associated communication markers and surface regions on a cantilever beam example (left:  $n_{marker} = 2$ )

### 3.2.5 FMBI Implementation

The FMBI has been implemented for the tools CFX and Simpack. The following section introduces some of the central topics of this implementation. Further details on the implementation are summarized in Appendix A and in the code documentation.

#### 3.2.5.1 Transfer Memory

As defined in Section 3.2.2, the transfer memory is based on files either on a physical or virtual hard drive. The data is thereby split into files associated to the simulation runs by their names and identified by the file ending. It was found feasible here to group the coupling informations into the categories of the empty \*ready files, indicating a specific point in the process by their existence, and the data carrier files, which transport the coupling information between the tools. To maintain simplicity all files were defined as ASCII-files, as the amount of communicated data is small enough and the ASCII-files are maintenance friendly during development.

### 3.2.5.2 CFX-UserFortran

CFX is a closed code, dedicated to be used in industry without custom changes to the code. However, there are two interfaces in CFX to incorporate custom Fortran codes: The command expression language (CEL), and the junctionbox routines, which are both used to implement the present coupling. The CEL type of code is evaluated during the iteration on each grid element and used here to apply the fluid translator. The CEL is coupled in CFX via the memory management system (MMS) to the junctionbox routines, which run once between the iteration steps. The MMS is further used within CFX to distribute the communication between the parallel environment of the simulation. Therefore, the communication is implemented as junctionbox routines to result in a single point of contact for the coupling.

### 3.2.5.3 Simpack-UForce

Simpack is similar to CFX a closed commercial code, also with an interface for user specified Fortran code. These UForce functions are treated by Simpack as additional force elements, applied to the system and are therefore evaluated during each inner integration step. In the present case, all functionalities of the coupling on the structural side are merged into a single function, which is used for both, measuring and sending the deformations, and receiving and applying the hydrodynamic loads.

### 3.2.5.4 Moderator

The moderator is the heart of the coupling and controls the procedure and convergences. It is written as a Perl-script. As shown in Fig. 3-9, the moderator script contains two loops: One for the iteration and relaxation of the implicit solution within each time step, and one for the transient simulation. Both operations are based on reading, interpreting and modifying the files in the transfer memory.

Additionally, the moderator also stores copies of all converged time step communications during the simulation. These intermediate results are used at the end of the coupled simulation to perform a Simpack time integration, which covers the full time duration of the coupled simulation. This step is not relevant for the coupled simulation itself, but due to the repeated start-stop of Simpack, cf. Section 3.2.1.3, a contiguous structural result file is missing. This is generated with the final Simpack integration.



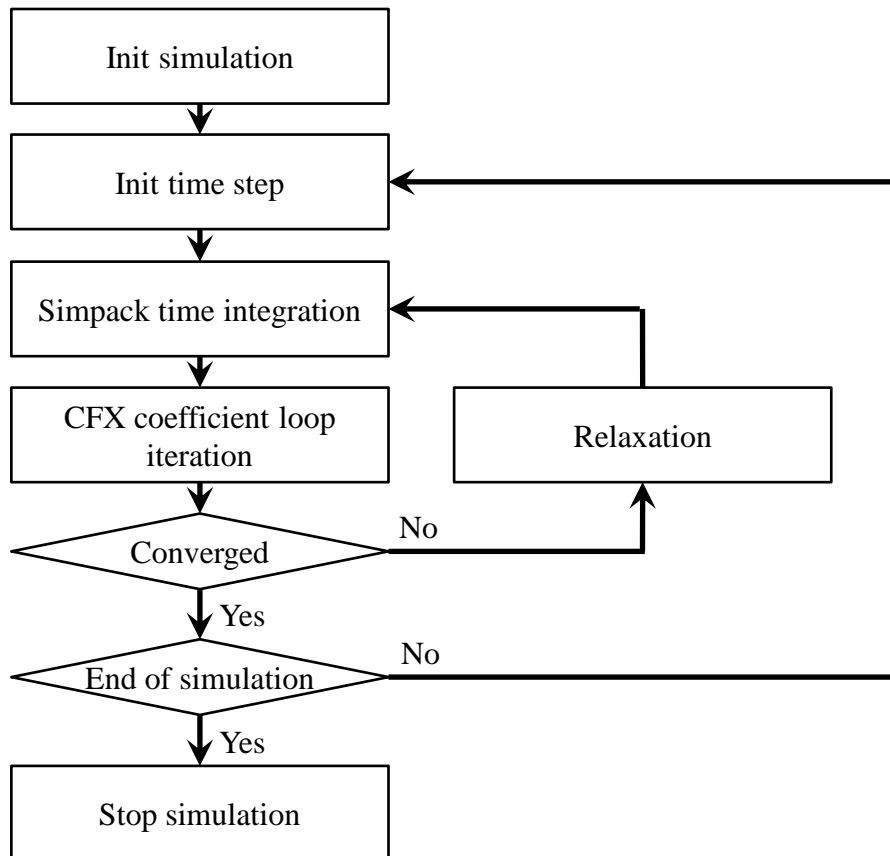


Fig. 3-9: Workflow of moderator script in FMBI coupling

### 3.2.6 Summary of the FMBI-Method

Within this section a coupling methodology between the commercial codes Ansys CFX and Simpack has been developed. This method couples the CFD to a general multibody system to set up a fluid-multibody-interaction (FMBI) simulation environment. The FMBI is a fully implicit, strong coupling of CFX and Simpack. The coupling can be applied to rigid and/or flexible objects by means of a spline interpolation method. It is therefore able to simulate complex systems and interactions efficiently.

In the current state of development, the flexible objects are limited to beam-shaped objects or combinations of those, which is sufficient for the applications in this research project. In a future development, the FMBI coupling can be extended to, e.g., membrane-shaped objects by extending the spline method to a multi-dimensional form. It needs to be mentioned that the method presented here has been extended by fellow researchers within another project, replacing the CFX code with the free vortex code WinDS, [45], and is also transferred to the Flower research CFD code replacing the previous Flower-Simpack coupling of [54].

### **3.3. Validation and Verification of the FMBI**

Before using any simulation method, it needs to be verified and validated first. In this process, it is not only necessary to identify any discrepancy between the model and the reference data, but also to identify the section within the code or method that is responsible for the identified misalignments. Therefore, the aim of this section is to present a set of basic validation cases and its application for the validation of the FMBI.

By splitting the FMBI method into its key data of forces, moments, translations and rotations, each part of the coupling can be validated isolated with a specific validation case. Each of these cases consists of a free decay pendulum in water. To gather the experimental reference data, the cases are set up in a water basin and the motion over time is recorded with an optical measurement system. In the second step, the validation cases are set up in the FMBI and simulated accordingly. The motions from numerical simulation and experiment are compared and used to draw conclusions on the data integrity of the measurements and the validity of the FMBI code.

#### **3.3.1 Methodology of Validation**

Validation and verification are addressing the same question, i.e. whether a simulation code is able to reproduce the correct results. However, there is a distinct difference. As outlined by [65] verification is the comparison to a known (numerical or analytical) solution, while the validation is the relationship between a simulation and the real world. Thus, any developed code needs to be validated to prove its applicability and can be verified to benchmark it to the state-of-the-art simulation codes.

##### **3.3.1.1 Cases in Literature**

Literature holds a large variety of validation and verification cases for CFD and structural simulations. Still, cases applicable to coupled fluid-structure validation are much rarer and often highly complex. This might be the result of the source of the reference data: As experiments are expensive in most cases, they are designed to answer a specific technical question, e.g. on the dynamic motions of floating wind turbines, [44], or on the aerodynamics of a wind rotor, [76]. The validation of a tool is then a later step towards the aim of reaching, e.g., a numerical wind tunnel in a computational lab. Therefore, the validation process itself is rather difficult, as the result is the magnitude of deviations to the data and it is not clear,

whether the reason for this deviation is a bug in the coupling code or in one of the simulation programs, a sub-optimal model setup or measurement errors.

This effect is amplified for validation based on data from full-scale testing. In this case, the incoming disturbances are not known in most of the cases and it is only possible to compare the statistics, e.g. [15] and [41]. However, calculating stochastic loads requires a large time duration to be both measured and simulated. In the present case of FMBI simulations of a tidal current turbine, neither of these data are available or feasible.

On the other hand, a large variety of cases are specifically designed for verification of the codes by means of a code-to-code (C2C) comparison, e.g. [13], [73], [80] and [83]. These cases fulfill the step of verification, but not the step of validation, as defined above. In some of these C2C cases measurements in the laboratory are added. However, this often leads back to the same problem of complex cases, e.g. [46] and [72], and the results from the validation study are non-conclusive.

### 3.3.1.2 Difference of Code and Model Validation

To avoid those issues, the method used in this research inverts the logical approach of a model validation, resulting in the code validation procedure. The traditional model validation concludes from the information that the model is valid to the information that the fluid, the structure and the coupling implementation are valid for the application, (3-17). Vice versa, the code validation states that if the three implementations and setups are valid, then the model is also valid.

$$Model\ validity \cong \begin{cases} + & Fluid\ validity \\ + & Coupling\ validity \\ + & Structure\ validity \end{cases} \quad (3-17)$$

The validation is therefore split into the three single validations. The validation of the fluid and structure is still application dependent and needs to be redone after a change in application. Yet, this step should be done anyway for new applications of the two tools. The advantage of the code validation is that those tool validations can be limited to single-physic validation cases, which are much simpler than multi-physic experiments.

On the other hand, the validity of the coupling implementation is independent of the application. Therefore, it does not need to be redone upon a change in application but can be transferred without limitations. Subsequently, the cases chosen for the validation of the

coupling implementation are neither bound to an application. Therefore, the cases can be designed to fit the needs of the validation itself.

Given the validity of the standalone fluid and structure solution for a specific application and a previously done validation of the coupling implementation, the coupled simulation for this application is valid. For the equations and codes of the coupling, there is no difference between vortex-induced vibrations, rotor blade oscillations, wave slamming, etc. Therefore, the validation shown here is a general-purpose validation of the method, but not of the model.

### 3.3.2 Developed Validation Cases

Based on the lack of suitable validation cases in the literature, a new set of validation cases is defined here. Each of them is specifically designed to validate a single aspect of the coupling between previously validated fluid and structural codes. There is no technical question answered except the validity of the coupled hydroelastic toolchain. Subsequently, there is no concern regarding the model scale, as the equations and code of the coupling are case- and scale-independent. Furthermore, the available measurement equipment and facilities need to be taken into account for the design of the validation cases.

#### 3.3.2.1 Design of the Validation Cases

Following the above-discussed issues, three guidelines for the design of the validation cases can be inferred:

- Limit the complexity of the interaction to a single new part of the coupling with each experiment to simplify the search for possible bugs in the code.
- Limit the complexity of the standalone fluid problem and the structure problem to prevent unintended additional issues.
- Limit the complexity of the measurement, and match the experiment to the measurements.

Based on these guidelines, the simplest structural problem is the motion of a pendulum. Further, a pendulum has the advantage of being a rather precise combination of loads and motions. To result in a significant impact of the fluid on this pendulum motion, the pendulum can be placed in a fluid with approximately the same density as the structure. As pendulums experience large amplitudes of motion, an optical measurement system, based on a camera

and image processing, can be used. These thoughts lead to three experimental setups as summarized in Table 3-1 and detailed in Section 3.3.3.1.

Table 3-1: List of validation experiments

No.	Model	Fluid load	Type of motion
1	Spring pendulum	Force	Translation
2	Gravity pendulum	Moment about the pivot point	Rotation about the pivot point
3	Bending pendulum	Force, moment combined	Flexible surface deformation

All experiments are performed in air for the baseline behavior and with the pendulum body fully submerged in a water basin with glass walls to measure the impact of the fluid-structure-interaction. These experiments are recorded by a camera and analyzed with an image-processing algorithm, as sketched in Fig. 3-10. As the frame rate of the camera is limited, the pendulum needs to move slowly enough for a proper recording.

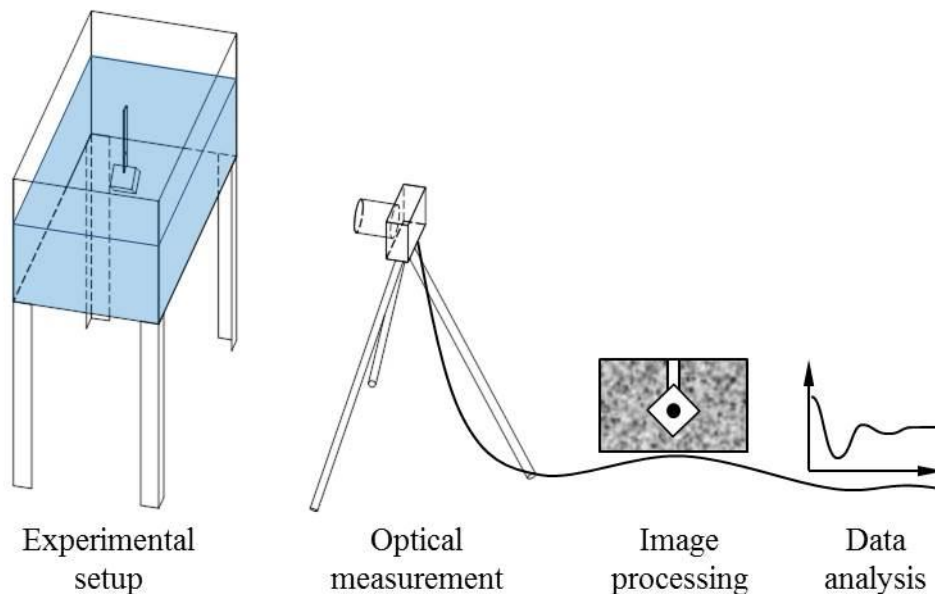


Fig. 3-10: Experimental setup for pendulum experiments

### 3.3.2.2 Validation Procedure

Based on the three specifically designed experiments, it is not only possible to state the existence of eventual bugs in a hydroelastic simulation, but also to locate them within the

code. As shown in the flowchart, Fig. 3-11, the results can be used to validate the code systematically.

Initially the structural and the CFD code should be validated each in standalone, to check their suitability for the validation cases. This can be done by comparing the structural solution to the experiments in air and by comparing it to results found in literature, e.g. [66].

After the initial check has been passed, the validation process with the pendulum experiments can be started. Each validation case provides two characteristic values: The frequency, which can be used to validate the implementation of the coupling method, and the damping ratio, which can be used to check the accuracy of the structural and the fluid setup. By following the steps of the flowchart, Fig. 3-11, the validation of the hydroelastic method can be carried out based on four pendulum simulations.

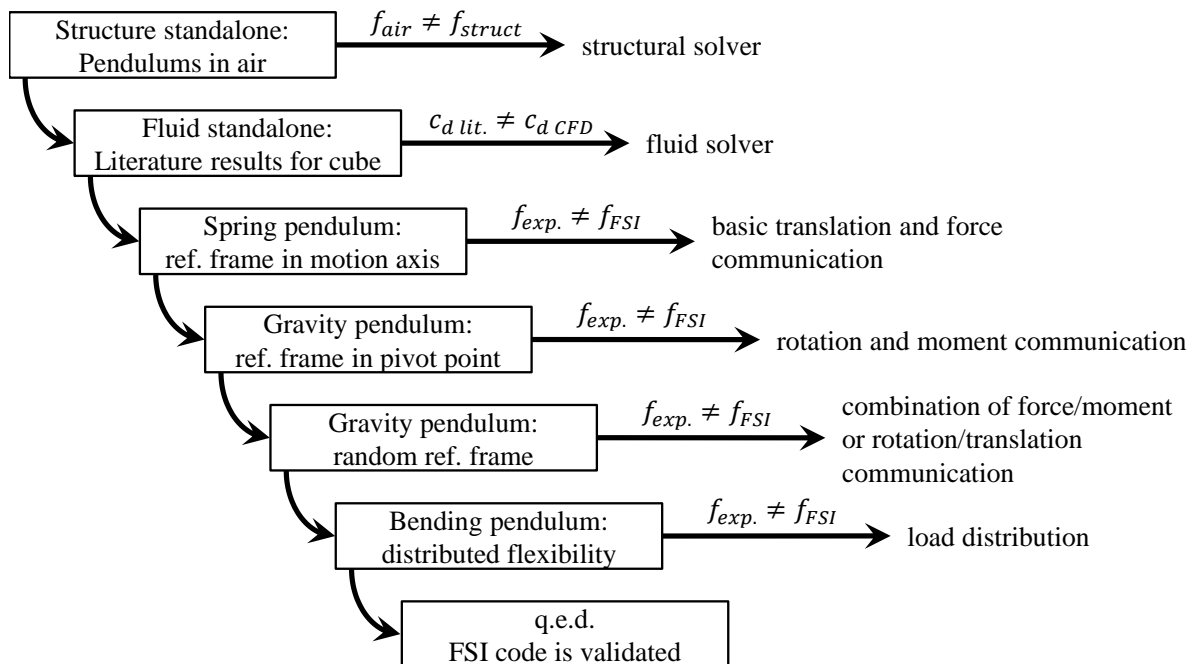


Fig. 3-11: Validation procedure based on the free decay pendulums and detected location of bugs in case of deviation

The gravity pendulum is thereby used twice: Once with the reference frame of communication in the pivot point, and once with the reference frame in an arbitrary, random location. While the first case is a pure coupling of a moment and a rotation, the latter case results in a combination of forces and moments respectively translations and rotations. Therefore, both cases should give the same results and both can be compared to the same gravity pendulum experiment.

However, one needs to keep in mind that this is only a validation of the code, the transformations of loads and motions, and the implementation. It is not a validation of the setup for any specific purpose. To use it on a specific purpose, e.g. vibrations of a turbine blade, the CFD and structural model should be validated in standalone in addition.

### 3.3.3 Experimental and Numerical Setup

Within this section, the above given analysis of the validation methodology is transferred to its practical application. This consists of three main parts: The experiments, the numerical model, and the calibration of both.

#### 3.3.3.1 Pendulum Objects and Basin

Fig. 3-12 shows the experimental setup. The setup consists of a stiff frame, assumed to be rigid, used as attachment point for the spring and gravity pendulum above a water basin. The bending pendulum is attached to a gravity base at the bottom of the basin. The water basin is a glass aquarium with a cross-section of  $788 \times 338 \text{ mm}$  and a maximal water depth of  $394 \text{ mm}$ . The larger the basin, the lower is the impact on the flow around the pendulum. According to [16] and [87], a wall or water surface vicinity is negligible for a sphere with radius  $r_{sphere}$  at a distance larger than  $3 \cdot r_{sphere}$ . The size of the basin therefore allows for a reasonable size of the pendulum object with  $r_{pendulum} \leq 5 \text{ cm}$ , while being still small enough to be handled.

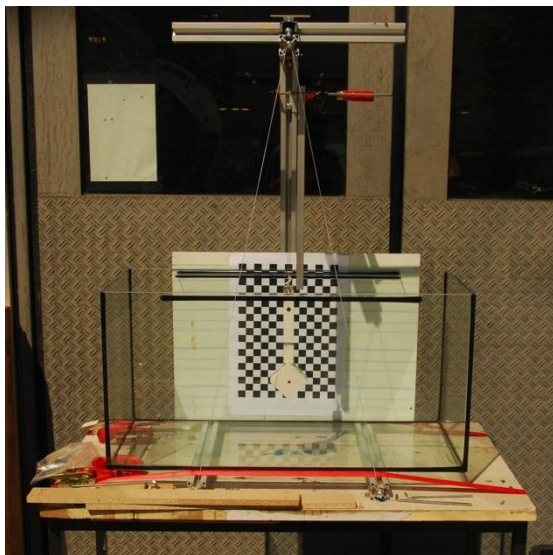


Fig. 3-12: Image of experimental setup for spring pendulum (left) and bending pendulum (right) in air (basin not yet filled with water)

One of the most difficult tasks in hydrodynamics is the prediction of the separation point for curved surfaces. Therefore, the pendulum objects are chosen to be cuboids with sharp edges, and subsequently predefined locations of flow separation. This limits the complexity of the experiment without impact on the outcome of the validation procedure. For the spring and gravity pendulum, the same cube with an  $\beta_{cube} = 45^\circ$  inclination is used, as shown in Fig. 3-13. The cube has an edge length of  $l_{cube} = 6\text{cm}$ , which is well below the size limit given above, and consists of cast resin with a density of  $\rho_{resin} \approx 1220\text{ kg/m}^3$  close to the density of the fluid,  $\rho_{fluid} \approx 1000\text{ kg/m}^3$ . The strength of the spring and the length of the rod were both chosen such that the pendulum has an eigenfrequency in air of  $f_{air} \approx 1\text{Hz}$  and, due to the surrounding fluid, a lower frequency in water  $f_{water}$  as will be discussed in Section 3.3.4.

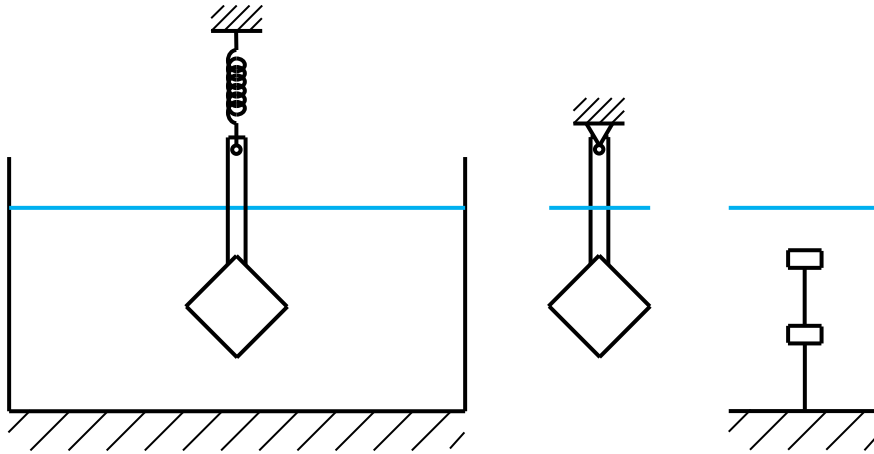


Fig. 3-13: Sketch of the experimental setups for validation (not to scale)

The bend pendulum similarly consists of cuboid parts and is manufactured from spring sheet steel with two additional masses added. This setup results in the 1<sup>st</sup> eigenfrequency in air of  $f_{air} \approx 5\text{Hz}$ . This frequency of motion is at the limit of the measurement system, described in the next section. However, a lower eigenfrequency was not feasible for this pendulum, due to the mechanical stability.

Fig. 3-14 shows an analysis of manufacturing inaccuracies for both pendulum objects. As can be seen, minor deviations in the surface geometry occurred, but are within the acceptable ranges. The largest deviations are side-side displacements of, e.g., the mass blocks on the bend pendulum. The full geometric details of the pendulums can be found in [A 3].



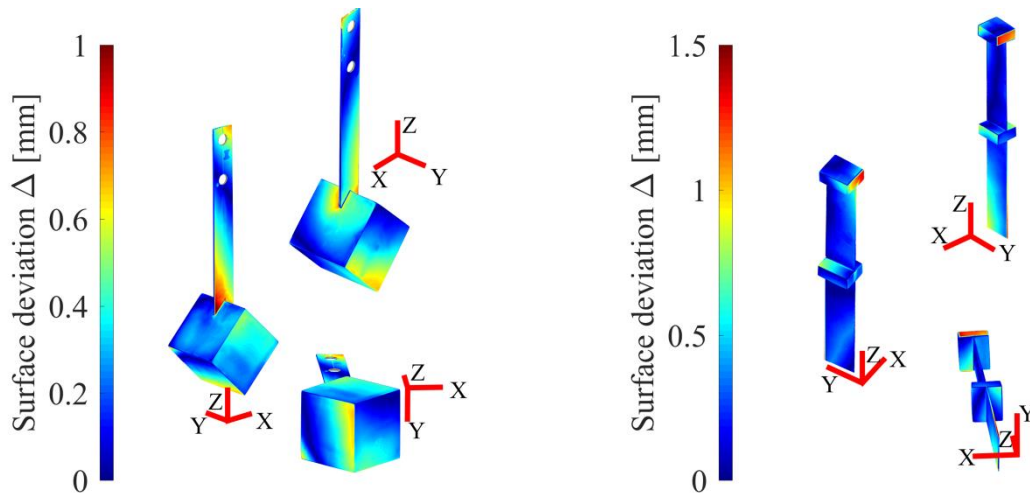


Fig. 3-14: Surface deviation  $\Delta$  from design geometry of pendulum objects

### 3.3.3.2 Optical Measurement System

For the validation, the position of the pendulums over time needs to be measured. This is carried out here with an optical measurement system, which has the advantage of non-interfering data acquisition. In the present setup a camera is placed in front of the water basin, the motion is recorded in a video, and each frame is analyzed with an image-processing algorithm. To prevent issues with reflection and lens effects of the basin wall, the system was set up as rectangular as possible.

The quality and type of the camera system is of dominant relevance for the feasibility of this type of measurement. The output shall be high-resolution images with a high frame rate and without motion blur. Especially the latter requirement is critical for the choice of the camera system, as a slight motion blur often makes a video more pleasing to the human eye. Thus, many commercial cameras intentionally tolerate motion blur to a certain extent, which is not acceptable for the present application. A Canon 600D digital-single-lens reflex camera (DSLR) with a short exposure time of  $1/2.000s$  and 50 frames per second at a 720p resolution was found to be the best compromise between cost and quality.

For the image processing various options are available in literature, e.g. pattern recognition for counting persons in a video. However, those methods are often difficult to implement and use. Thus, a simpler approach was chosen here that fulfills the purpose of the application. A red dot was painted on the pendulum's surface as a tracer, which is then tracked by an image-processing algorithm. This is sketched in Fig. 3-15 starting top-left with the baseline image,

which is a snapshot from the video stream of the camera. This baseline image is split into the three RGB-colors (red, green and blue) and then combined to a greyscale image with a variable weighting of the colors, (3-18). The resulting greyscale image is dark on all locations with a red color portion in the original image and bright on all others. Turning it into a black/white image with a threshold value turns the red tracer dot into a black circle and eliminates most of the rest of the image. By limiting the search region to an area close to the last know position of the tracer dot, this reduces the image-processing step therefore to finding a black circle on a white background. This step can be done efficiently with the circular Hough transformation, [8], to compute the center location of the tracer dot. This transformation also computes the radius of the tracer, which is used for the check of the data integrity, as a mismatch of the calculated radius of the tracer with the known size indicates an error in calibration or image processing.

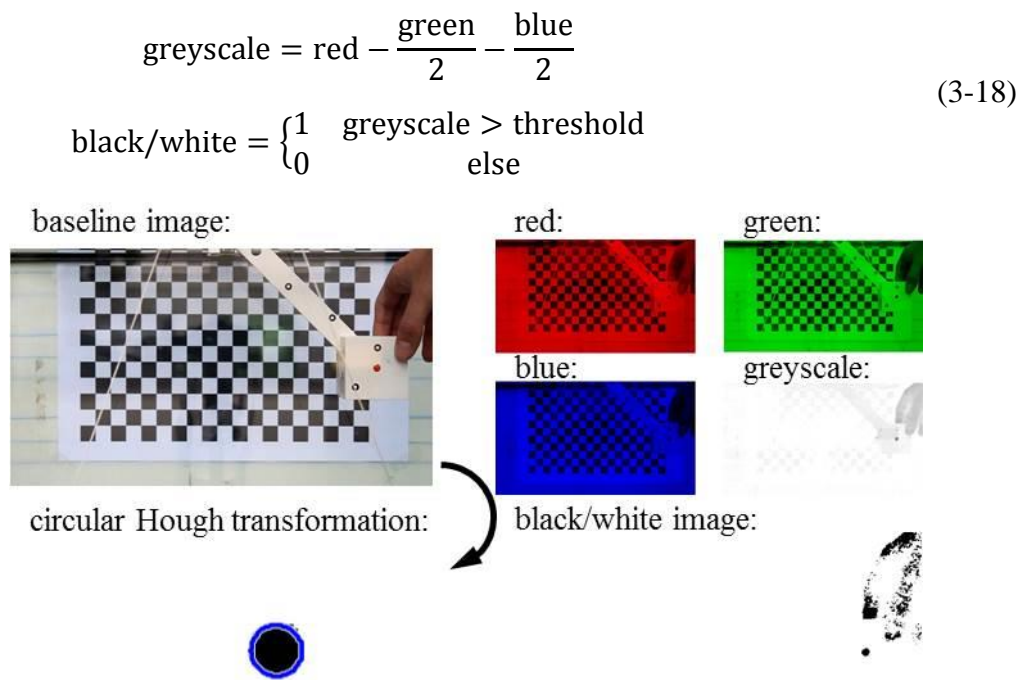


Fig. 3-15: Image processing steps for optical measurement system

### 3.3.3.3 FMBI-Model Setup

The numerical model of the pendulum is based on the previously introduced coupling of Simpack and CFX. For the CFD setup, the geometry of the pendulum is idealized to the design geometry, i.e. manufacturing inaccuracies, the rod, the basin walls, the free surface, etc. are neglected. Furthermore, the problem is assumed to be symmetrical to the plane of

motion of the pendulum. Fig. 3-16 shows the resulting high quality hexa-grid with about  $800 \cdot 10^3$  elements, which is used for the spring and gravity pendulum. The grid for the bending pendulum is of similar quality. The time resolution is chosen here to be ca. 1000 time steps per oscillation period. A grid and time step independence study showed that these values are far above the minimal requirements. E.g., on the required time step resolution, as low as 10 time steps per oscillation period are sufficient to provide acceptable results for the frequency. However, the calculation of the damping ratio of the pendulum requires a higher number of time steps. The turbulence is modelled with the shear stress transport (SST) model.

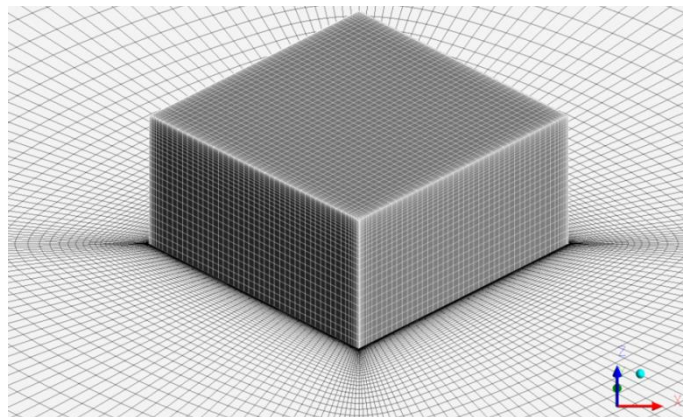


Fig. 3-16: Grid for spring and gravity pendulum

The structural model contains the geometry and dynamic parameters of the pendulums. In the case of the bending pendulum, they are modelled with the linearized beam theory. For the spring and gravity pendulum rigid body dynamics are assumed. Due to the neglected free surface, the fluid solution does not account for the buoyancy. This buoyancy load is therefore applied on the structural model as either constant or position dependent force. All solver parameters and other settings are maintained to default values.

#### 3.3.3.4 Calibration

As the properties of the experimental setup do not exactly match the design parameters, the FMBI model needs to be calibrated. This calibration is done based on the in-air experiments with the assumption of a negligible impact of the surrounding air. The parameters calibrated here are the mass of the pendulum, the spring stiffness, the inertia and the bearing friction for the spring and gravity pendulum, and the mass and structural damping for the bending pendulum. These parameters are adapted based on the static deflection, the eigenfrequency and the damping ratio. During calibration, all parameters remained well within the expected range of manufacturing and material tolerances.

A second calibration is required for the optical measurement system. This calibration deals with the two aspects of the measurement's scale and optical distortion. Both are measured by placing a rectangular chess-pattern test sheet in the plane of motion of the tracer on the pendulum. The image of this test sheet, taken at the start of each measurement, is then compared to its known geometry. Hence, the pixel-to-millimeter scale factor can be determined, as well as the distortion can be measured. Due to the rectangular setup and the type of the lens, the distortion was in the range of one to three pixels. This is sufficiently small for the present application, and the calibration of the measurement system needs to apply only the pixel-to-millimeter scaling factor.

### 3.3.4 Comparison of the Experimental and Numerical Results

#### 3.3.4.1 Standalone Validation

As introduced in the validation procedure, cf. Fig. 3-11, the two solvers Simpack and CFX need to be validated first in standalone for the present validation procedure. In the case of Simpack, this has been already done in the calibration step. The experiments in air have been compared to the Simpack results, and the validity of the solver, as well as the integrity of the data, is shown by the agreement of the structural parameters to the design values within expected tolerances.

In the case of CFX, on the other hand, additional results are required. The two main contributions to the hydrodynamic load in the validation cases are the added mass, as introduced in Section 3.1.1.2, and the vortex shedding and drag.

The added mass is compared here to the analytical solution from [61] and the drag to the experimental data of [78]. Several parameters have been compared, however for brevity reasons only exemplary results of this comparison are shown in Table 3-2 and Table 3-3. The added mass coefficient  $c_a$  matches the theoretic results very well, while the drag coefficient  $c_d$  and the shedding frequency, shown by the Strouhal number  $Sr$ , have a higher deviation. Still, also these values match within an acceptable margin. CFX is therefore valid for the validation cases used here.

Table 3-2: Standalone added mass validation results for CFX

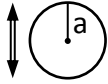

Case	Volume $V$	CFX	Literature, [61]
circle 	$\pi a^2 \cdot dz$	$c_a = 0.99968$	$c_a = 1$
square 	$4a^2 \cdot dz$	$c_a = 1.18657$	$c_a = 1.1885$

Table 3-3: Standalone drag validation results for CFX with Reynolds number  $Re = 200$ 

Inclination	CFX	Literature, [78]
$\beta_{cube} = 0^\circ$	$c_d = 1.365$ $Sr = 0.122$	$c_d = 1.44$ $Sr = 0.166$
$\beta_{cube} = 45^\circ$	$c_d = 1.938$ $Sr = 0.197$	$c_d = 1.97$ $Sr = 0.205$

### 3.3.4.2 Submerged Free Decay Cases

The comparison of the measured data from the basin tests and the FMBI simulation results in two curves with different frequency and damping ratio, which can not be directly compared. Therefore, a harmonic analysis of the first three oscillations is introduced here as basis for the error calculation. For the frequency  $f$ , the peak-to-peak period is calculated and averaged. For the damping ratio  $\zeta_{1-3}$ , the reduction of amplitude  $\Delta x$  is calculated in (3-19). Choosing three oscillations is arbitrary, however proved feasible to take the impact of the linear and non-linear damping into account.

$$\delta_{1-3} = \frac{1}{3} \ln \left( \frac{\Delta x(0)}{\Delta x(3 \cdot 1/f)} \right) \quad \zeta_{1-3} = \frac{\delta_{1-3}}{\sqrt{(2\pi)^2 + \delta_{1-3}^2}} \quad (3-19)$$

For the spring and the gravity pendulum, the simulation and the experiment agree reasonable well, as shown in Fig. 3-17. Both, frequency and damping, deviate a few percent from the measured values. However, in both cases the added mass is slightly under-predicted in the simulation compared to the measured value. This does not match with the observations from the standalone validation in the previous section, which showed a very good agreement between the simulated and analytic added mass coefficients. By taking the free surface of the water basin into account, this mismatch of the data could be partially traced back to the rod of the pendulum and its free surface interaction. Yet, the simulation of the free surface requires a very high grid quality, which is disturbed by the large grid deformations of the pendulum

motion. For this reason, the accuracy of the performed free surface simulation was too low to give conclusive results, and is therefore not further detailed here.

The next step in the validation procedure, cf Fig. 3-11, is the gravity pendulum with a random coordinate frame used for communication of the loads and displacements. Those simulations match perfectly with the simulation with the reference frame in the pivot point. Therefore, the code is validated with respect to forces and moments respectively translations and rotations and their combination.

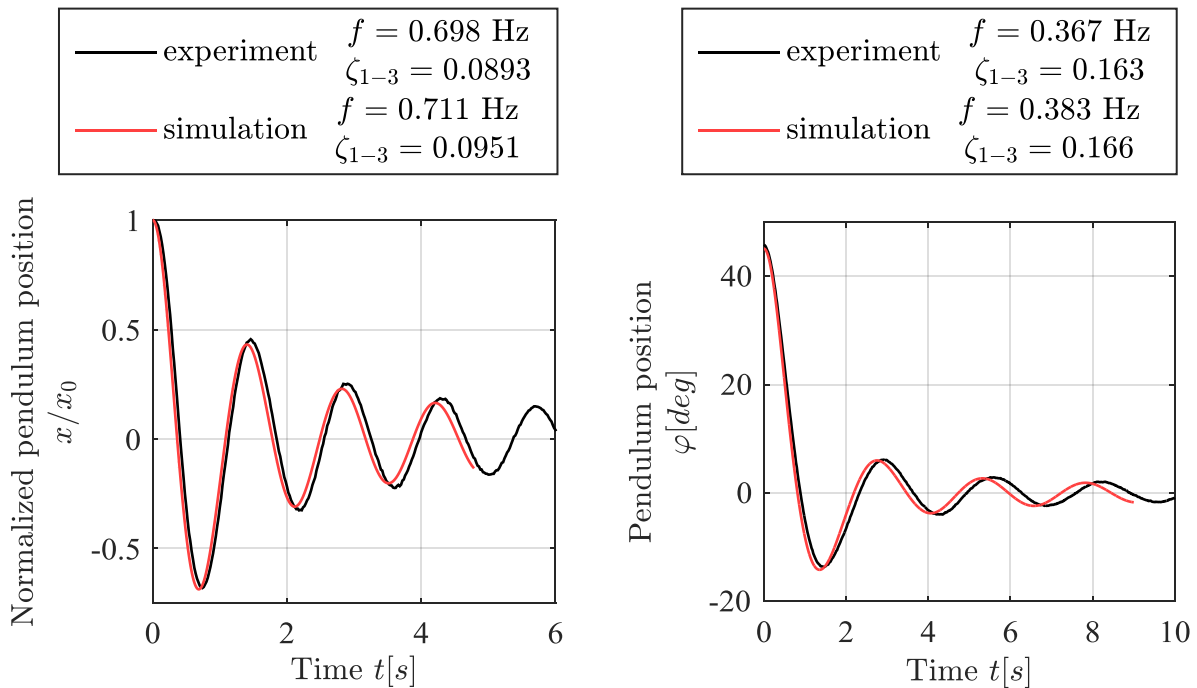


Fig. 3-17: Comparison of the spring pendulum position  $x$ , normalized with the initial amplitude, (left) and the gravity pendulum position  $\varphi$  (right) between experiment and simulation

The last step in the validation procedure is the bending pendulum, Fig. 3-18. This step of the validation includes the full capabilities of the coupled fluid-structure simulations with flexible bodies. Comparing the simulation results of the bending pendulum with the experimental data, a very good agreement can be seen. The 1<sup>st</sup> eigenfrequencies from simulation and experiment have a deviation of ca. 1.2% and the damping ratios differ ca. 2.2%. The coupling of flexible objects is therefore also validated for the FMBI.

As it has been discussed in Section 3.2.4.4, the number of communication markers is critical for the accuracy of the coupling of flexible bodies. This has been tested for the bending

pendulum with 2, 3, 5 and 9 markers. The simulations showed that at least three markers are required for the bending pendulum. In the case of two markers, the deformation of the center of the beam is not transferred. Therefore, the damping is not calculated correctly for the 2<sup>nd</sup> eigenfrequency and the simulation became unstable. The other cases with a higher number of markers had a negligible deviation of less than 0.2% in the 1<sup>st</sup> eigenfrequency. Therefore, the number of communication marker can be set to a reasonable low value and is determined mostly by the desired spatial resolution of the load.

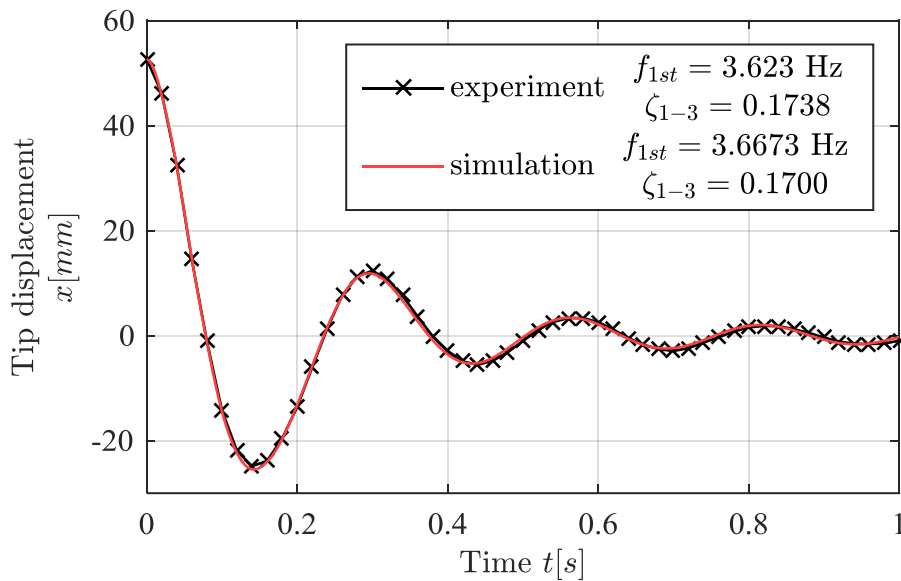


Fig. 3-18: Comparison of the tip displacement  $x$  of the bending pendulum between experiment and simulation

### 3.3.5 Validation of Simpack and CFX for Tidal Turbines

As mentioned in Section 3.3.1.2, the simulation tools Simpack and CFX need to be validated in standalone for the application in order to draw conclusions on the overall validity. However, measured data of reasonable quality is not available for the Voith HyTide<sup>®</sup> turbine. Therefore, the validity can only be inferred here from similar applications.

#### 3.3.5.1 Simpack

For Simpack several validations in the field of wind energy are available. Based on the physical similarity of wind and tidal turbines, it can be assumed that a structural solver valid for wind energy is also valid for tidal energy. There are several validation studies, e.g. [36],

[47] and [90], which show, among others, the validity of Simpack for the present type of simulations.

### 3.3.5.2 CFX

On the fluid side, the same inference is not directly applicable, due to the differences in geometries and size, stiffness and mass ratios. Therefore, the inference of the validity will be shown here in multiple partial steps. In Section 3.3.4.1, the analysis of added mass for 2-dimensional objects has been shown. Due to the similarity of the physical effect, this added mass validity also applies for 3-dimensional objects. For the rotor hydrodynamics no such similarity is present, however CFX has been validated for rotor hydrodynamics by, e.g., [4] and [82] based on measured rotor data. Drag validations of CFX for different shapes and objects, can be also found in literature, e.g. [68].

These validation studies would be sufficient for investigations of the tidal turbine in an upstream configuration with the rotor ahead of the tower, but as will be shown below in Section 4.2, especially the downstream operation with the rotor in the tower wake is of interest for the hydroelasticity. Subsequently, also the ability to model the tower wake needs to be validated. Unfortunately, neither suitable measured data is available for this type of load cases, nor the wake can be considered repetitive: i.e. the wake of the tower depends on several stochastic variables, which change during the operation, and thus the wake changes. These variables are the turbulent inflow, the marine growth influencing the surface roughness, current speed, direction and shear, among others. In addition, the geometry of the tower structure can not be modelled exactly for FSI simulations, as a large number of secondary components such as cables, anodes, etc. are attached to the outside. Validating the tower wake for the deterministic simulations shown here is therefore difficult, as the measured data would have a very large scatter and any alignment of the simulation results would only be an approximation of the ‘correctly’ measured values, [86].

A deeper look into the validity of the tower wake and its impact on the simulation results reveals that the intensity of the tower wake is only a scaling factor on the load amplitudes apparent for the rotor: i.e., an over prediction of the tower wake intensity would cause a similar over prediction of the resultant load amplitude. Considering that the deformations calculated in this research are all small, as will be shown Section 4.3.1, and quite well within the range of linear assumptions, only the quantitative, but not the qualitative hydroelastic results will



change with the tower wake. As long as the present investigation compares only qualitative results and the system behavior, the validity of the tower wake is of secondary importance and any inaccuracies related to the tower wake would not change the findings of the work carried out here.

For the validity of CFX, it can therefore be concluded that the validity of the simulation can only be partially confirmed, but it is sufficiently accurate for the present research. Nevertheless, any comparison of the results must be done within the same setup maintaining the same tower wake intensity. The absolute values of the simulation results need to be treated with caution for the downstream simulations in tower wake and will be subsequently shown only in normalized form, also because of the confidentiality of the turbine data.

### **3.4. Summary of Simulation Methodology**

This chapter analyzed the state-of-the-art simulation methods for the type of hydroelastic simulations to be applied in the present research, and shows a lack of a suitable toolchain. Therefore, a new, coupled toolchain based on the CFD code Ansys CFX and the multibody code Simpack has been developed, closing this gap. This combination of tools allows for an efficient simulation in the required modelling depth to determine the extent of hydroelastic effects.

Both codes used are industrial software packages and therefore without source code access. However, they offer programming interfaces for user written routines. These are used to connect the two single-physic codes with a moderator script coordinating the coupling. This setup forms an implicit, strong coupled system, the fluid-multibody-interaction (FMBI) method. The FMBI therefore communicates bi-directionally, i.e. it updates the surface geometries in CFD and the loads in the multibody solver and iterates these data within each time step till convergence

In contrary to classic FEM based FSI simulation methods, the FMBI does not rely on a local node communication approach but on a discrete location interface with a spline based interpolation methodology. The FMBI has therefore a reduced communication intensity, by sacrificing some model details. The present approach is deemed as a good compromise between computational effort and the required simulation details.

In a third step, the developed toolchain is validated by means of a systematic code validation with dedicated experiments. Compared to the classic model validation approach, the code

validation is split into partial validations of the toolchain, limiting the requirements of the validation experiments. Based on this procedure the essential validity of the FMBI approach is shown. However, the validation of the tower wake is inconclusive. Therefore, the absolute values of the results for the simulations with the rotor in the tower wake should be treated with caution.

---

## 4. HYDROELASTIC SIMULATIONS

The following section focuses on the setup and results of the hydroelastic simulations. After initially introducing the numerical setup, this is done in three steps. First, the hydrodynamic properties of the tidal turbine are investigated considering only the rigid body motion of the rotor. These results are used to describe the hydrodynamic effects of the rotor-foundation-interaction and to analyze the impact of the numerical simplifications, made in the setup.

In the second step of the analysis, a single point of operation is used to compare the results of different setups with a variety of combinations of component flexibilities. This comparison is used for the identification of which components have a significant impact on the turbine system loads, i.e. which flexibilities within the turbine are relevant for design load case simulations. With these results, it can be also identified, which components have the greatest influence on the hydroelastic response and should be optimized.

The section then concludes with an extension to further points of operation with different rotational speeds in the third step. Here, the fully flexible turbine setup is simulated with several rotational speeds to identify the severeness of resonance operations.

### 4.1. Simulation Setup

Based on the previously introduced FMBI-method, the following subsection will briefly introduce the numerical setup, used for the present analysis. Based on the two physics within the FMBI, the introduction is split into the fluid model and the structural model.

#### 4.1.1 Fluid Model

The fluid is simulated with the CFD tool Ansys CFX in the version 14.5 in URANS mode. The setup of this model is divided in the grid, describing the simulated geometry, and the numerical schemes for the spatial and temporal transport and the turbulence.

##### 4.1.1.1 Numerical Grid

With its finite volume approach, CFX relies on high-quality grids, which describe the fluid domain of the system. These grids are created based on hexahedral elements. This type of grid element can be aligned to the flow, reducing the required resolution and thus increasing the numerical efficiency compared to, e.g., tetrahedral elements. However, setting up a high-quality hexahedral grid with good element angles, aspect ratios, volume change ratios, etc.

and an adequate element distribution requires detailed thoughts, to be done efficiently and to result in the minimal required number of grid elements, as shown in the next section. Nevertheless, this effort is considered well spent, as the turbine's geometry is not varied here and the grid strategy can be used for multiple simulations and grid resolutions.

#### 4.1.1.2 Grid topology

The first step in creating a CFD grid is to decide, which size of surface features is to be taken into account. For the Voith HyTide<sup>®</sup> turbine the outer surface contains a large number of flanges, hinges, etc., cf. Fig. 2-8. These are omitted in the present case, as they are not expected to have a strong influence on the hydroelastic responses. Only the major geometry was considered for the grid generation.

The grid for the tidal current turbine is split into four domains as shown in Fig. 4-1. The rotor and stator section contain the respective portions of the turbine system. As in a hexahedral grid, a local grid refinement extends over the full grid domain, the interface and farfield grid domains are introduced to avoid unnecessary fine grid elements in non-essential locations. Thus, this setup results in an efficient grid element distribution. The interfaces between the domains and the rotor stator interaction are based on the general grid interface method (GGI) in CFX, which requires the grid domains to be surface matching. Therefore, the rotor domain has to be circular.

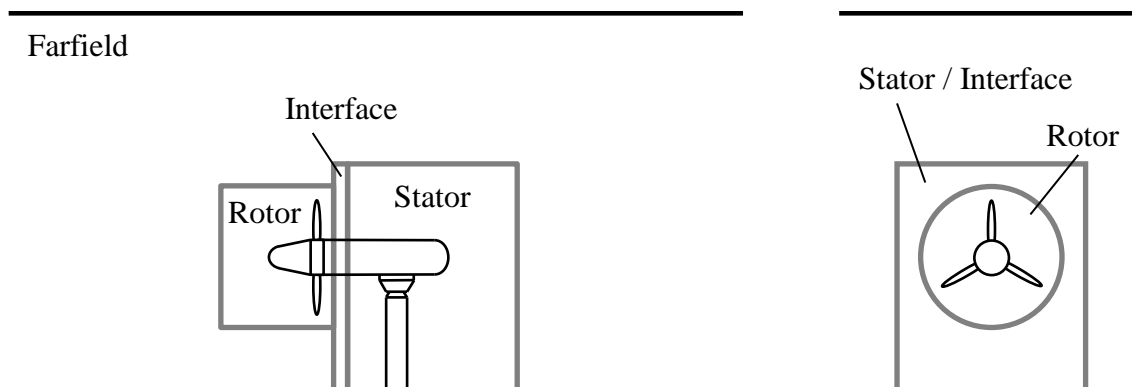


Fig. 4-1: Sketch of global grid topology

The grid is mainly based on O-grid and C-grid topologies, as shown in Fig. 4-2, in order to be aligned to the curved surface boundary layers. The overall cell count for the presented grid is  $9.6 \cdot 10^6$  elements in the baseline setup for the full turbine and  $3.5 \cdot 10^6$  in the coarser and most used setup, as will be discussed in Section 4.2.4 with respect to the trade-off between grid dependency and computational resources. For more detailed stall investigations in

Section 5.3.1 an additional high resolution grid with  $4 \cdot 10^6$  elements for a single rotor blade is set up. All grid domains resolve the boundary layers with at least 15 cells and are designed for  $y^+ \approx 1$  on the rotor blades.  $y^+$  on the nacelle is higher due to the use of a numerical sand roughness model as will be discussed below in Section 4.1.1.4.

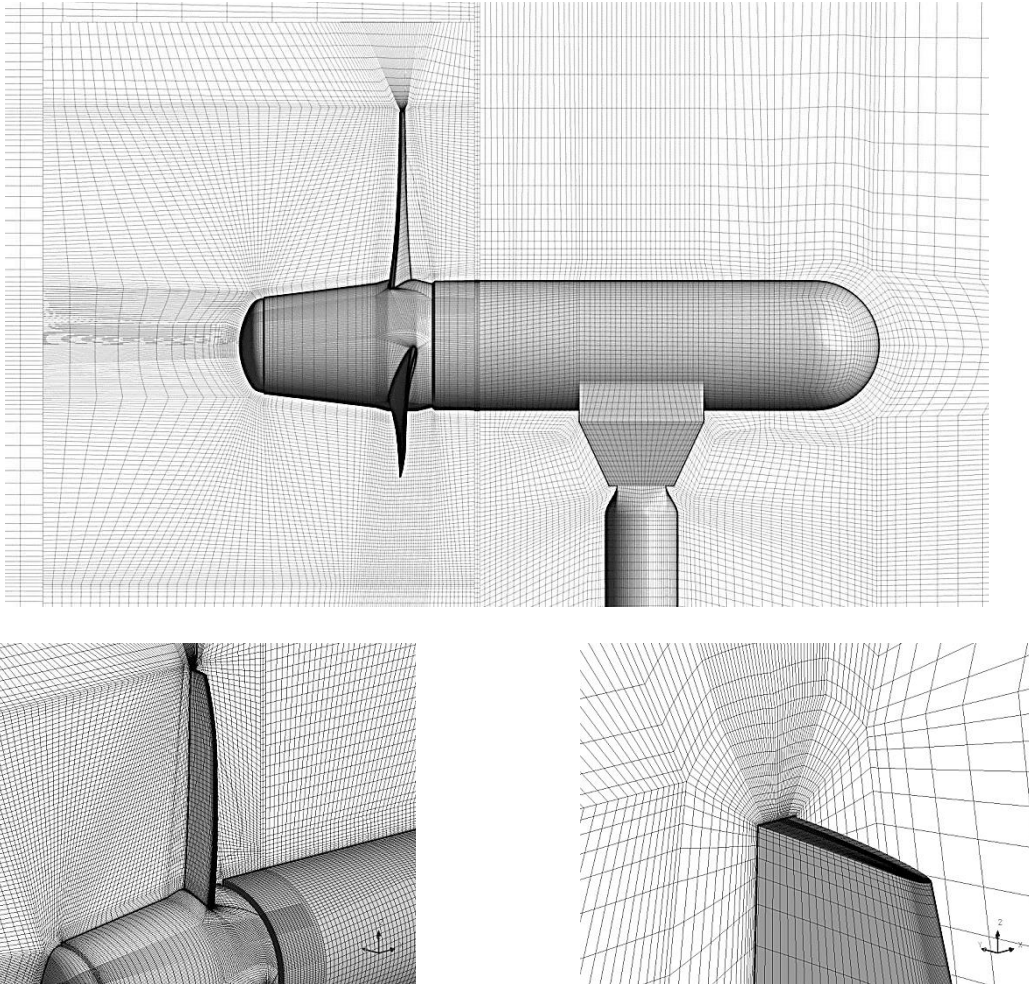


Fig. 4-2: Turbine grid (top) and close up views to the blade and blade tip grid (bottom)

#### 4.1.1.3 Grid Deformation in the coupled FMBI Simulation

Further attention to the grid is required for the hydroelastic simulation. To account for the structural deformations, the grid needs to be deformed as well. This is done with a build-in algorithm in CFX, which morphs the grid node locations based on the surface deformation calculated from the FMBI, and interpolates the field data to this modified grid. Despite this algorithm is stable for most applications, in the present case it has two main issues that need to be addressed: Maintaining the grid quality, and ensuring the surface alignment for the GGI. The algorithm tends to deform the volume grid mainly in surface vicinity, which leads to low

element quality in the boundary layer, especially for the rotor blades. This is countered here by introducing a protective volume to move all nodes close to the blades prescribed based on the FMBI results, to maintain full element quality in the boundary layer. During all simulations in this research, the grid quality was permanently monitored to ensure the suitability of the grid deformation algorithms.

On the other hand, considering the nacelle motion in the rotational and stationary frame, the GGI surfaces might detach between the rotor and stator grid domains. This must be prevented by applying a prescribed blending on the GGI grid from the FMBI surface deformation towards zero deformation at the circular GGI of the rotor.

#### 4.1.1.4 CFD Setup

Besides the numerical grid, CFX also relies on the turbulence model and the numerical schemes in the URANS formulation. Here, mostly the default settings of CFX are found to be suitable and therefore have been chosen. The turbulence is modelled with the SST-turbulence model with the curvature correction and Kato-Launder production limiters. For the advection terms, blending between 1<sup>st</sup> order upwind and 2<sup>nd</sup> order central scheme is used. The transient solution is calculated with a 1<sup>st</sup> order backward Euler scheme, due to the artificial added mass phenomenon, which will be discussed in the next section.

The boundary conditions follow the state-of-the-art guidelines for CFD models. The inlet has a prescribed velocity field, the outlet and sides are represented by entrainment-opening conditions, and the seabed and sea surface use free-slip walls to prevent artificial boundary layer issues. All turbine surfaces are no-slip walls. To account for the omitted flanges and hinges, which have a height of approx.  $100\text{mm}$  from the clean surface, an additional sand roughness height of  $h_s = 100\text{mm}$  on the nacelle is used.

#### 4.1.1.5 Artificial Added Mass Instability

The fluid reacts with its inertia and a corresponding force to any grid surface motion within a coupled hydroelastic simulation. However, the fluid solver is not able to distinguish between a physical motion and a numerical inaccuracy for the calculation of the reacting force. While the first is the added mass and a desired part of the solution, the latter may prove harmful during a simulation. The so-called artificial added mass effect describes this numerical effect of strong forces following disturbances in the computed motion. These strong forces may cause a counter-reacting motion in the structural solver, which leads to reversed artificial

added mass forces in opposite direction and can destabilize the simulation. This behavior is sketched in Fig. 4-3.

The artificial added mass is influenced by several physical and numerical parameters and may be prevented. As shown by [31], for systems with a low structure to fluid density ratio, the risk is increased. For explicit schemes in, e.g., pure structural cases, stability can be usually achieved by reducing the size of the time step. However, according to [55] this even increases the risk of artificial added mass and an implicit coupling scheme is the only numerical option to eliminate it. Another option is the consideration of the compressibility of the fluid, transforming the artificial added mass to an artificial acoustic wave, requiring very small time steps, which are not feasible for the present application of tidal turbines. Further, a numerical damping term on the coupling could be used, but would violate the conservation of energy.

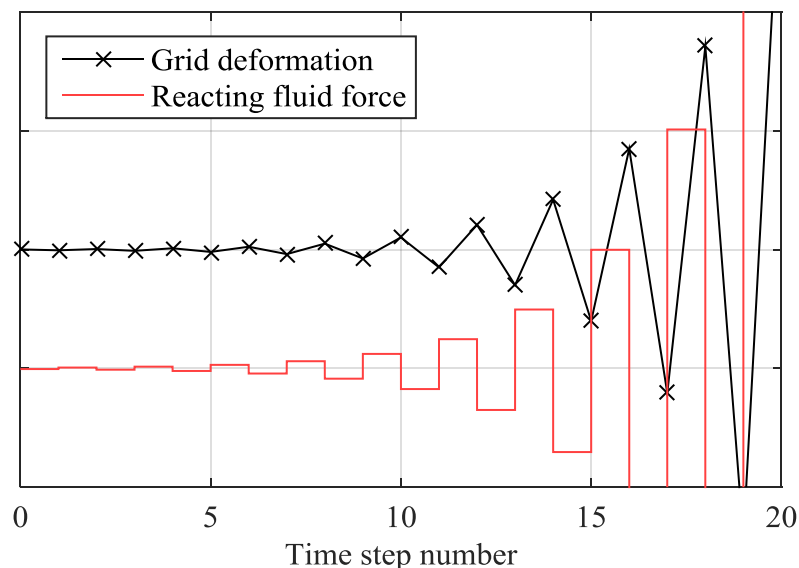


Fig. 4-3: Sketch of artificial added mass instability in an explicit coupled simulation

As discussed in Section 3.2.1.3, the method for the coupling of CFX and Simpack developed in this research fulfills the condition of an implicit coupling, as the artificial added mass issue has been anticipated during the development. However, applying it to an arbitrary setup is still not possible, as only the most recent time step is coupled implicitly. Therefore, in any case of the solver algorithm taking more than the recent time step into account for the calculation of the current time step, the system gets an explicit character. As also observed by [31], this explicit character of 2<sup>nd</sup> order time stepping schemes leads to the limitation that only a 1<sup>st</sup> order time stepping scheme can be used for the fluid solver. Solving this issue would require the implicit coupling scheme to be increased to 2<sup>nd</sup> order, and 2 time steps would have to be

iterated in the communications. This is not possible without access to the closed code structure of the used CFD and MBS tools. Therefore, all coupled simulations, and those compared to the coupled ones, are done with a 1<sup>st</sup> order backward Euler time stepping scheme.

Compared to the common 2<sup>nd</sup> order setup, the reduced numerical order will have a negative impact on the quality of the fluid solution, especially on the damping of, e.g., the tower shadow, as will be shown in Section 4.2.4. Nevertheless, the use of a 1<sup>st</sup> order scheme is unavoidable for the present cases to maintain the implicit character of the coupling and therefore has to be done. As has been discussed in the validation, Section 3.3.5.2, this condition of uncertainty in the results is not favorable, but acceptable for the present type of investigations.

#### 4.1.2 Structural Model

The structural model is setup in Simpack in version 9.5, containing rigid objects as well as flexible, modal reduced objects based on either FEM or beam theory. As it is not feasible to model every single detail of the turbine, the minor components such as screws, utility systems, cables, pre-assembled components, etc. are included in their respective primary component. The resulting list of primary components and their numerical description is shown in Table 4-1.

Table 4-1: List of MBS-model components

<b>Number</b>	<b>Component</b>	<b>Numerical description</b>	<b>Method</b>
1	Rotor blades	Modal reduced	Beam theory
2	Spinner	Rigid	Inertia tensor
3	Main shaft	Modal reduced	FEM
4	Generator	Rigid	Inertia tensor
5	Bearings	Force	Spring
6	Nacelle housing	Modal reduced	FEM
7	Tower & transition piece	Modal reduced	Beam theory
8	Foundation	Force	Distributed spring along monopile
9	Enclosed water	Rigid	Discrete distributed masses



While the blades and tower can be modelled with the beam theory due to their properties, this is not possible for the main shaft and the nacelle. The models for those components are based on the Abaqus FEM models of [43], which were modal reduced here using an eigenfrequency analysis. The resulting modes are then transferred as modal DoF to Simpack. The resultant setup is sketched in Fig. 4-4, however the full data of geometry and mass can not be shown here for confidentiality reasons.

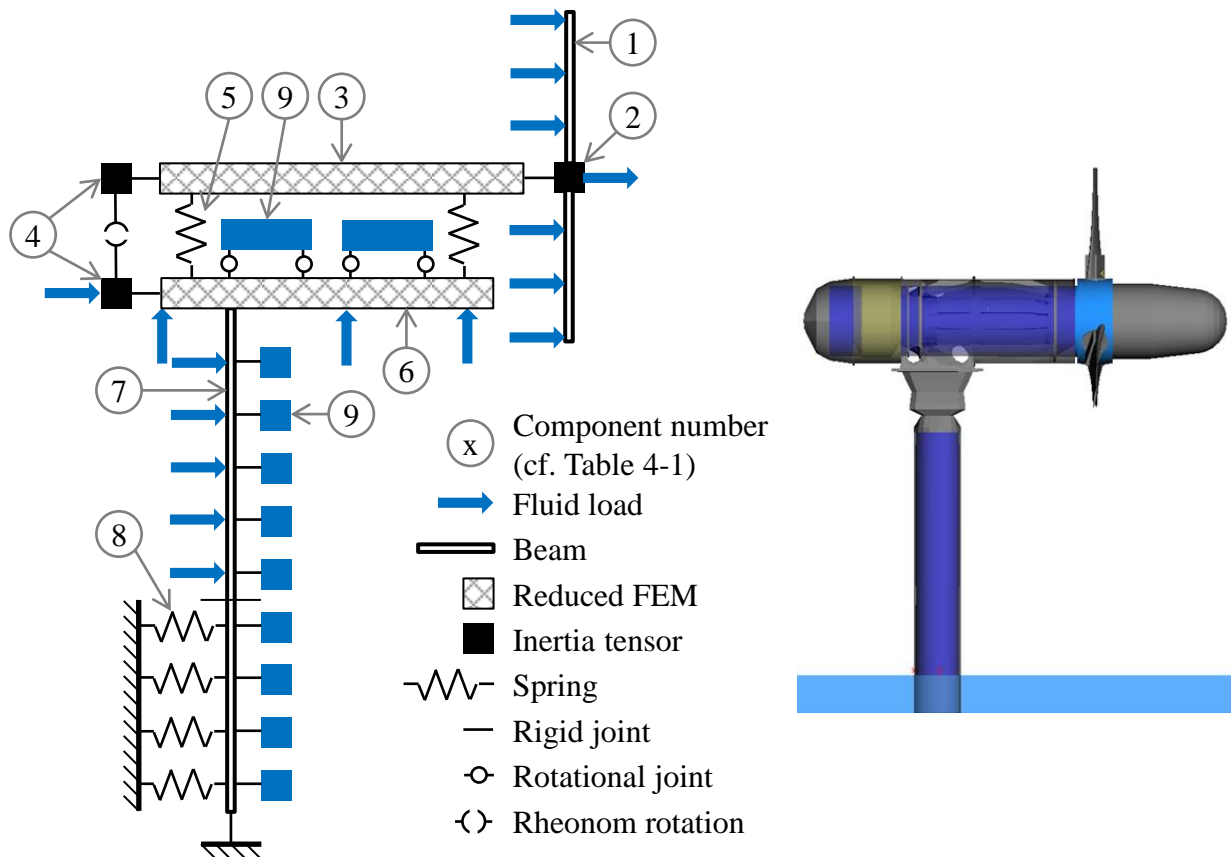


Fig. 4-4: Sketch of the MBS model topology (left) and visualization of the tidal turbine in Simpack (right)

Not all loads present in the real turbine are taken into account here. The steady loads of gravity and buoyancy are considered as an offset to the mean value. As the deformations are small and the MBS model in the present setup applies linear mechanics, the steady loads do not contribute to the dynamic hydroelastic response of the turbine. Load oscillations due to gravity and buoyancy occur only in the blade in-plane motion as additional  $1\Omega$  excitation. However, the in-plane eigenfrequency is more than one order of magnitude larger than the  $1\Omega$  excitation and thus the impact on the dynamics is negligible. As the present investigation

further concentrates on the hydrodynamic loads, the steady gravitational and buoyancy loads are not taken into account.

All transient structural and hydrodynamic loads are taken into account. The structural loads, including the ground support, joint forces and gyroscopic loads, are calculated solely in the MBS-model. The transient hydrodynamic loads of added mass, lift, drag, etc. are calculated completely by the CFD solver and transferred using the FMBI algorithm.

#### 4.1.3 FMBI Model

To setup the coupling of the fluid and structural model with the FMBI, the geometry needs to be discretized. This discretization splits the structure of the turbine into the splines and rigid objects that are used for the interpolation of deformations. As shown in Fig. 4-5, six interpolation splines based on 39 communication markers are used. Eight markers are distributed along each rotor blade, and seven along the tower, cf. Section 3.2.4.4. These numbers of markers are a trade-off between accuracy and effort on model setup and result in an adequately low discretization error with well below 0.25% relative error in calculated displacement, cf. Fig. 3-8.

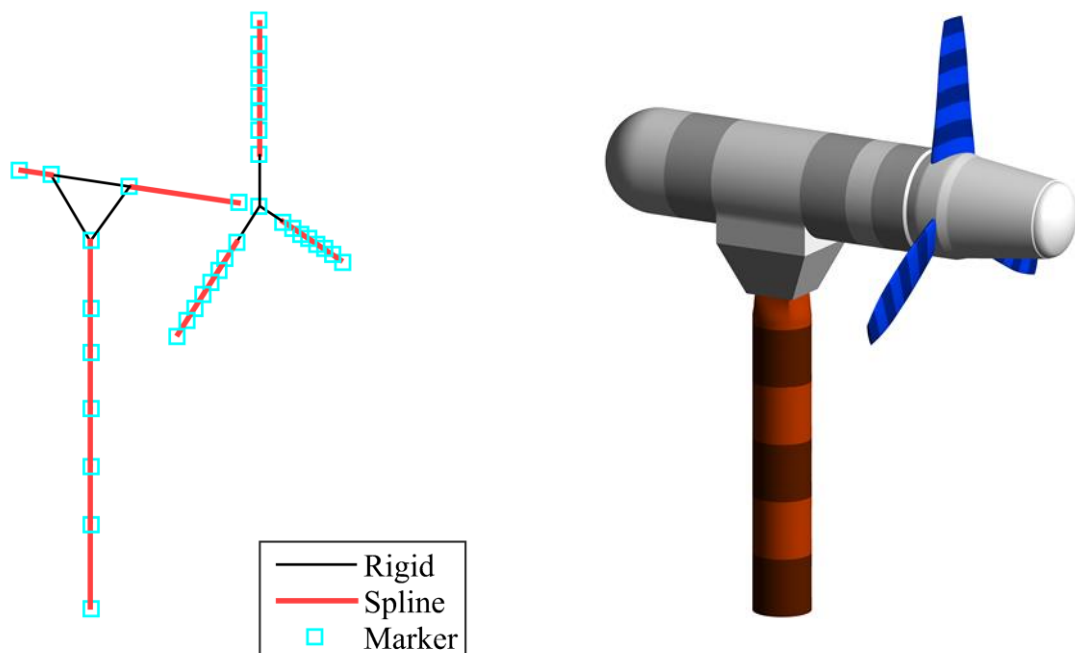


Fig. 4-5: Sketch of the interpolation system (left) and surface discretization of the CFD grid (right)

On the CFD grid, the turbine surface is split accordingly. Each communication marker is associated to a region of the turbine surface grid. The central marker location, cf. Fig. 3-8, is used for all but the first and last marker of each spline element, cf. Section 3.2.4.4. The markers are thus positioned in the middle of each grid region, where applicable.

Special attention was required for the spinner and the nacelle center section. On those locations, multiple interpolation splines intersect. Applying the methodology of section 3.2.4.4, Fig. 3-7, these are treated as rigid objects in the interpolation. They are still modeled as flexible bodies in the structural model, if applicable according to the simulated case.

Beside this interpolation setup, the number of iterations needs also to be defined. For the simulation of the Voith HyTide<sup>®</sup> turbine, a fixed number of five coupling iterations per time step resulted in a converged and stable simulation. However, the simulations do not span the same amount of time, as will be discussed further in Section 4.3.2, and for each simulation, the duration is adapted to match the necessary duration for the onset of the hydroelastic motion. Thus, the total number of coupling steps between the simulations varies.

## 4.2. Rotor-Foundation-Interaction

To analyze the hydrodynamics of the turbine system with rotor-foundation-interaction, only the rigid motion of the rotor with a constant rotational speed is taken into account. These transient simulations are performed with the fine grid with  $9.6 \cdot 10^6$  elements and grid motion between tower and rotor blades. This grid and motion is chosen in order to ensure a sufficiently high resolution for the identification of the resulting vortex structures and to analyze them with respect to their impact on the loads. In this section, also the numerical simplifications are evaluated, which are required for the hydroelastic simulations including the bi-directional FMBI coupling.

### 4.2.1 Simulated Cases

Based on the overspeed control algorithm of the Voith HyTide<sup>®</sup>-turbine, the points of operation can be grouped in two categories: below rated operation with  $\lambda_{TSR} = \lambda_{TSR\ opt}$ , and above rated operation with  $\lambda_{TSR} > \lambda_{TSR\ opt}$ . In the latter case, the tip speed ratio converges to the run-away condition with increasing current speed as shown in Fig. 4-6. To represent those two groups, cases are simulated with  $\lambda_{TSR} = \lambda_{TSR\ opt}$  at the design current speed of

$v_1 = 2.2m/s$  and with  $\lambda_{TSR} = 2 \cdot \lambda_{TSR\ opt} \approx \lambda_{TSR\ run-away}$ , [4], at the cut-out current speed of  $v_1 = 4m/s$ .

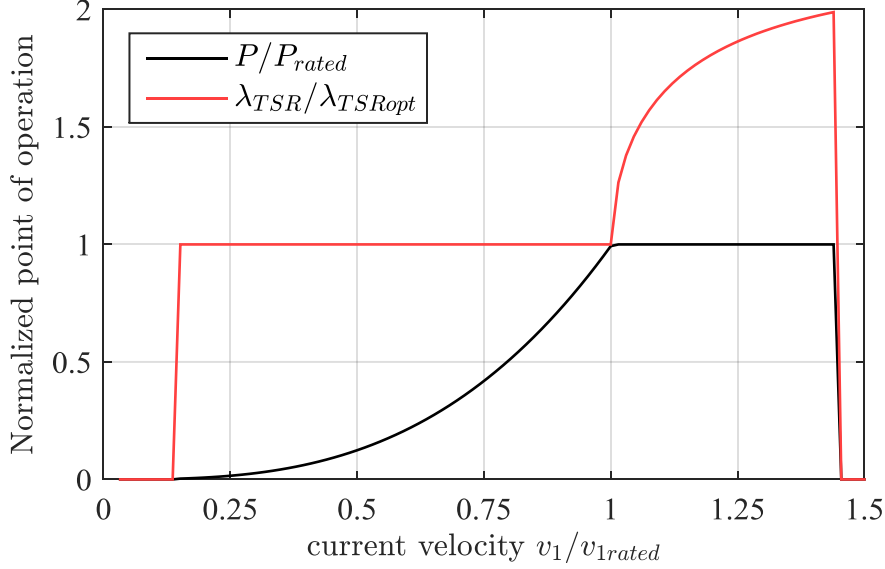


Fig. 4-6: Turbine power  $P$  and tip speed ratio  $\lambda_{TSR}$  over normalized current velocity  $v_1$

In order to account for the directional changes in the current velocity, luv and lee operation of the turbine, i.e. with the rotor up- respectively downstream of the tower, is considered. This leads to four points of operation for this investigation, as shown in Table 4-2.

The environmental conditions are assumed to be steady with an inflow velocity distribution according to the vertical current shear, (4-1), with  $\alpha_z = 0.19$ , which was derived from [58], and the current speed  $v_1$  at hub height  $h_{hub}$ . Taking turbulence, waves, etc. into account would be possible; however, the increase in required computational resources makes it unfeasible for the present investigation.

Table 4-2: Matrix of points of operation for the simulation of rotor-foundation-interaction

		Turbine orientation	
		luv	lee
Current velocity	Tip speed ratio $\lambda_{TSR}$		
	$v_1 = 2.2m/s$	$\lambda_{TSR\ opt}$	$\lambda_{TSR\ opt}$
	$v_1 = 4m/s$	$2 \cdot \lambda_{TSR\ opt}$	$2 \cdot \lambda_{TSR\ opt}$

$$v(z) = v_1 \cdot \left( \frac{z}{h_{hub}} \right)^{\alpha_z} \quad (4-1)$$

### 4.2.2 Qualitative Analysis of the Flow Field

The analysis of the results starts here with the below rated operation. For this case, the flow field around the turbine and the resulting wake structure can be split into the two regions of rotor and tower wake. Due to the energy extraction, the rotor causes a strong rotor wake. This wake is relatively homogenous, as the lift and load distribution on the rotor blade is homogenous by design, Fig. 4-7. The wake of the tower structure and the transition piece on the other hand changes significantly over time, and appears to be more chaotic and dependent on the luv or lee orientation of the turbine. This appearance of a chaotic wake and the direction dependency is a result of the vortex shedding at the tower, which has a velocity dependent shedding frequency, and thus depends on the current shear, cf. (4-1).

For luv and lee operation the rotor wake develops in nearly the same way. Both rotor wakes are bound on top position by a tip vortex. This vortex can be identified in Fig. 4-7 for luv operation at six locations and for lee operation at four locations by a locally increased velocity in the analysis plane. This difference in the dissipation of the tip vortex is a result of the difference in grid resolution and thus the difference in the numerical damping above the nacelle and in the farfield grid domain. However, the tip vortex in those regions does not interact with the structure of the turbine and thus will not cause additional loads. Therefore, the difference in damping can be neglected here.

Another difference between luv and lee operation can be observed for the tip vortex on the bottom position. For luv operation, a tip vortex is shed and convects with the flow. After one rotation of the rotor the tip vortex hits the foundation and interacts with the boundary layer on the tower. This results in a layer of increased flow velocity behind the tower, emphasizing the split of the turbine wake into the initially-introduced pattern of rotor wake and tower wake.

For lee operation the rotor operates in the foundation wake. Due to the low axial velocities, the angles of attack along the rotor blades are significantly reduced. Therefore, no tip vortex is shed on the bottom position, and also the depth of the rotor wake is reduced for vertical down position,  $\varphi = 180^\circ$ , of the rotor blade. This leads to an area of increased flow velocity in the rotor wake, which is mixed with the mean rotor wake within approximately one rotor diameter.

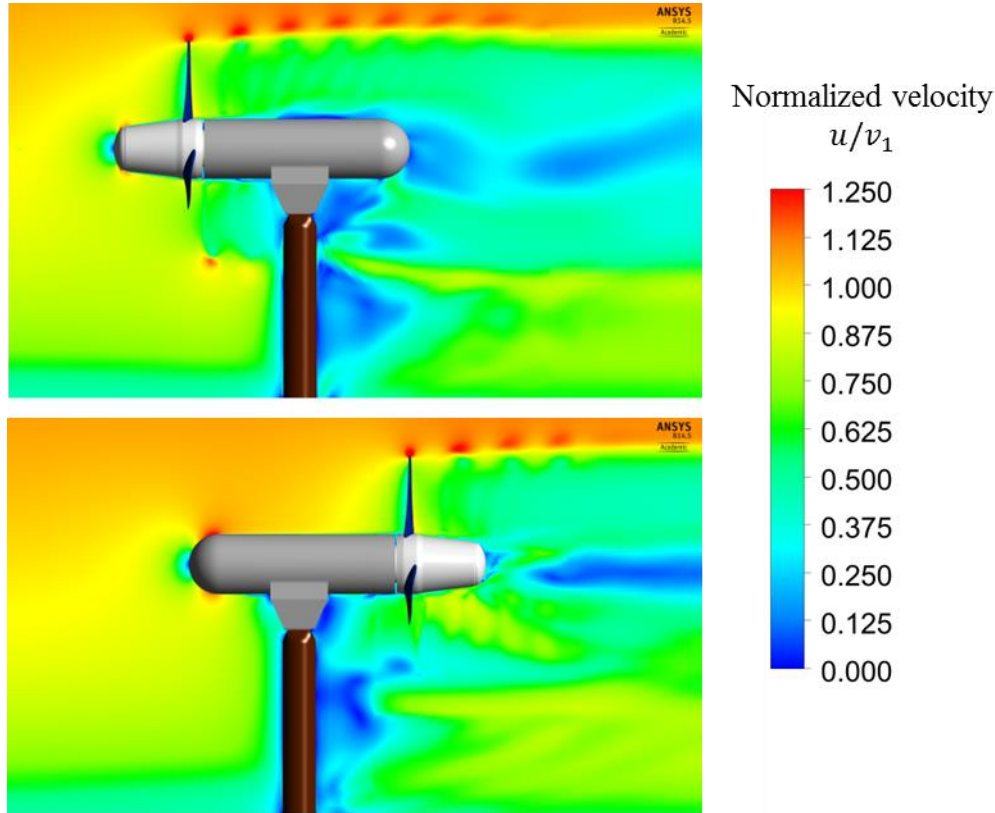


Fig. 4-7: Normalized current velocity on the turbine mid plane for luv (top) and lee (bottom) operation at  $v_1 = 2.2\text{m/s}$ ,  $\lambda_{TSR} = \lambda_{TSR\ opt}$

Similar effects as reported for the below rated operation are also present for the above rated operation as shown in Fig. 4-8. By direct comparison of below and above rated conditions, it can be seen that the rotor-foundation-interaction has a stronger impact on the flow field for above rated operation.

It can be noticed that there is a difference in the flow field for below rated luv operation compared to all other cases. The flow around the nacelle is homogenous with the expected boundary layer except for the below rated luv operation. For below rated luv operation the flow separates as shown in Fig. 4-9 at the transition piece between the foundation and the nacelle. Based on Newton's law 'actio est reactio', the wake of the rotor is rotating. This rotor swirl deforms the wake of the nacelle and transition piece around the nacelle. Due to the increased rotational speed at similar power output, the rotor torque  $Q_{Hydro} = P_{Hydro}/\Omega$  and the swirl are reduced for the above rated luv operation and thus this effect of deformed wake is significantly lower. This separation has only a minor impact on the rotor hydrodynamics, but is of interest for near wake investigations. It can also affect the nacelle side-side hydrodynamic damping to a minor extent.

A horseshoe vortex originating from the stagnation point of the transition piece can be identified in Fig. 4-10, by investigating the 3-dimensional flow around the nacelle. This horseshoe vortex moves along both sides of the nacelle. It vanishes in the below rated luv operation, due to the flow separation around the nacelle. For lee operation, the horseshoe vortex moves into the rotor plane and influences the rotor hydrodynamics by locally changing the angle of attack.

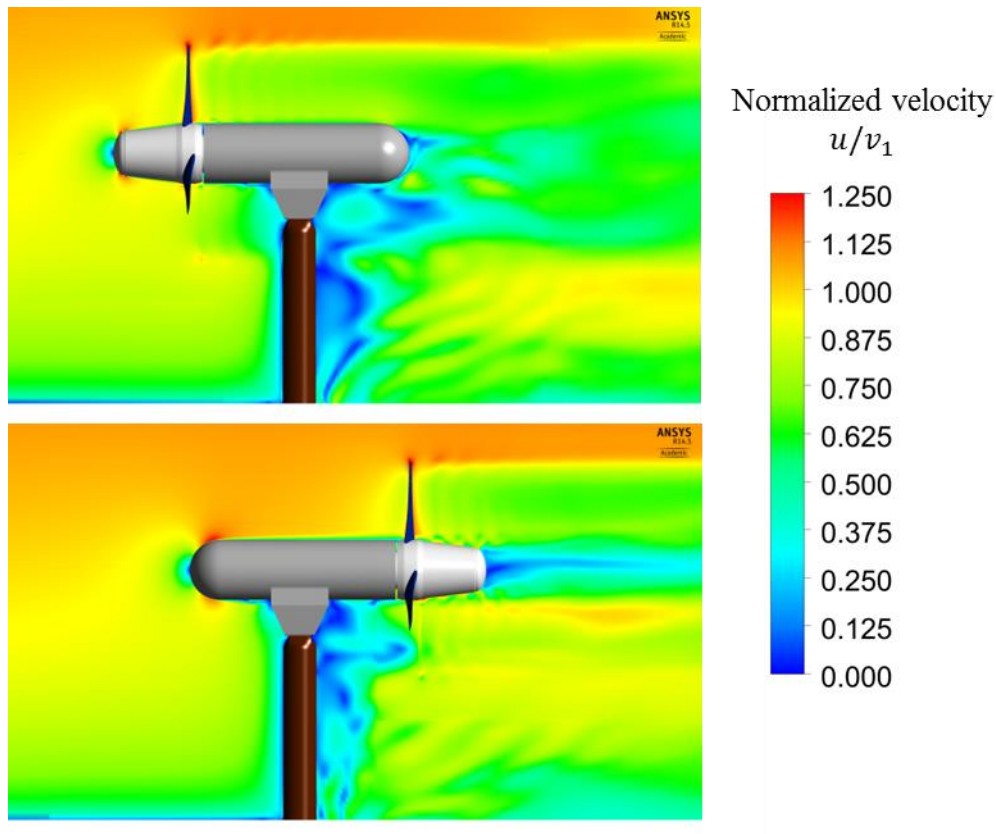


Fig. 4-8: Normalized current velocity on turbine mid plane for luv (top) and lee (bottom) operation at  $v_1 = 4m/s$ ,  $\lambda_{TSR} = 2 \cdot \lambda_{TSR\ opt}$

The last effect discussed here is the 3-dimensional wake of the foundation for lee operation, Fig. 4-11. Due to the same dimensions in diameter of the transition piece and the nacelle, the flow moves tangential to the circular nacelle surface from the sides of the nacelle into the wake structure of the transition piece. This forms a co-rotating and counter-rotating area in the rotor inflow, which increases respectively decreases the angle of attack at the rotor blades.

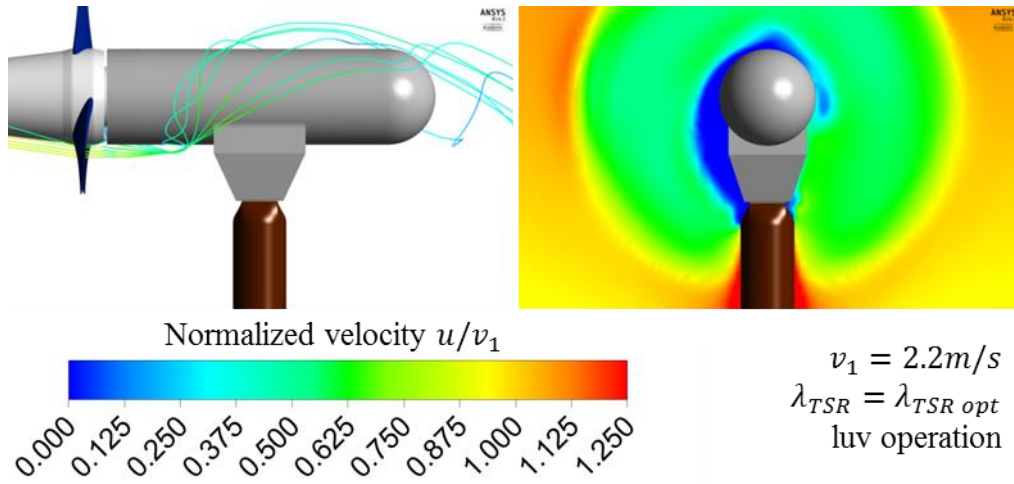


Fig. 4-9: Swirl deflected transition piece wake in side (left) and rear view (right)

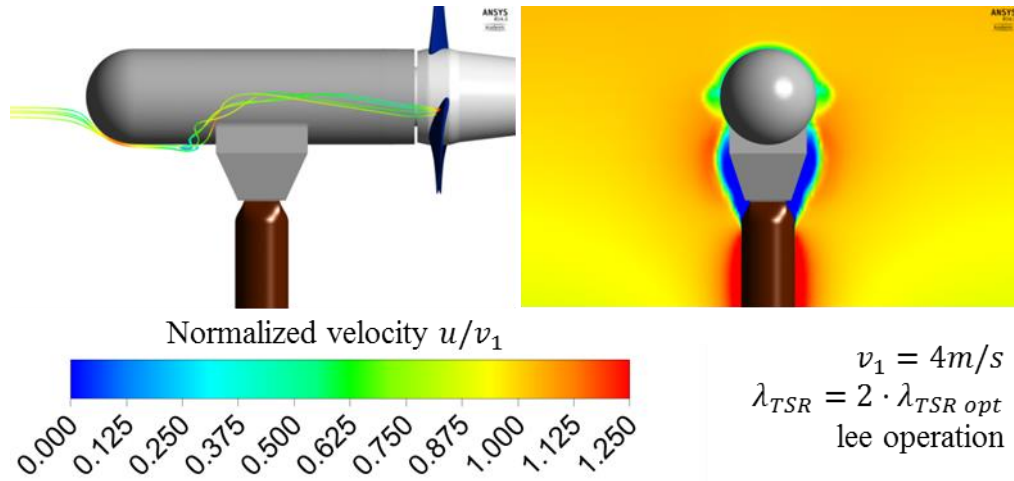


Fig. 4-10: Horseshoe vortex origin at tower-nacelle connection in side (left) and rear view (right)

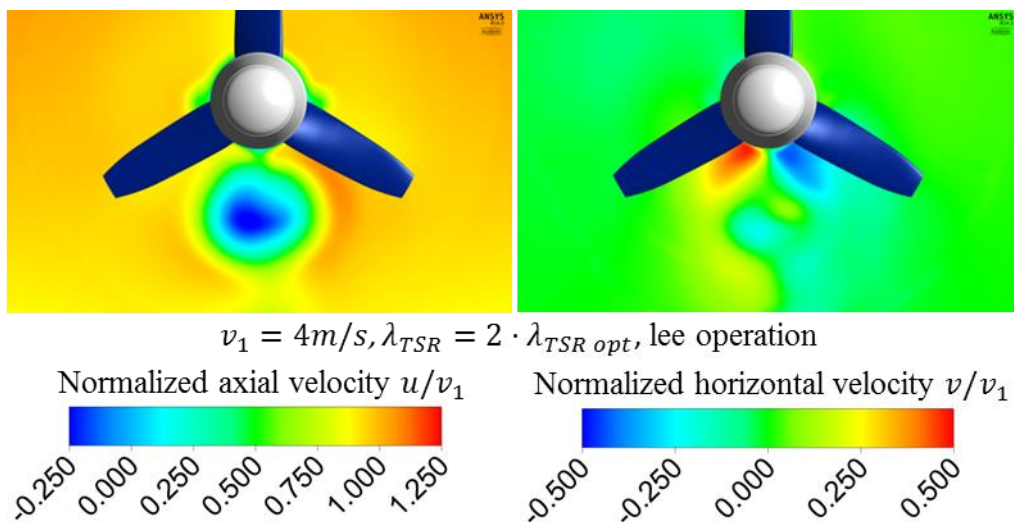


Fig. 4-11: Rotor inflow velocity field 5m after tower center in front view



### 4.2.3 Quantitative Analysis of the Hydrodynamic Loads

To evaluate the impacts of the vortex structures, described in the previous section, the blade thrust coefficient  $c_{th\ blade}$  is shown in Fig. 4-12 for lee operation. The results for the power coefficient are equivalent to the findings for the thrust coefficient. The luv operation results are not further detailed here, as they yield only a about 25% amplitude amplification of the close to sinusoidal time series of the blade thrust due to current shear, but no higher order excitations as shown in publication [A 15]. The luv rotor-foundation-interaction therefore needs to be taken into account for fatigue analysis, but has a lower impact on the turbine loads compared to the lee operation. Therefore, the lee operation can be considered as more severe with respect to the hydroelastic motions and loads.

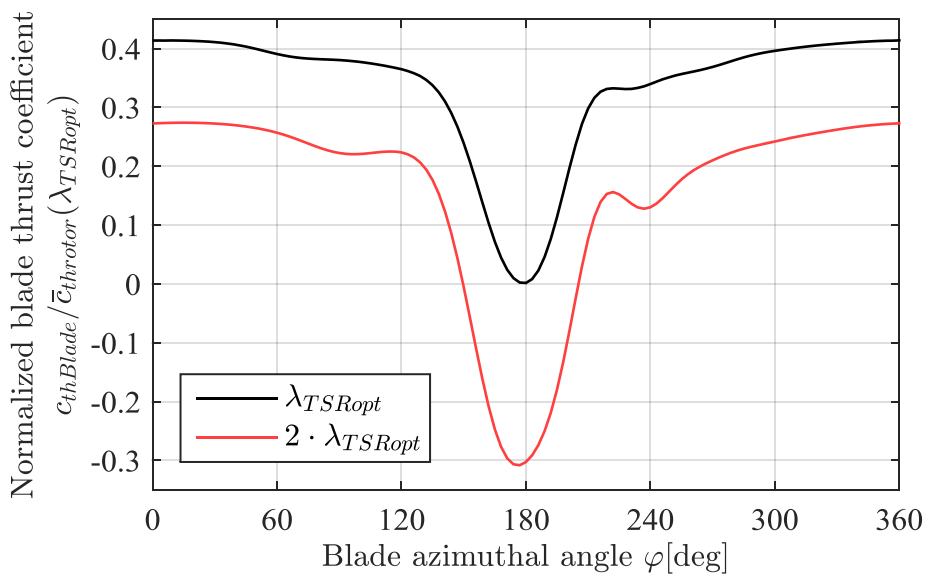


Fig. 4-12: Blade thrust coefficient  $c_{th\ blade}$  during revolution in lee operation

In lee operation, the rotor is significantly influenced by the local vortex structures. The strongest effect results from the wake of the foundation itself. As described in the previous section, the rotor wake deficit is reduced for  $\varphi = 180^\circ$ . This is confirmed by the quantitative results in Fig. 4-12, showing that the rotor blade's thrust coefficient is reduced, or even becomes negative for  $\lambda_{TSR} = 2 \cdot \lambda_{TSR\ opt}$  in the tower wake.

Further, the influence of the horseshoe vortices can be identified as a reduction of the thrust, and also of the power coefficient, over a short range at the position of the vortices. The position of the reduction in values at  $\varphi \approx 90^\circ$  and  $240^\circ$  does not fully correlate with the positions of the vortices. This phase shift occurs due to the finite blade chord length at hub,

and therefore the difference in the blade position  $\varphi$  and the position of the leading edge  $\varphi_{lead}$ , which interacts with the vortices. Also a slight difference in position of the load fluctuation depending on the point of operation can be observed, due to the changes in the intensity of the rotor wake and the generated rotor swirl.

Similarly, the co- and counter-rotating inflow to the rotor influences the loads as it decreases or increases respectively the apparent tangential velocity  $v_{tan}$ , cf. Fig. 2-4. Based on the subsequent changes in angle of attack  $\alpha_{AoA}$ , the thrust and power coefficient are increased for  $\varphi < 180^\circ$  and decreased for  $\varphi > 180^\circ$ , visible in the asymmetry in Fig. 4-12, resulting in an additional side-side bending moment on the nacelle.

The tower shadow in lee operation induces load oscillations in all six load components to the hub. The most significant are thereby the axial thrust load and the nodding moment, which are dominated by the  $3\Omega$  excitation frequency and include strong higher order components. It can be therefore concluded that the vortex structures have a relevant effect on the loads on the turbine system and will cause hydroelastic responses.

#### 4.2.4 Impact of Numerical Simplifications

As has been discussed in Section 4.1.1, it is not suitable to perform the coupled FMBI simulations with the maximum possible resolution on the CFD side. Fig. 4-13 shows the comparison of the blade thrust coefficient during one revolution at  $\lambda_{TSR} = 2 \cdot \lambda_{TSR\ opt}$ . It can be seen that the numerical (1<sup>st</sup> or 2<sup>nd</sup> order time stepping), spatial ( $3.5 \cdot 10^6$  or  $9.6 \cdot 10^6$  elements), and temporal (120 or 180 time steps per revolution) resolutions have a significant impact on the results. Especially, the higher frequency effects of the horseshoe vortex along the nacelle change, when using the coarser setup. The reason for this observation is the change in numerical damping, which, e.g., increases the tower wake width and reduces its depth due to the increased numeric mixture.

While the impact of the spatial and temporal resolution is acceptably small, the numerical resolution reduces the load amplitude significantly. However, as discussed in Section 4.1.1.5, the numerical resolution can not be refined. Using a 1<sup>st</sup> order temporal scheme is inevitable for a stable solution, and therefore its impact has to be accepted.

For the spatial and temporal resolution, the finer setup requires significantly increased computational resources. While the increase in temporal resolution requires 50% more resources, the time for the simulation is about three times higher with the finer grid. Those

changes in resources are therefore an inconvenience, which has to be evaluated. In the present research the decision to use the finer temporal, but the coarser spatial resolution is reasoned by the comparatively small impact, considering the change due to the time stepping scheme. Yet, the finer temporal resolution yields the advantage of higher frequency resolution for the hydroelastic simulations. For the  $6\Omega$  excitation with 20 time steps per oscillation and the  $9\Omega$  with only 13 time steps per oscillation, the resolution of  $\Delta\varphi = 3^\circ$  (120 time steps per revolution) is considered too coarse according to usual setup requirements.

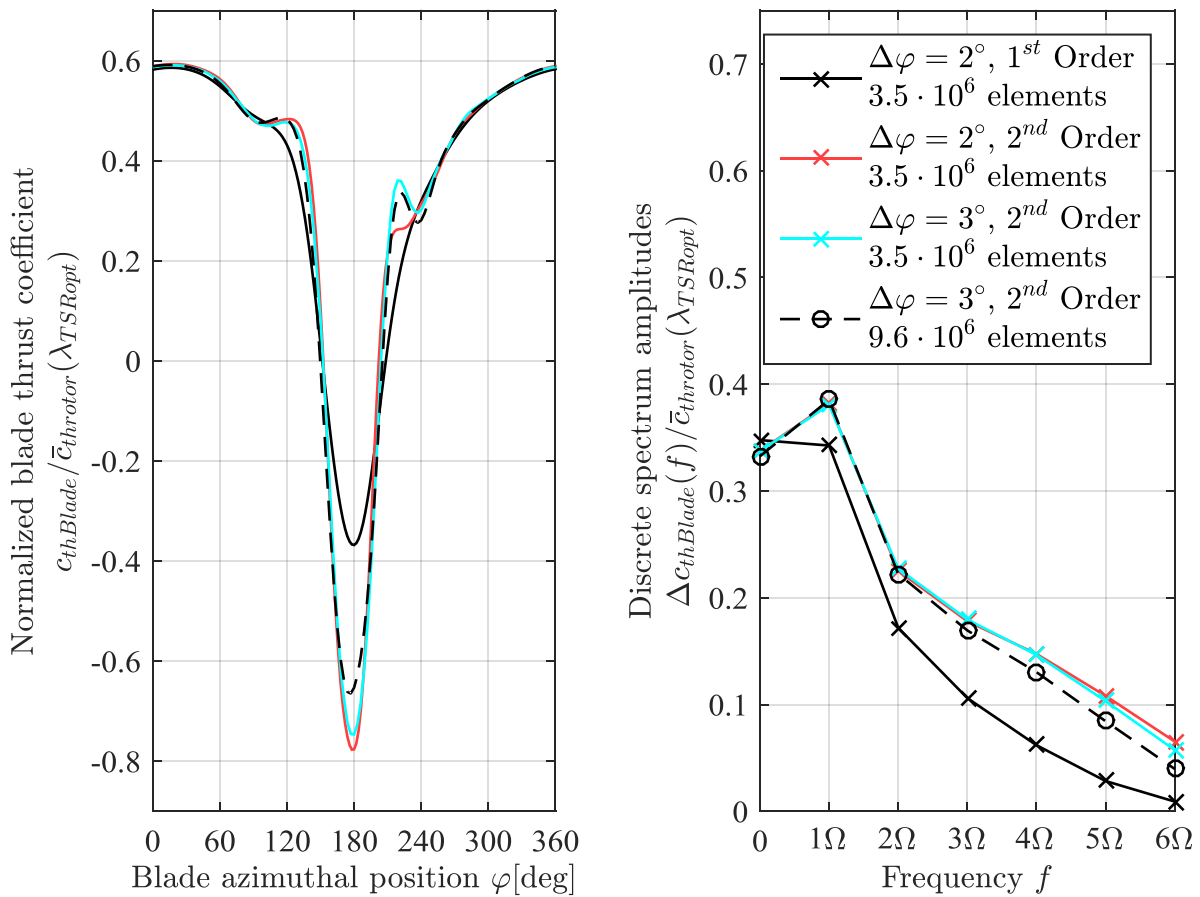


Fig. 4-13: Impact of numerical, spatial and temporal resolution on the blade thrust coefficient  $c_{th\ blade}$  (left) and on corresponding amplitude  $\Delta c_{th\ blade}$  spectrum (right)

Overall, it can be concluded that the numerical and the model setup have an impact on the results in the shown cases. Thus, the results are not fully setup-independent as usually intended. However, keeping the discussion of Section 3.3.5 in mind, the absolute results are not stringently required as long as only linear elastic cases are compared with the same excitation amplitude. This is the case for the analysis in this research and therefore the issue

of the setup-dependency is accepted for the present cases as trade-off with the numerical requirements and available resources.

### 4.3. Impact of Flexibility on Loads

Based on the rigid body hydrodynamics shown in Section 4.2, the point of operation at high current speed,  $v_1 = 4m/s$ , and run-away-condition,  $\lambda_{TSR} = 2 \cdot \lambda_{TSR\ opt}$ , in tower shadow is considered the most severe case with the highest loads. This is also in agreement with the stochastic load analysis as described in Section 5.2.3 and in [85]. Therefore, this point of operation is chosen and analyzed further in the following section. Within this deterministic operational state, a variety of combinations of components with a flexible or rigid structure are simulated. The purpose of this process is to identify, which components' flexibility has the largest impact on the hydrodynamic loads compared to the rigid case.

#### 4.3.1 Flexible Turbine Motion

In the first step of the operational analysis, the turbine is simulated fully flexible with all components of the turbine flexible. This results in the dynamic motions of the system sketched in Fig. 4-14.

The blade tips are moving in an approximately elliptical circle. On the upper side of the blade positions, the deflection is close to constant. On the lower side, the rotor blade deflection is reduced, due to the decreased current velocity based on the shear. When entering the tower wake, the blade tip swings back towards the tower and even reaches a negative deflection. Still, the overall deflection is with ca.  $2.3cm$ , i.e. 0.35% of the rotor radius, at the topmost position of the blade tip small compared to the turbine size. Based on the load analysis in Section 4.2, the dominant loads are the oscillating thrust and nodding moment, due to the tower wake. Therefore, the expected dominant motion of the system is a fore-aft and a nodding motion. All other motions are expected to be much smaller, as the exciting loads are smaller. However, this is not observed in the present simulations. Instead, the tower deflection is almost constant over time after the onset of motion, with the nacelle in a bow position and a strong nodding motion. This can be seen on the hub in Fig. 4-14, moving in an s-shaped curve in the side view. Further, the nacelle is rotating on the tower torsional mode. Furthermore, the nacelle is in a non-periodic side-side-motion  $\Delta y$  with about double the amplitude of the fore-aft-motion  $\Delta x$  as shown by Fig. 4-15.

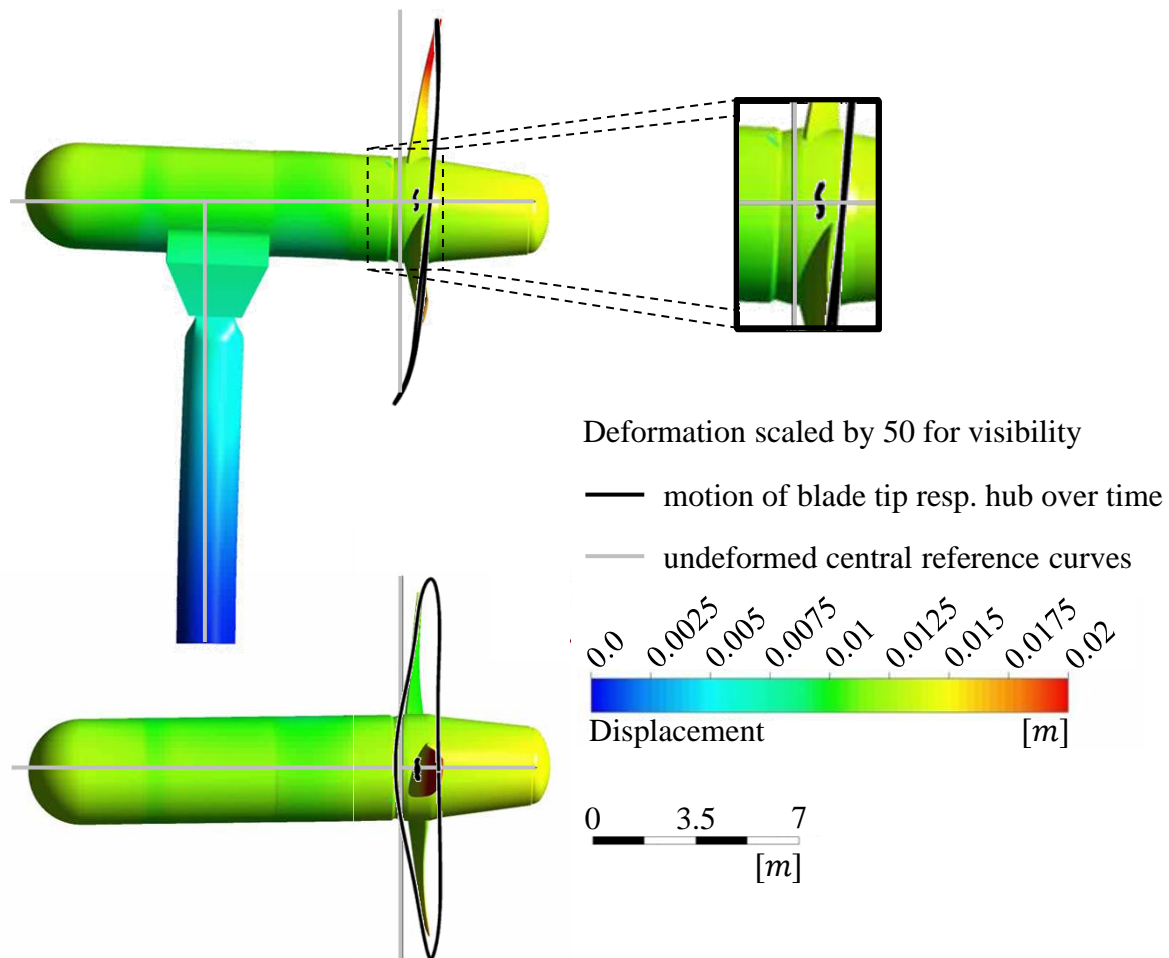
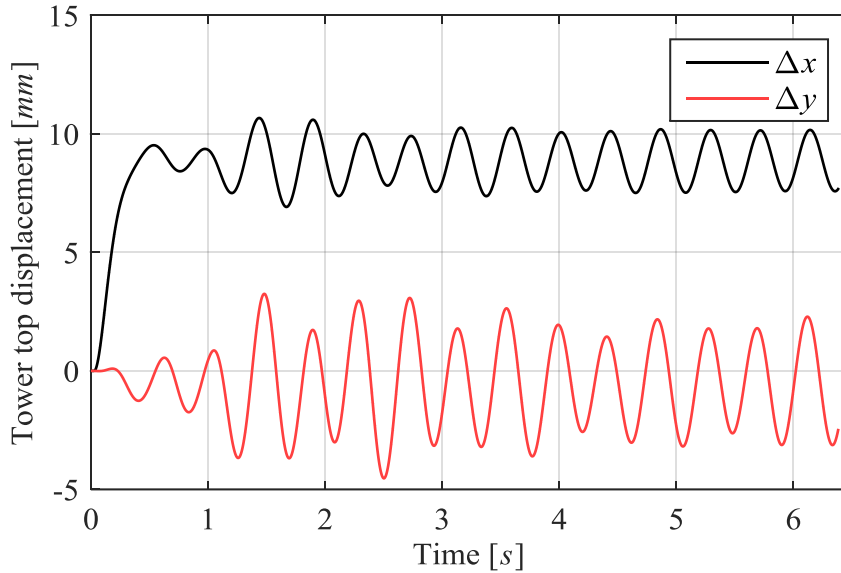


Fig. 4-14: Fully flexible turbine in motion colored by displacement

To explain those motions, they need to be divided into 2 groups. Starting with the nacelle nodding and torsional motion, these are clearly a result of the  $3\Omega$  excitation, due to the tower wake. This  $3\Omega$  excitation is with  $f_{3\Omega} = 2.35\text{Hz}$  about 37% higher than the 1<sup>st</sup> tower eigenfrequency, cf. Fig. 4-25. Subsequently the nacelle fore-aft-motion is not able to follow the loading and the amplitude of motion is reduced. The 2<sup>nd</sup> tower bending eigenfrequency, as well as the torsional eigenfrequency, on the other hand are close to or higher than the  $3\Omega$ . In combination with the tower shadow causing not only an oscillating rotor thrust, but also a time dependent side loading in the rotor plane and a periodic nodding moment, the present motion occurs.

The source for the non-periodic nacelle side-side motion  $\Delta y$ , Fig. 4-15, is not a result of the rotor loading alone. A frequency domain analysis of  $\Delta y$  reveals two dominant frequencies at  $f \approx 2.37\text{Hz}$  and  $f \approx 1.51\text{Hz}$ . The first frequency is within numerical accuracy the  $3\Omega$  excitation, the latter is the vortex shedding frequency at the tower. The turbine is therefore in

a vortex induced vibration state, combined with the  $3\Omega$  oscillation, resulting in the observed non-periodic side-side motion.



Only tower is modeled flexible here; the fully flexible case is equivalent but not started from zero deflection, cf. 4.3.2

Fig. 4-15: Tower top motion over time, case V (Table 4-3)

### 4.3.2 Simulated Configurations

As discussed initially in Section 1.2, one of the main objectives of this research is to identify the components, which have an impact on the hydroelastic behaviour of the turbine. Therefore the structural model is varied and a total of 10 different setups have been simulated. These are listed in Table 4-3 with the number of eigenmodes taken into account for each component. These numbers of modes represent the dominant modes of each component. The higher modes, which have eigenfrequencies notably higher than the relevant excitations, cf. Fig. 4-13 (right), are neglected.

The single cases were not simulated for the same time period. The time required for the onset of the oscillation depends on the actual setup and took, e.g., about 3.5 revolutions for case V shown in Fig. 4-15. Thus the simulated number of revolutions is adapted for each simulation. The main purpose of this variable simulation length is to reduce the required computational resources. For instance, case III takes only a single revolution to converge, starting from the rigid solution, and the fully flexible case takes three additional revolutions starting from the converged result of case VII. Thus, the fully flexible case is simulated for five revolutions taking about 160h on 20 Cores, 2.2GHz.

Table 4-3: Number of Eigenmodes in each simulated combination

Case	Main shaft	Nacelle housing	Rotor blade	Tower & Ground*	Transition piece
Rigid					
I	3				
II	3	4			
III			3		
IV	3	4	3		
V				6	
VI				5	
VII				5	3
VIII			3**		
Fully flexible	3	4	3	5	3

\*) 5: tower torsional rigid at seabed; 6: ground torsional soft

\*\*\*) blade out-of-plane eigenfrequency in air reduced by 50%

The different simulation periods do not change the results for the periodic motion. However, bringing the two frequencies observed in the previous section to mind, the phase angle between the rotor revolution and the vortex shedding on the tower is time dependent. Consequently, the relative phase position of the two load oscillations changes with each case, as the described method of using other cases as initial conditions also appends the absolute time of the simulations. Therefore, the forces from the vortex induced motion differ on each simulation and the loads on the turbine may differ slightly on the direct comparison, due to this effect. Also, the results are no longer exactly  $3\Omega$  periodic as initially expected, but vary slightly between each blade passage, as can be seen, e.g., in Fig. 4-16, by comparing the values at  $240^\circ$  and  $360^\circ$  blade position. Nevertheless, this disadvantage is considered minor and the advantage of the reduced computational effort is much greater.

### 4.3.3 Variation of Drivetrain Flexibility

The first set of comparisons of flexibility variations is carried out for the drivetrain (main shaft and rotor blade) and the nacelle components (case I...IV). Fig. 4-16 compares the axial thrust force on the hub  $F_{x\text{Hub}}$  during one third of a revolution, which is equivalent to the

passage of one rotor blade at the tower. There is close to none impact on this load due to the drivetrain flexibility. As the nacelle (case II) and shaft (case I) are both very stiff in this direction their impact was expected to be small. Based on the lower stiffness of the rotor blade's out-of-plane bending mode (case III), a higher impact on  $F_{x\ Hub}$  could be expected. However, the blade out-of-plane eigenfrequency is still much larger than the excitation frequency  $f_{OoP\ Blade} \gg 1\Omega$  and subsequently the impact can be neglected. This result is specific for the here investigated geometry and might change for other blade designs as will be discussed in Section 4.3.4.

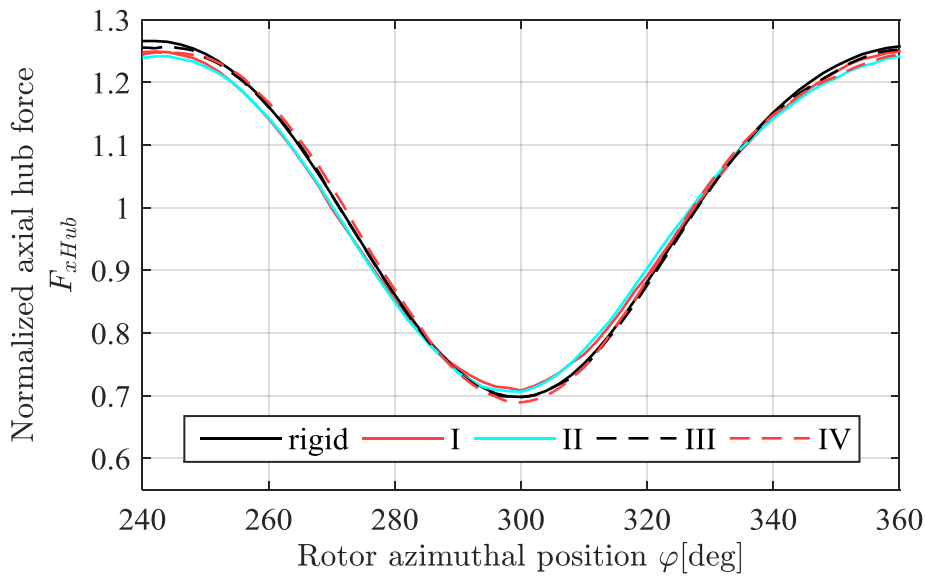


Fig. 4-16: Axial hub force  $F_{x\ Hub}$  with varying drivetrain flexibility normalized with mean value  $\bar{F}_{x\ Hub}|_{rigid}$

For the hub torque  $Q_{x\ Hub}$  the impact of the drivetrain flexibility is larger, Fig. 4-17. Depending on the combinations of flexibility the rotor is oscillating in rotating modes. In case III the blades are flexible and oscillating in the in-plane eigenfrequency. As the shaft and hub are rigid and rotating at a constant speed each blade mode is uncoupled from the other blades. Thus, the impulse due to the tower shadow affects only a single blade at a time causing a strong response. This oscillation also has a low damping ratio and is subsequently persistent over a large number of periods.

In case I/II the rotor is rigid and the shaft is flexible with the corresponding torsional eigenfrequency. Subsequently, the changing impulse respectively momentum introduced by the tower shadow to the blade in-plane motion is distributed amongst the full rotor inertia and the oscillation is smaller. Also in case IV, which is the combination of II and III, the shaft is



no more rigid and the blade modes are not anymore coupled. In the same way as for case II, the momentum to the blade is spread amongst the three rotor blades and the in-plane oscillation is reduced.

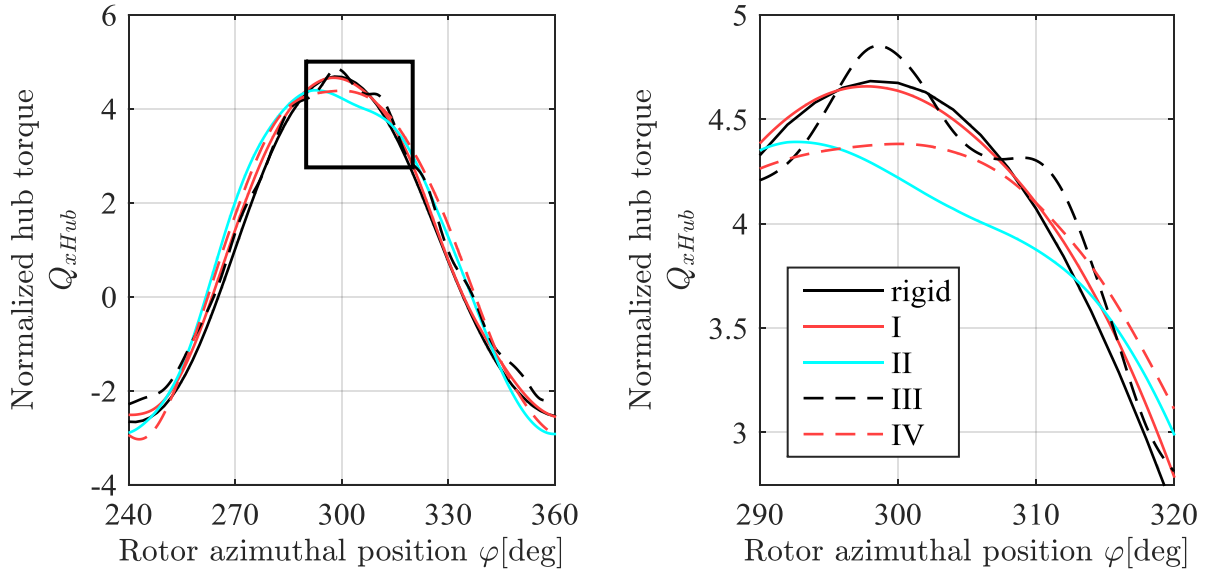


Fig. 4-17: Hub torque  $Q_{xHub}$  with varying drivetrain flexibility normalized with mean value  $\bar{Q}_{xHub}|_{rigid}$

Fig. 4-18 shows the impact of the drivetrain flexibility on the tower bottom bending moment  $M_{yTowerBottom}$ . As can be seen, the flexibility of the rotor blade and the main shaft have only a minor impact on  $M_{yTowerBottom}$ . The nacelle flexibility on the other hand has a significant impact on the tower bottom bending moment. While the impact of the rotor thrust, Fig. 4-16, on  $M_{yTowerBottom}$  remains the same due to the high axial stiffness of the nacelle, the nodding moment of the rotor is no longer transmitted in its full extent through the nacelle into the tower top as the nacelle is less stiff in this direction and the mass inertia introduces counteracting forces.

As the  $6\Omega$  frequency is close to the nacelle nodding eigenfrequency, there is an additional eigenmotion with this frequency. Subsequently the amplitude of  $M_{yTowerBottom}$  is reduced but it has a strong  $6\Omega$  component, visible in the two additional extremal points in Fig. 4-18, case II/IV.

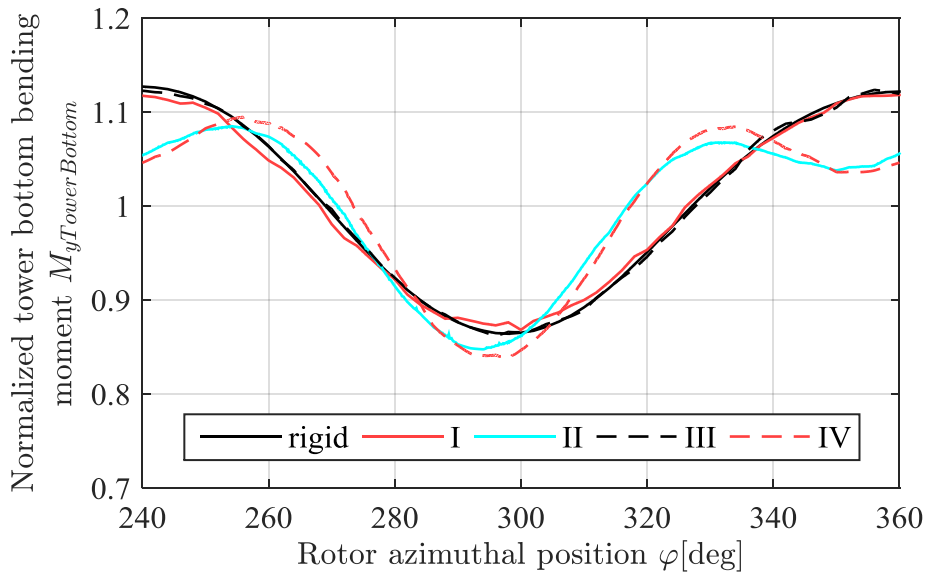


Fig. 4-18: Tower bottom bending moment  $M_{y TowerBottom}$  with varying drivetrain flexibility normalized with mean value  $\bar{M}_{y TowerBottom}|_{rigid}$

#### 4.3.4 Variation of Blade Flexibility

Most research on hydroelasticity on tidal current turbines focuses on the rotor blade's out-of-plane bending mode, e.g. [42], [62] and [79], as done also in the wind energy state-of-the-art. However, in the present simulations this flexibility was shown in the previous section to be of negligible impact. This disagreement can be traced back to the specific design of the Voith HyTide<sup>®</sup>1000-13 rotor blades. Fig. 4-19 shows the comparison to a generic rotor blade (case VIII) with the blade stiffness reduced by factor of four. The blade surface geometry is not changed for simplicity.

Maintaining the blade mass, the stiffness reduction reduces the eigenfrequency in air by 50%. Despite the eigenfrequency is still about six times larger than the dominant  $1\Omega$  excitation, the impact of the rotor blade flexibility is significantly increased. The hub load  $F_{x Hub}$  and the tower bottom bending moment  $M_{y TowerBottom}$ , show a strong response to the oscillations of the rotor blade and its mass.

The rotor blade therefore might have an impact and needs to be checked, whether its specific design has an impact on the loads or not. For the present case of the Voith HyTide<sup>®</sup>1000-13 turbine the impact of the rotor blade flexibility can be neglected.

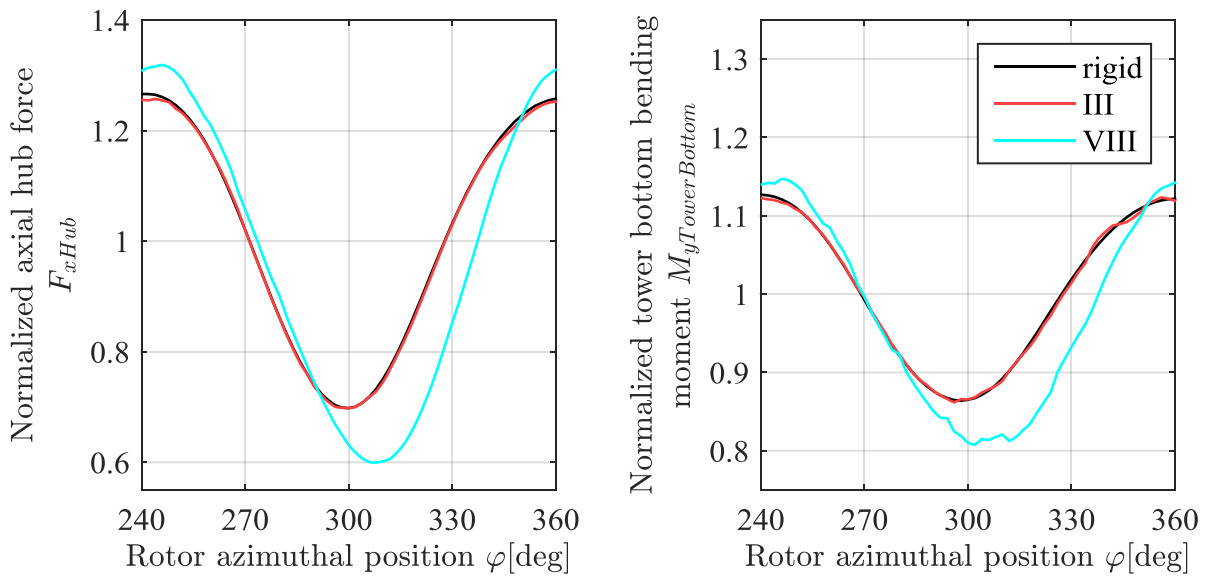


Fig. 4-19: Axial hub Force  $F_{xHub}$  (left) and tower bottom bending moment  $M_{yTowerBottom}$  with varying blade structural flexibility normalized with mean value  $\bar{F}_{xHub}|_{rigid}$  and  $\bar{M}_{yTowerBottom}|_{rigid}$  respectively

#### 4.3.5 Variation of Fixed-Structure Flexibility

The 2<sup>nd</sup> big group of flexibility variations considers the tower and ground flexibility. Similar to the investigation of the drivetrain and nacelle flexibilities, the analysis starts with the driving torque at the hub,  $Q_{xHub}$ , Fig. 4-20. Similar to the observations in the previous section, only a small impact of the flexibilities on this load is noticeable. Despite this impact is larger than anything observed for the drivetrain flexibility variations, cf. Fig. 4-17, it is mainly a phase shift. This phase shift occurs due to the nodding motion of the turbine, and the subsequent fore-aft motion of the outer blade sections, influencing the hydrodynamic torque.

For the axial hub load  $F_{xHub}$ , the impact is larger, Fig. 4-21. Two effects combine here: The change in the hydrodynamic load due to the motion, as discussed for  $Q_{xHub}$ , and the inertia loads due to the nacelle acceleration. The motion amplitude is with  $\Delta x \approx 1.5mm$  small, as shown in Fig. 4-15. However, due to the high frequency of the oscillation, the nacelle fore-aft acceleration amplitude is  $\Delta \ddot{x} \approx 0.55m/s^2$ . Combined with the mass of the rotor blades and the hub system,  $m_{rotor}$ , the resultant inertia force,  $F = m_{rotor} \cdot \Delta \ddot{x}$ , is at about 5% of the steady load. This is equal to the amplitude reduction of  $F_{xHub}$  by 30% seen in Fig. 4-21.

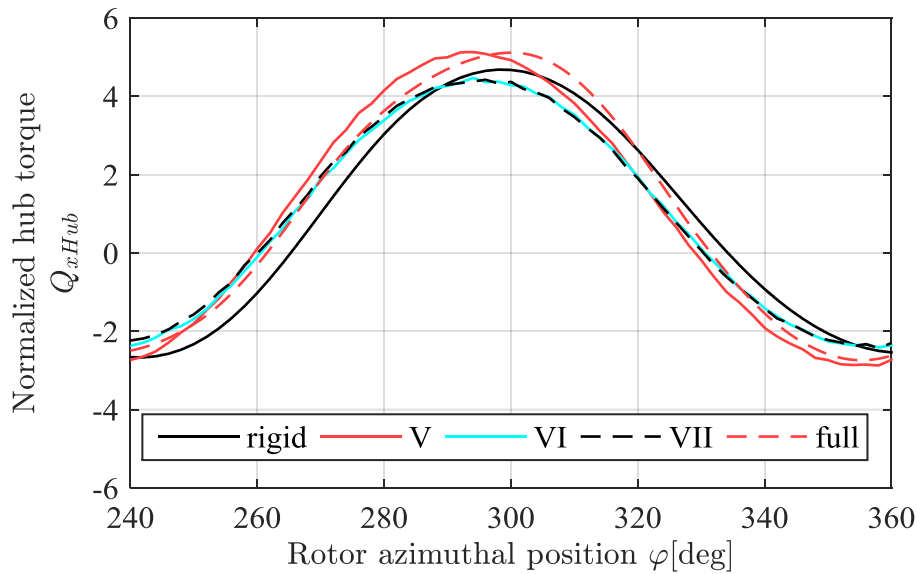


Fig. 4-20: Hub torque  $Q_{xHub}$  with varying fixed-structure flexibility normalized with mean value  $\bar{Q}_{xHub}|_{rigid}$

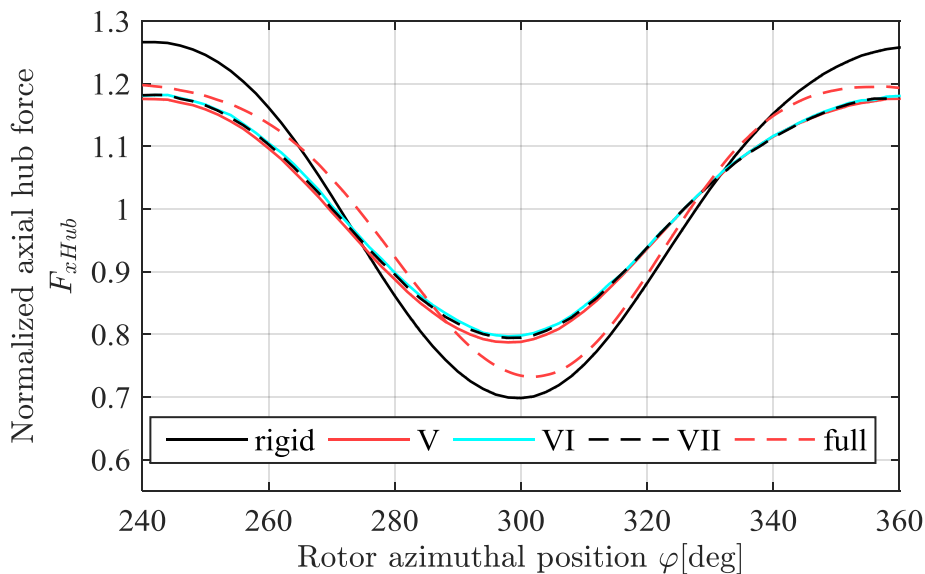


Fig. 4-21: Axial hub force  $F_{xHub}$  with varying fixed-structure flexibility normalized with mean value  $\bar{F}_{xHub}|_{rigid}$

This finding is also confirmed by the axial tower top load  $F_{xTowerTop}$ , Fig. 4-22. The same results as for the hub loading can be found, but the impact of the inertia is significantly larger, as the accelerated mass is higher. The amplitude of the axial tower top load is reduced by about 70% due to the heavy mass of the nacelle with the included water.

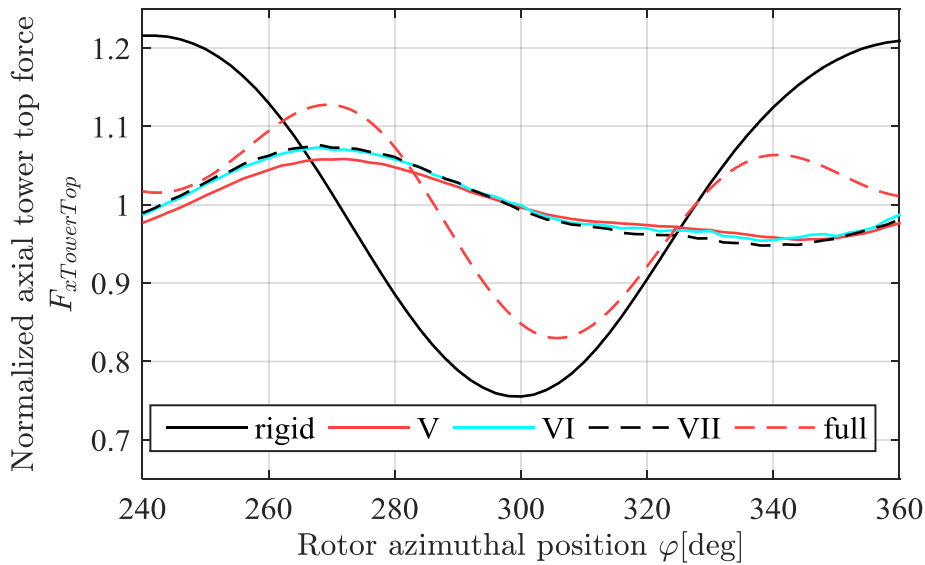


Fig. 4-22: Axial tower top load  $F_{x\ TowerTop}$  with varying fixed-structure flexibility normalized with mean value  $\bar{F}_{x\ TowerTop}|_{rigid}$

Including also the drivetrain flexibility (fully flexible case), a strong  $6\Omega$  load variation in  $F_{x\ TowerTop}$  occurs. It is an interesting observation that the drivetrain flexibility alone had a very small impact on the axial tower top load, cf. Fig. 4-16, but in combination with the tower flexibility, the impact on  $F_{x\ TowerTop}$  becomes significant. The reason for this interference can be attributed to the nacelle nodding mode. In Fig. 4-18, the effect of a  $6\Omega$  oscillation has been observed for  $M_{y\ TowerBottom}$  with a rigid tower, due to the nacelle nodding. With the tower being flexible in the fully flexible case, this load results in a  $6\Omega$  motion of the tower top and this motion can be observed also in the tower top load  $F_{x\ TowerTop}$ . Comparing this finding to the hub load  $F_{x\ Hub}$  in Fig. 4-21, the influence of the fully flexible turbine can be observed. However, for  $F_{x\ Hub}$  this effect is small as the nacelle nodding and the tower fore-aft motion form a common mode, which does not transfer the load back to the hub.

Continuing the comparison with the cases V and VI, they differ in their treatment of the torsional stiffness of the ground. While case VI assumes the ground to be rigid in torsional direction, case V assumes torsional flexibility, and subsequently the two cases differ in their results on the nacelle yawing motion and load. Fig. 4-23 shows the tower top torsional moment  $Q_{z\ TowerTop}$ . As can be seen, taking the torsional flexibility of the tower into account increases the  $Q_{z\ TowerTop}$  load amplitude compared to the rigid case. Especially, in case V the loads are significantly higher. This is a result of the lower stiffness of the system and subsequently higher motion amplitudes in case V. The transition piece (case VII), the

drivetrain and nacelle flexibility (fully flexible case) are of minor importance for the tower top torsion.

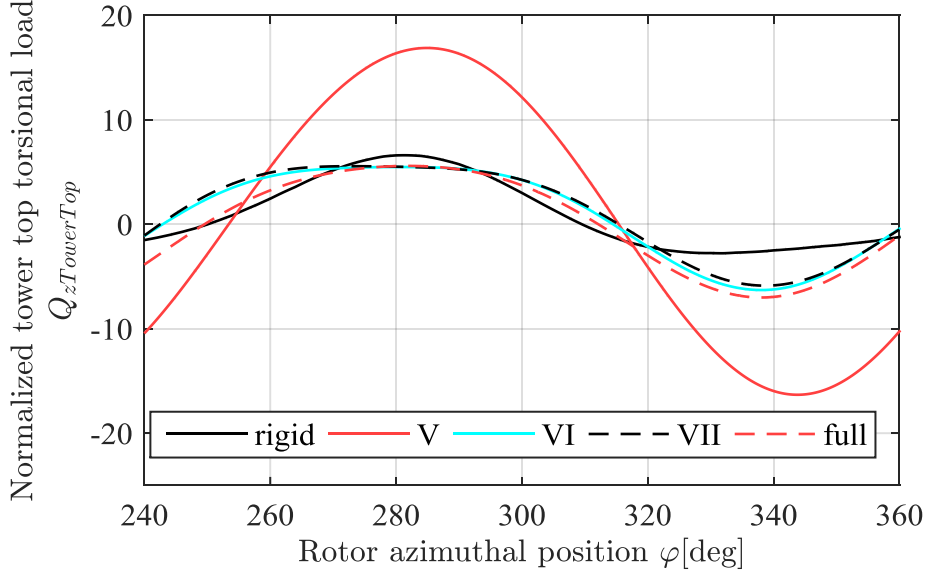


Fig. 4-23: Tower top torsional load  $Q_{z\,TowerTop}$  with varying fixed-structure flexibility normalized with mean value  $\bar{Q}_{z\,TowerTop}|_{rigid}$

For the tower bottom bending moment  $M_{y\,TowerBottom}$ , Fig. 4-24, the tower flexibility results in approximately the same load amplitude as in the rigid case, but the phase is shifted by  $\theta \approx 0.87 \cdot \pi$ . As the tower eigenfrequency  $f_0$  is significantly lower than the excitation  $f$  this phase shift is the expected result from a 1DoF oscillator, (4-2), cf. Fig. 4-25 with the amplitude response ratio  $A/A_0$ , phase shift  $\theta$  and the damping ratio  $\zeta$ .

$$\frac{A}{A_0} = \frac{1}{\sqrt{\left(1 - \left(\frac{f}{f_0}\right)^2\right)^2 + \left(2 \cdot \frac{f}{f_0} \cdot \zeta\right)^2}} \quad \theta = \arctan\left(\frac{2 \frac{f}{f_0} \cdot \zeta}{1 - \left(\frac{f}{f_0}\right)^2}\right) \quad (4-2)$$

Considering also the drivetrain and nacelle flexibility, the  $6\Omega$  component, discussed for  $F_{x\,TowerTop}$ , can be seen also for  $M_{y\,TowerBottom}$ . The overall load amplitude is thereby reduced due to the phase match of the  $3\Omega$  and  $6\Omega$  component.

Based on these findings it can be concluded that for the present load case the tower and the nacelle flexibility influence the loads considerably. The other flexibilities are relevant for some specific loads, but have a minor impact on the overall hydroelastic behavior of the turbine.

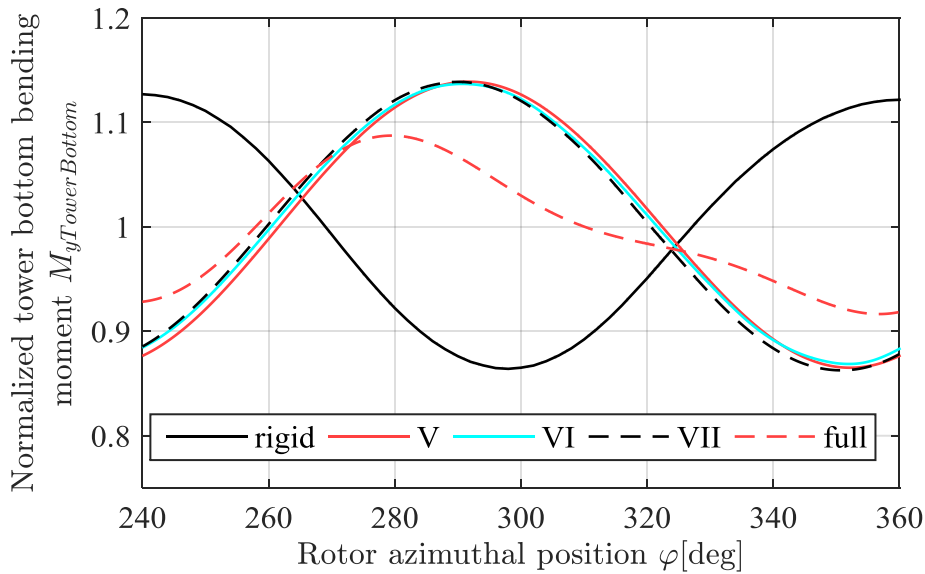


Fig. 4-24: Tower bottom bending moment  $M_{yTowerBottom}$  with varying fixed-structure flexibility normalized with mean value  $\bar{M}_{yTowerBottom}|_{rigid}$

#### 4.4. Operation in Point of Resonance

At multiple occasions in the previous section on the hydroelastic response, the ratio of the excitation frequency and the eigenfrequencies has been mentioned. Following this reasoning, a large impact of the point of operation on the hydroelastic response can be expected. Therefore, the investigation in Section 4.3 needs to be extended to further points of operation. Especially, the analysis of the operation at resonance of the structural components might reveal different results. This is investigated here by analyzing the loads at resonance operation with constant rotor speed, followed by a simulation of riding-through the resonance with a deceleration of the rotor speed.

##### 4.4.1 Steady Resonance Operation

To evaluate the impact of the operation in resonance, four additional points of operation are simulated here. As shown in Fig. 4-25, these are split into a set with the constant tip speed ratio  $2 \cdot \lambda_{TSR\ opt}$  and a set with the constant current speed  $v_1 = 4\text{m/s}$ . The points of operation cover the range from above to below resonance with respect to the first tower eigenfrequency.

Fig. 4-25 shows a large increase of the amplitude of the tower bottom bending moment  $M_{yTowerBottom}$  at resonance. Here, an increase of the loads by a factor five is observed

compared to results for a rigid setup. As the hydrodynamic damping is in the same order of magnitude for the chosen tip speed ratios and current speeds, the impact of the points of operation can be reduced to the excitation frequency. Nevertheless, the absolute values of the load amplitudes differ between the cases.

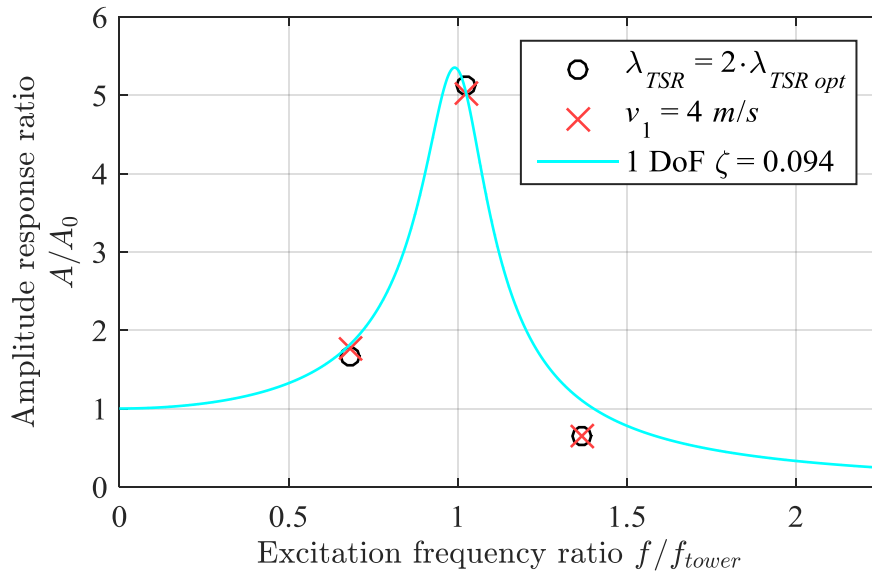


Fig. 4-25: Amplitude response ratio  $A/A_0$  of tower bottom bending moment  $M_{y\ TowerBottom}$  to excitation ratios  $f/f_{tower}$

The comparison of the results to the theoretical 1 DoF oscillator, cf. (4-2), gives a reasonable match. However, the agreement is not perfect, due to the higher harmonic oscillations. This behavior was also observed and analyzed for the case of  $4\ m/s$  current speed and tip speed ratio  $2 \cdot \lambda_{TSR\ opt}$  in Section 4.3.5. As can be seen from Fig. 4-26, the impact of the higher order frequencies increases with increasing current velocity, and the time series of the load deviates from the sinusoidal shape at lower current speeds.

This analysis indicates a massive load increase in case of resonance; however, at the different locations in the turbine the load amplification differs. Fig. 4-27 shows the axial force for the resonance response at the tower top,  $F_{x\ TowerTop}$ , and at the hub connection,  $F_{x\ Hub}$ . As can be seen, moving from tower bottom to tower top, the resonance load factor of five is reduced to three. Moving on to the hub, there is no increase in the axial hub force loads, shown here, during resonance operation.



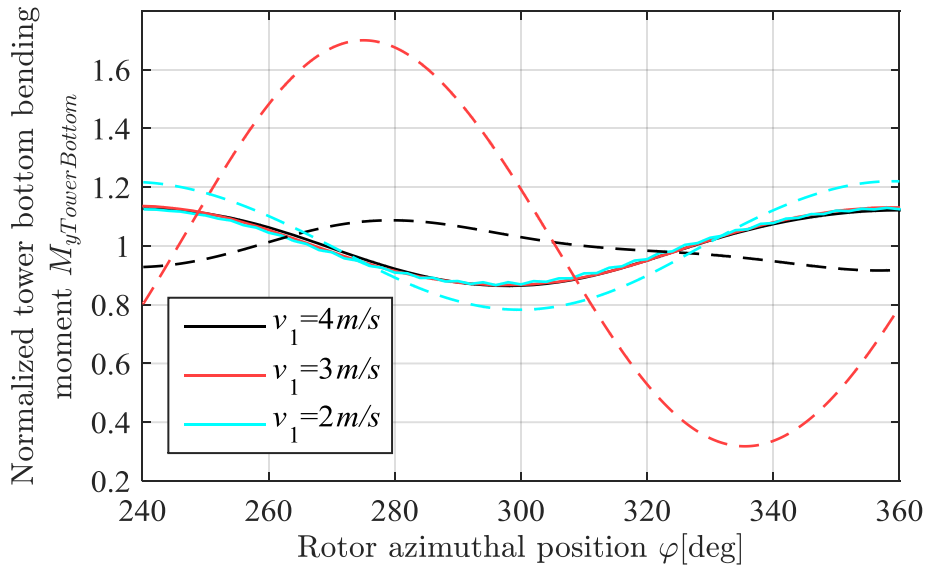


Fig. 4-26: Tower bottom bending moment  $M_{yTowerBottom}$  for  $\lambda_{TSR} = 2 \cdot \lambda_{TSR opt}$  in fully flexible (dashed) and rigid (solid) setup normalized with the corresponding mean values  $\bar{M}_{yTowerBottom}|_{rigid}(v_1)$

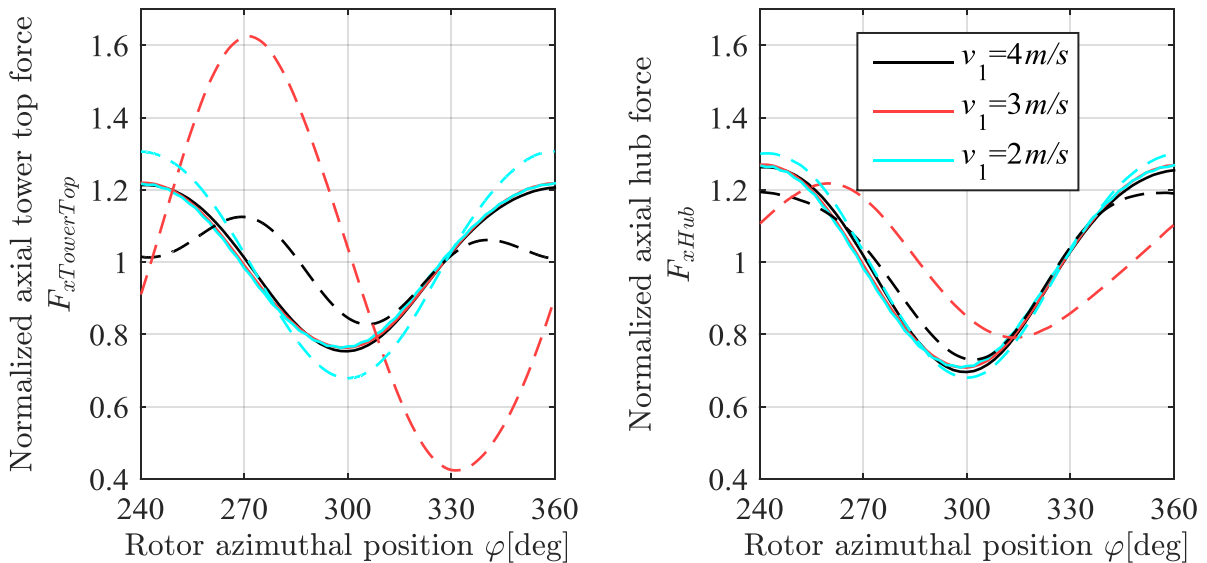


Fig. 4-27: Axial tower top load  $F_{xTowerTop}$  (left) and axial hub force  $F_{xHub}$  (right) for  $\lambda_{TSR} = 2 \cdot \lambda_{TSR opt}$  in fully flexible (dashed) and rigid (solid) setup normalized with the corresponding mean values

This location dependency of the resonance effect is mainly a result of the mass distribution. Each mass of the system needs to be accelerated according to the system motion and causes a compensating load  $F = m \cdot a$ . Furthermore, due to the motion of the rotor and considering the tower fore-aft mode, the rotor hydrodynamics result in lower thrust amplitudes compared to

the rigid case, decreasing the local loads further. In Fig. 4-27 also the load amplitude in the rigid case between the two locations seems to differ. However, this is only an artifact from the normalization with the respective mean value, which differs due to nacelle drag.

The steady operation at resonance causes a significant load increase. However, these are not necessarily spread evenly across the entire turbine system. A detailed analysis of the specific turbine system is required here. For the present case of the Voith HyTide<sup>®</sup> turbine the tower resonance should be avoided to limit the fatigue and extreme loads on the tower, but is of minor importance for, e.g., the hub design.

#### 4.4.2 Transient Ride-Through of Resonance

The issue of resonance is typically avoided on tidal current turbines by changing the rotational speed quickly in a short time to ride-through the resonance frequency. This approach is adopted from wind energy, [21]. To evaluate the loads during such a passage, the simulation setup is extended here to a variable speed case. For a current speed of  $4\text{m/s}$ , the rotational speed of the turbine is decelerated from  $2 \cdot \lambda_{TSR\ opt}$  to  $\lambda_{TSR\ opt}$ . This change in rotational speed is described in the numerical setup as an additional rotational deformation of the rotor domain, which requires an adaption of the grid deformation algorithms, detailed in Appendix B, p. 145.

For the passage time, [32] calculated that a 1MW tidal turbine takes  $1\text{s}$  to speed up from design condition to run-away condition upon a generator torque loss ( $P_{el} = 0\text{W}$ ). However, during normal operation this is unrealistically fast, as the allowed variation of electrical power output is limited. Hence, a passage time of  $2\text{s}$  is chosen here with a linear change in rotational speed, Fig. 4-28. Resonance operation occurs at  $t = 1\text{s}$ , cf. Fig. 4-25.

The loads on the tower bottom and the tower top for this transient event are shown in Fig. 4-29. As can be seen, even with the quick ride-through procedure, the onset of resonance can not be fully prevented. However, the amplitude ratio for the tower bottom bending moment  $M_{y\ TowerBottom}$ , which was about five for steady operation in resonance, cf. Fig. 4-25, is reduced here to approximately four. The same reduction in the load amplitude ratio applies also to the tower top load  $F_{x\ TowerTop}$ .

Further changes in the loads occur due to the riding-through. Despite that the deceleration ends at  $t = 2\text{s}$ , in both,  $M_{y\ TowerBottom}$  and  $F_{x\ TowerTop}$ , a variation of the loads can be still observed afterwards for the flexible and the rigid case. This is caused by the dynamic inflow.

With the change in rotational speed, the thrust coefficient  $c_{th}$ , and thus the axial induction  $a_{ax}$  change aswell. However, this change does not occur instantaneously due to the inertia of the fluid, resulting in a time delay of ca. 4s in the present case to reach steady flow conditions. Taking also the flexibility and dynamic motions of the turbine structure into account, the flexible case requires several seconds more for the onset of the steady oscillation.

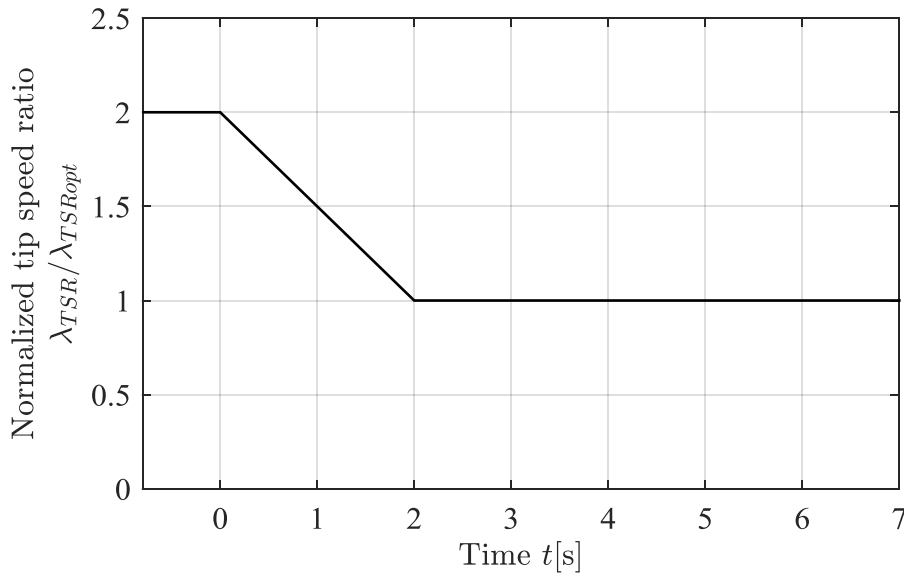


Fig. 4-28: Linear deceleration of rotational speed for passage of resonance

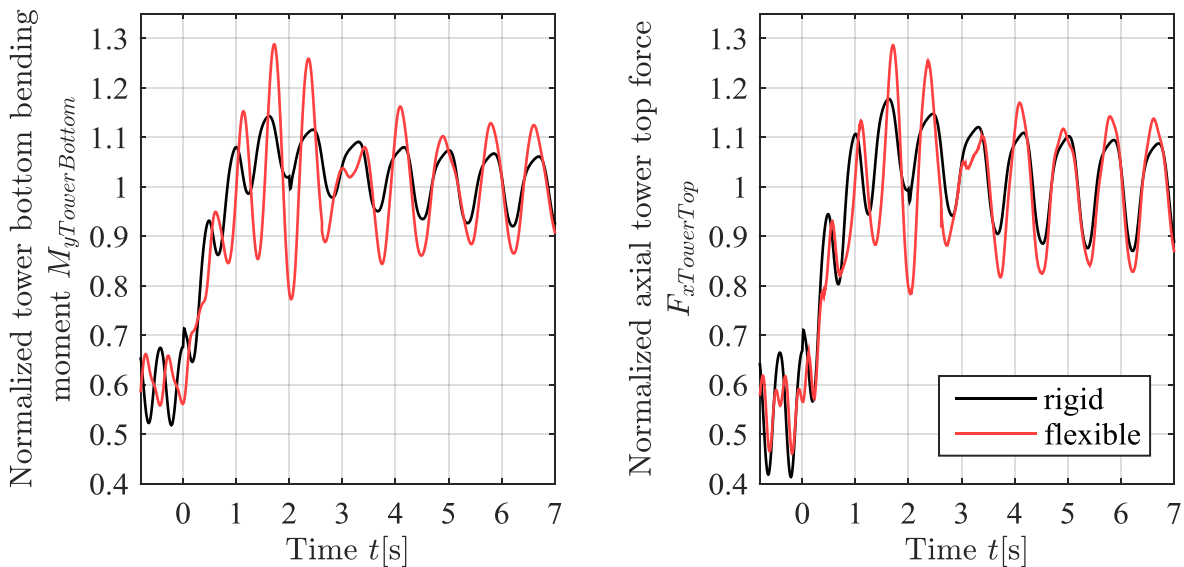


Fig. 4-29: Tower bottom bending moment  $M_{yTowerBottom}$  (left) and axial tower top load  $F_{xTowerTop}$  (right) during passage of resonance normalized with the corresponding mean values at  $t > 6s$

In the analysis of the flexibility shown in Section 4.3, the main shaft was found to have a negligible impact on the loads. In the here investigated transient load case however, a significant impact can be observed for the hub torque  $Q_{xHub}$ , Fig. 4-30. In order to decelerate the turbine, the generator torque is increased to follow the prescribed rotational speed in the generator, Fig. 4-28. This causes a step response of the main shaft in its torsional mode. As this mode has a low hydrodynamic damping, the oscillation persists during the complete riding-through. However, this is only a local load and the main shaft's torsional motion does not transfer the loads in a relevant extent to, e.g., the tower.

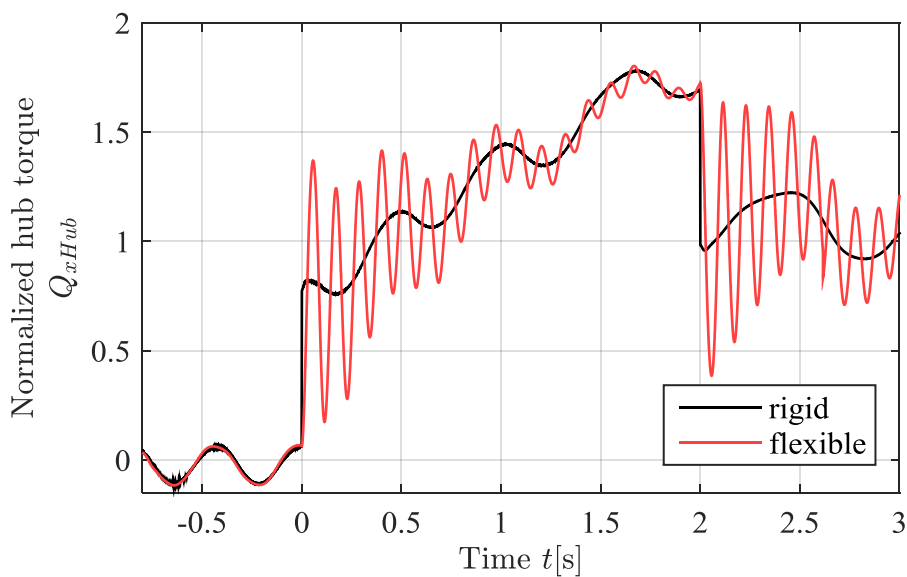


Fig. 4-30: Response of hub torque  $Q_{xHub}$  to deceleration of generator rotational speed normalized with the mean value at  $t > 6s$

A transient passage of resonance within a short period can therefore be used to limit the effect of the resonance. This affects mainly the fatigue load, as the number of high amplitude oscillations is reduced. The extreme loads are reduced with this maneuver, but the change in loads is small compared to a rigid structure.

#### 4.5. Summary of Hydroelastic Results

The hydroelasticity of the turbine has been investigated in three steps. In an initial rigid simulation approach, the vortex structures during operation have been analyzed. Here, especially the 3-dimensional inflow to the rotor and a horseshoe-vortex along the nacelle are of importance, as these influence directly the loads on the rotor in lee operation. Furthermore, the impact of the numerical setup on the load time series has been analyzed. This showed a

large impact of the time scheme order, which was limited to 1<sup>st</sup> order for stability reasons in the hydroelastic simulations.

Based on those rigid results, the lee operational point at  $\lambda_{TSR} = 2 \cdot \lambda_{TSR\ opt}$  and cut-out current speed,  $v_1 = 4\text{m/s}$ , was chosen and simulated with the fluid-multibody-interaction method (FMBI), introduced in Section 3.2. By systematically increasing the complexity of the structural model, and considering further flexibilities, it has been shown that the hydroelastic response of the Voith HyTide<sup>®</sup>-turbine is dominated by the tower and nacelle flexibility. This stands in contrast to findings from the literature, claiming that the flexibility of the rotor blade of a tidal turbine has the largest impact. The blade's flexibility was found here to be only relevant for very soft rotor blades.

The investigation was then extended to resonance operation. The resulting amplitude response plot showed up to five times higher loads at the tower bottom, but only minor changes in loads for, e.g., the hub during tower resonance. It was also shown that riding-through the point of resonance in a short time results in slightly reduced load amplitudes, which are still four times larger than the loads on a rigid turbine, but can reduce significantly the fatigue loads.



## 5. EVALUATION OF THE LOAD REDUCTION POTENTIAL

The following section evaluates the potential of changes in the turbine concept with respect to the results of the hydroelastic simulations. In a first step, this is done by discussing the potential of different strategic directions, covering the system damping, geometric modifications and operational modifications. Based on its results, the discussion is followed by a more detailed analysis of the controller system, which is shown to have the highest potential. A new strategy of controlling the turbine will be introduced and its feasibility shown. The section then closes by analyzing the impact of the suggested changes in the controller on the turbine's hydroelastic behavior.

### 5.1. Assessment of Potential

The assessment of potential for load reduction is based here on an analysis of the amplitude response plot, Fig. 5-1, and strategies to reduce the resulting loads are discussed. The response amplitude  $\hat{F}_{res}$  is based on the four variables of damping ratio  $\zeta$ , load amplitude  $\hat{F}$ , resonance frequency  $f_0$ , and excitation frequency  $f$ . Within this section, strategies associated to each of those variables are discussed and evaluated regarding their potential.

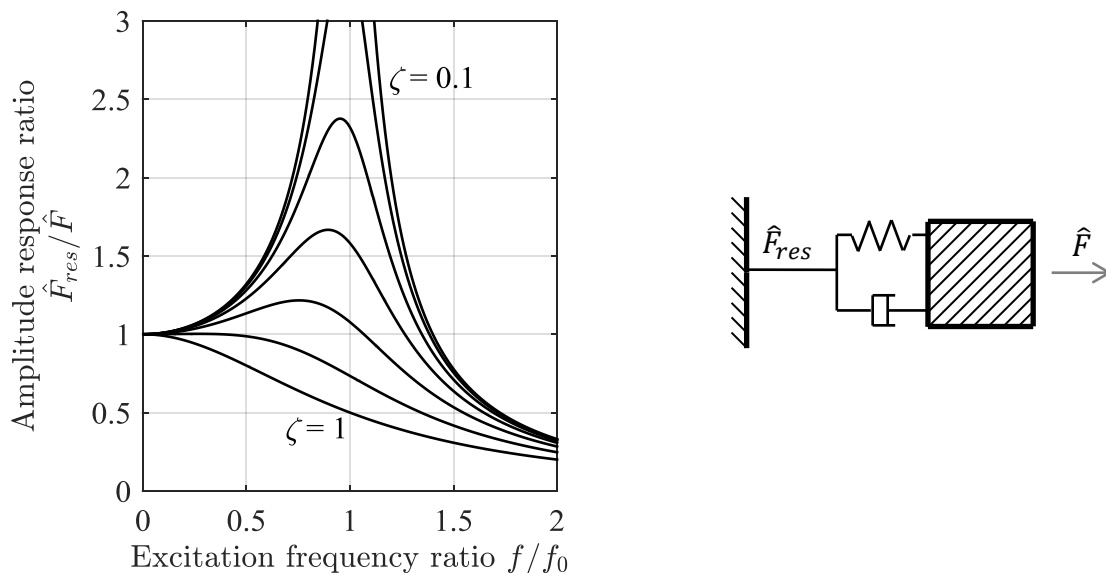


Fig. 5-1: Load amplitude response ratio (left) through a spring-mass-damper-system (right) with varying damping ratios  $0.1 \leq \zeta \leq 1$  in logarithmic row

The target for those strategies, can be deduced from the amplitude response plot by splitting it into three regions with respect to the frequency ratio:  $f/f_0 \ll 1$ ,  $f/f_0 \approx 1$ , and  $f/f_0 \gg 1$ . In

case of a low excitation frequency compared to resonance, a neutral behavior occurs as the dynamics follow the load with a negligible impact of the mass acceleration and therefore no change in the loads,  $\hat{F}_{res} \approx \hat{F}$ . On the other hand, with a high excitation frequency, the system forms a lowpass filter behavior with a reduced load,  $\hat{F}_{res} < \hat{F}$ . Between those, the resonance region occurs with significantly increased loads,  $\hat{F}_{res} \gg \hat{F}$ . The latter highly depends on the damping of the system and vanishes in case of an over critical damping ratio.

The design target for the system is therefore to reach the lowpass filter region, or if this is not possible, at least the neutral region. As named, the design parameters for this are  $f$ ,  $f_0$ ,  $\zeta$  and  $\hat{F}$ , which can be adapted by geometric, structural or operational modifications.

### 5.1.1 System Damping

The probably most effective way to reduce loads would be to increase the damping of the system. This would reduce the number of oscillations of the system considering a step response and, as described, reduces the extend of the resonance region for periodic loads.

#### 5.1.1.1 Structural Damping

Damping can be split into the structural or material damping and the hydrodynamic damping. The structural damping is mainly depending on the materials. E.g., steel has typically a two times lower material damping than composite materials, and 40 times lower than prestressed concrete, [10]. However, with the material obviously also the structural strength and the manufacturing costs varies. Changing the material to a higher structural damping is therefore limited and requires careful consideration.

Another way to approach to the structural damping is a change in the stiffness of the system. The lower the stiffness and thus the resonance frequency, the lower is the mass fraction participating in the structural damping and thus the lower is the absolute damping. However, besides the crosstalk in design between the change in damping and resonance frequency, reducing the structural stiffness could lead to buckling and other issues with the structural strength, while increasing it would also increase the system mass and renders the same magnitude of loads less sever.

Further, secondary systems for damping could be used. These can be either active systems like controller damping, [30], [75], which require additional sensor inputs and thus may cause



down times on failures, or passive systems like tuned mass dampers, [74], which increase the mass of the system.

### 5.1.1.2 Hydrodynamic Damping

The hydrodynamic damping is, besides the structural damping, the second important contribution to the overall damping. Similar to the tuned mass dampers, it is a passive system, but it is based on the already implemented component rotor blade. Assuming a constant thrust coefficient  $c_{th}$  and current velocity  $v_1$ , the thrust force  $F_{th}$  depends on the rotor fore-aft-velocity  $v_{fa}$ , (5-1), with the rotor radius  $R$  and the fluid density  $\rho$ , cf. (2-4).

$$F_{th} = \frac{\rho}{2} \pi R^2 \cdot (v_1 + v_{fa})^2 \cdot c_{th} \quad (5-1)$$

By this equation, any motion is countered by an opposing change in thrust load and the structural motion is quadratically damped. However, the thrust coefficient  $c_{th}$  is not constant but depends on the relative tip speed ratio  $\lambda'_{TSR}$ , which also changes with the fore-aft motion, (5-2), with the rotor speed  $\Omega$ .

$$\lambda'_{TSR} = \frac{\Omega \cdot R}{v_1 + v_{fa}} \quad (5-2)$$

Assuming low speeds of motion,  $v_{fa} \ll v_1$ , the thrust force during a rotor fore-aft motion can be calculated with a linearization of the steady thrust coefficient curve  $c_{th}(\lambda_{TSR})$  at the point of operation  $\lambda_{TSR}$ , (5-3).

$$F_{th} = \frac{\rho}{2} \pi R^2 \cdot (v_1 + v_{fa})^2 \cdot \left( c_{th}|_{\lambda_{TSR}} + \left. \frac{dc_{th}}{d\lambda_{TSR}} \right|_{\lambda_{TSR}} \cdot (\lambda'_{TSR} - \lambda_{TSR}) \right) \quad (5-3)$$

The hydrodynamic damping therefore decreases with a rising thrust curve slope  $dc_{th}/d\lambda_{TSR}$ . The critical value is a constant thrust force independent of  $v_{fa}$ . This is shown in (5-4) with the abbreviation  $\tilde{v} = v_{fa}/v_1$ , and the assumption of a constant rotor speed and quasi-static hydrodynamics. The derivation of this equation is shown in Appendix B, p. 147.

$$F_{th} = const \Rightarrow c_{th} = (1 + \tilde{v})^2 \cdot \left( c_{th} + \left. \frac{dc_{th}}{d\lambda_{TSR}} \right|_{\zeta=0} \cdot \lambda_{TSR} \cdot \frac{-\tilde{v}}{1+\tilde{v}} \right) \quad (5-4)$$

$$\left. \frac{dc_{th}}{d\lambda_{TSR}} \right|_{\zeta=0, \tilde{v} \rightarrow 0} = \frac{2 \cdot c_{th}}{\lambda_{TSR}}$$

If the thrust curve slope is larger than this limiting value, the system gets unstable and flutter occurs independently from the eigenfrequency. It therefore can be concluded that the thrust curve slope needs to be small to achieve a high hydrodynamic system damping and thus a low amplitude response  $\hat{F}_{res}/\hat{F}$ .

Assuming fast structural motions on the other hand, the rotor leaves the steady performance curve  $c_{th}(\lambda_{TSR})$  due to the inertia of the fluid. With  $\tilde{v} \gg 0$ , the induction factor  $a$  can be approximated to be constant and the thrust force respectively lift force  $F_l$  changes with the lift curve slope  $dc_l/d\alpha_{AoA}$  on each radial slice. Applying the same procedure as for slow motions, the limiting value for the lift curve slope can be derived, (5-5), cf. Appendix B, p. 148.

$$F_l = const$$

$$\left. \frac{dc_l}{d\alpha_{AoA}} \right|_{\zeta=0} = \frac{-(\tilde{v}^2 + 2 \cdot \tilde{v} \cdot (1 - a)) \cdot c_l}{\left( \text{atan}\left(\frac{\tilde{v} + 1 - a}{\lambda'_{TSR}}\right) - \text{atan}\left(\frac{1 - a}{\lambda'_{TSR}}\right) \right) \cdot \left( (\tilde{v} - a + 1)^2 + \frac{1}{\lambda'^2_{TSR}} \right)} \quad (5-5)$$

This behavior occurs for the individual slices of the rotor with the local tip speed ratio and the damping ratio is subsequently mode shape dependent.

For increasing the hydrodynamic damping, the thrust curve slope therefore can be reduced, and the lift curve slope increased respectively. However, such a change is not arbitrarily possible, but requires a modification of the chord, twist and hydrofoil distribution of the rotor blade. It is therefore possible to improve the performance in a single point of operation, but on the cost of reduced performance in the other points. In case of the Voith HyTide<sup>®</sup> turbine this method is already used to reduce the thrust coefficient and the thrust curve slope for high tip speed ratios, but with adverse effects on the peak performance. A balance of those two design targets is achieved with an acceptable hydrodynamic damping, while maintaining a good maximum power coefficient, [14].

Another issue that needs to be kept in mind is that the hydrodynamic damping forces are introduced by the rotor blades into the system, but the mass in motion is distributed around the nacelle. Therefore, the damping forces need to be passed through the turbine system towards the masses, increasing the local loads. Also, the target of high load variations with changes in the relative motion of nacelle and fluid, which are the physical core of the damping, opposes the design target of a low excitation load amplitude  $\hat{F}$ , while operating in

turbulent fluctuating currents, [23]. Increasing the hydrodynamic damping therefore improves the system performance in steady and laboratory environments, but might have a negative impact in a real world application.

### 5.1.2 Geometric Modifications

Geometric modifications to the system can either be used to achieve an increased damping, or can be used to reduce the apparent load amplitudes. As discussed in the previous section for the rotor blades, those targets are opposing according to the hydrodynamic damping. However, potential exists for the transition piece wake. It has been shown in the rigid simulations, Section 4.1.3, that the rotor blades operate at the edge of the tower and transition piece wake structure. Therefore, one option for improvements is to increase the rotor-tower distance. This is mainly a construction issue, as the flipping moments increase, requiring a higher stiffness of the system.

Another possibility is a change in the outer shape of the transition piece between the tower and nacelle, which is rectangular in the investigated design with subsequently large vortex structures. Fig. 5-2 shows a comparison to modified geometries with same width,  $\Delta y \geq 2m$ , and cross-sectional area,  $A_{TP} = 5m^2$ , as the current transition piece. It can be seen that the size of the wake and thus the loads on the turbine can be reduced by these modifications without large adverse impacts on the system design and costs of the relevant parts.

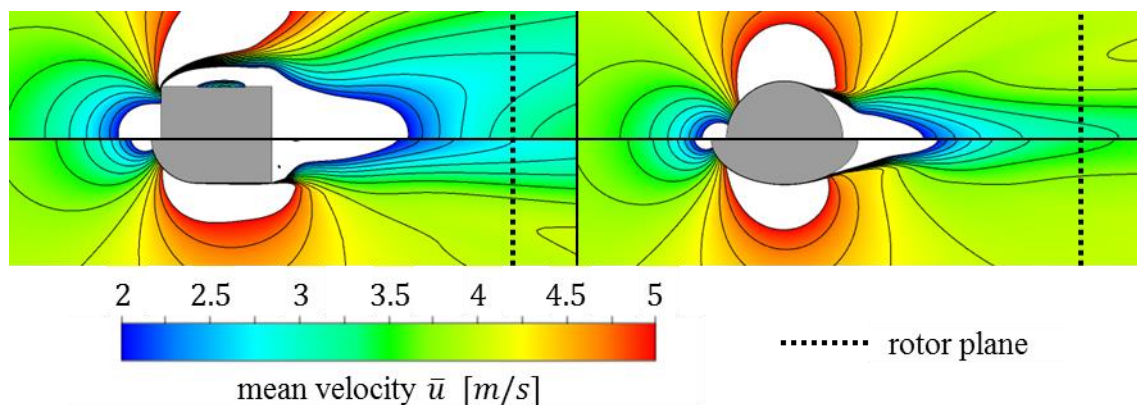


Fig. 5-2: 2-dimensional simulation results for the time averaged wake velocity  $\bar{u}$  with  $v_1 = 4m/s$  of four different transition piece cross-sections each shown as half field

Among the here shown shapes, the elliptical cross-section gives lowest wake deficit for fluctuating inflow angles. Hydrofoil shapes typically reduce the wake deficit further in the design point, however have a smaller range of inflow angles with a reduced wake deficit and

can cause high side loads on the tower. Therefore, the elliptical cross-section offers the highest potential for hydrodynamic load reductions and should be investigated further for optimal aspect ratio, structural design, manufacturing issues, etc.

### 5.1.3 Operational Modifications

In the previous subsections it has been shown that structural and geometric modifications offer some possibilities to improve the hydroelastic performance. However, most of those approaches lead to finding a suitable balance for the design targets. This balance has a rather flat optima and thus the design ends up with avoiding design flaws. The approach of operational modifications differs. This approach aims not on improving the performance for a given point of operation, but on avoiding any critical points of operation and thus influencing the excitation frequency. This is done by the controller of the turbine and in the specific case of a variable speed fixed pitch tidal turbine by adjusting the generator speed and torque.

On wind turbines, this is typically done by holding the generator torque constant in proximity to a critical speed. A change in the rotor's aerodynamic respectively hydrodynamic torque therefore causes the system to accelerate or decelerate through the critical speed and the onset of resonance is prevented. As shown in Section 4.4.2, despite such a fast riding-through can limit the full onset of resonance, it can not prevent the high loads.

Further, the power loss, due to the tip speed ratio  $\lambda_{TSR}$  being not optimal during this time, is small in sub-rated operation as the power coefficient  $c_p$  is close to constant,  $dc_p/d\lambda_{TSR} \approx 0$ . However, considering the overspeed power limitation strategy of the Voith HyTide<sup>®</sup> turbine, for the above-rated operation this method would cause large variations in the energy production, as  $|dc_p/d\lambda_{TSR}| \gg 0$ .

Nevertheless, avoiding critical points of operation offers still the highest potential for load reduction. Therefore, a strategy is required, which removes all high rotational speeds, close to resonance frequencies, from operation, while maintaining the desired power production and rated power output. An example for such a strategy is the underspeed controller, discussed in the following section.

## 5.2. Underspeed Controlled Operation

Based on the above results of the discussion, the load reduction potential of avoiding high rotational frequencies, and thus the potential of the underspeed controller is considered

---

highest among the available options. Within the following section, the concept of the underspeed controller will be introduced and the feasibility shown by a stability analysis. The stability analysis results in a set of controller gains, which are then applied to simulate the stochastic loads on the system with a simplified model. The section concludes with a performance evaluation with respect to subsequent strategic impacts of the underspeed controller.

### 5.2.1 Controller Concept

To limit the power of the rotor, the performance of the hydrofoils on the rotor needs to be reduced. This can be done either by reducing the angle of attack and lift coefficient with an increase in the rotational speed or a pitch change of the rotor blades, or by triggering stall on the rotor blades. Increasing the rotational speed is the state-of-the-art approach of the overspeed controller installed to the Voith HyTide<sup>®</sup> turbine, causing the discussed issues of high excitation frequencies, Section 5.1. Installing a pitch, on the other hand, would jeopardize the intended reliability of the system. Thus, it is proposed here to limit the power production by reducing the rotational speed and trigger stall here with the underspeed controller.

By increasing the torque of the generator during operation, the rotor can be decelerated and the tip speed ratio is reduced. As this enlarges or onsets the stall on the rotor blades, this temporal increase in the generator torque and electrical power therefore reduces the hydrodynamic power. As the hydrodynamic power is the source for the electrical power, this indicates the dilemma of the underspeed controller: To reduce the electrical power output of the turbine, the electrical power of the generator needs to be temporarily increased. The underspeed controller therefore operates in an unstable point of operation, which needs to be stabilized by the controller. Subsequently it is not able to maintain a constant electrical power output, but is only able to hold the mean power output equal to the rated power,  $\bar{P}_{el} = P_{rated}$ .

Despite this disadvantage of the underspeed controller compared to the overspeed controller, which operates at a stable point of operation with a constant power output, the underspeed controller offers a reduced thrust coefficient, besides the reduced excitation frequency and thus number of load cycles. This is shown in Fig. 5-3 (left) based on the steady performance curve of the rotor for an exemplary set-point. While both controllers require the same power

coefficient  $c_p$  for rated power, the thrust coefficient  $c_{th}$  for the respective tip speed ratio differs in favor of the underspeed concept.

Calculating the set-points for all current speeds, the generator torque  $Q_{el}$  over rotational speed  $\Omega$  of the rotor can be deduced, Fig. 5-3 (right). It can be seen that the usual method of calculating the torque as a function of the rotational speed  $\Omega$ ,  $Q_{el} = f(\Omega)$ , is not applicable here as multiple torque values correlate to a single rotational speed. Instead, the optimal speed  $\Omega_{opt}$  needs to be defined based on the electrical torque,  $\Omega_{opt} = f(Q_{el})$ , to associate a unique output value to each input. The set-point curve consists of a hyperbolic section of constant power for above rated operation and a parabolic section of constant tip speed ratio,  $\lambda_{TSR} = \lambda_{TSR_{opt}}$ , for optimal power production in below rated conditions, (5-6), [21], with the rotor radius  $R$ , fluid density  $\rho$  and peak power coefficient  $c_{p_{opt}} = c_p(\lambda_{TSR_{opt}})$ .

$$\Omega_{opt} = f(Q_{el}) = \min \left( \frac{P_{rated}}{Q_{el}}, \sqrt{\frac{Q_{el}}{\left( \frac{\rho \pi R^5 \cdot c_{p_{opt}}}{2 \cdot \lambda_{TSR_{opt}}^3} \right)}} \right) \quad (5-6)$$

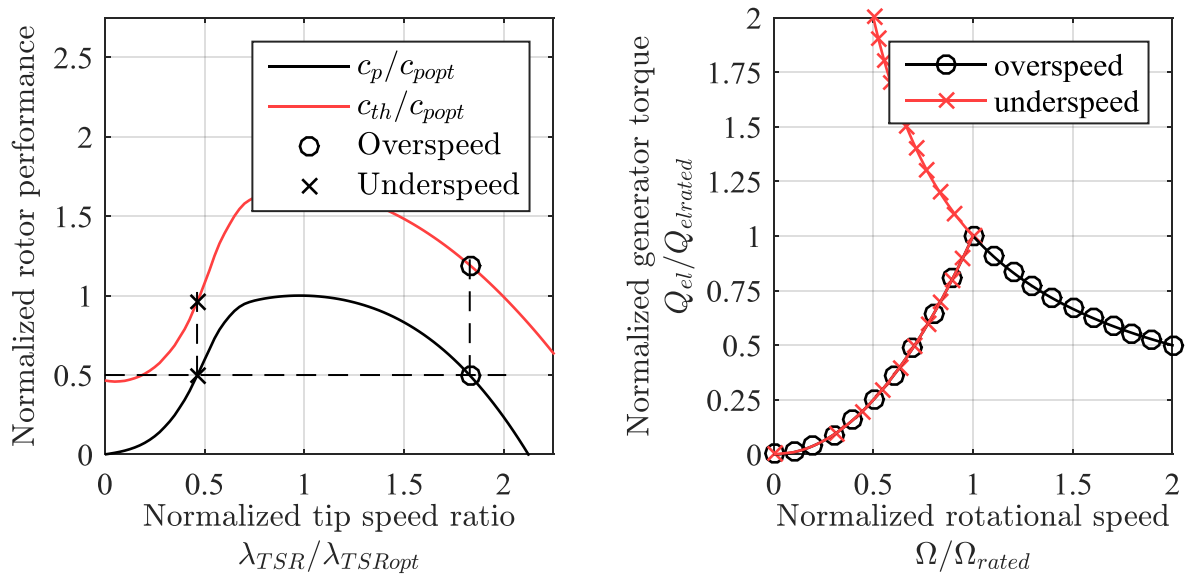


Fig. 5-3: Steady operation for the overspeed and underspeed controller in the rotor performance curve with an exemplary set point (left) and the generator set point curve (right)

Based on this correlation of  $\Omega_{opt} = f(Q_{el})$ , the controller can be split into two cascades, Fig. 5-4: An inner closed-loop with the input of a required rotational speed  $\Omega_{req}$  and the turbines rotational speed  $\Omega$  on the output, and an outer closed-loop to calculate the value of  $\Omega_{req}$  from

the electrical torque  $Q_{el}$ . The inner closed-loop consists of the turbine  $G_{turbine} = G_{Q_{el} \rightarrow \Omega}$  with the generator torque  $Q_{el}$  as input calculated by a PI-controller  $G_{PI} = G_{\varepsilon \rightarrow Q_{el}}$  on the input disturbance  $\varepsilon = \Omega - \Omega_{req}$ . The inner closed-loop is further disturbed by the hydrodynamic torque  $Q_{Hydro}$  acting on the turbine with  $G_{Q_{Hydro} \rightarrow \Omega}$ . The internals of the outer-loops transfer function  $G_{Q_{el} \rightarrow \Omega_{req}}$  will be discussed in the next section.

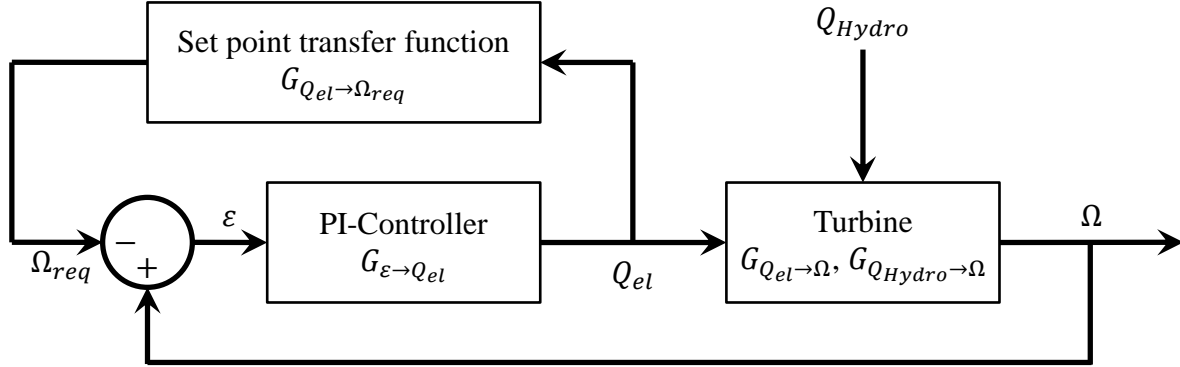


Fig. 5-4: Cascaded structure of underspeed controller

## 5.2.2 Discussion of Stability

To prove the feasibility of the proposed underspeed controller, the stability limits need to be calculated. This is done here by splitting the controller into its inner and outer closed-loop, and evaluating them separately by calculating their pole locations. These results are further used to find a suitable set of controller parameters in the last step of the stability analysis.

### 5.2.2.1 Inner Closed-Loop Stability

By analyzing the inner closed-loop separately, the response of the PI-controller and the turbine can be isolated. Thus, the stability limits for the PI-parameters  $k_p$  and  $k_I$  can be calculated based on a linear set of differential equations of the type  $\dot{\vec{x}} = \mathbf{A}_I \cdot \vec{x} + b_I$ , representing the dynamics of the inner closed-loop.

Based on the input disturbance  $\varepsilon = \Omega - \Omega_{req}$ , the dynamics are described here as the combination of the PI-controller, (5-7), the rotational DoF of the rotor with the speed  $\Omega$  and the inertia  $J$ , (5-8), and the rotor hydrodynamic torque  $Q_{Hydro}$ , linearized on the analyzed set-point  $\Omega_0$ , (5-9).

$$Q_{el} = k_p \cdot \varepsilon + k_I \cdot \int \varepsilon \quad (5-7)$$

$$\dot{\varepsilon} = \frac{1}{J} \cdot (Q_{Hydro} - Q_{el}) \quad (5-8)$$

$$Q_{Hydro} = Q_{Hydro}|_{\Omega_0} + \varepsilon \cdot \left. \frac{dQ_{Hydro}}{d\Omega} \right|_{\Omega_0} \quad (5-9)$$

These dynamics neglect all but the rotational DoF of the system, which is an assumption made for simplicity here. In Section 5.2.3, the operational loads on the turbine will be analyzed including the further DoF of nacelle motion.

With the substitute  $\vec{x}$  for the states, (5-10), the dynamics can be summarized to the linear set of differential equations, (5-11).

$$\vec{x} = \begin{bmatrix} \int \varepsilon dt \\ \varepsilon \end{bmatrix} \quad (5-10)$$

$$\dot{\vec{x}} = \underbrace{\begin{bmatrix} 0 & 1 \\ -\frac{k_I}{J} & \frac{1}{J} \cdot \left( \left. \frac{dQ_{Hydro}}{d\Omega} \right|_{\Omega_0} - k_p \right) \end{bmatrix}}_{A_I} \cdot \vec{x} + \underbrace{\begin{bmatrix} 0 \\ \frac{Q_{Hydro}|_{\Omega_0}}{J} \end{bmatrix}}_{b_I} \quad (5-11)$$

With this set of equations, the poles representing the harmonic solutions of the inner closed-loop can be derived by calculating the eigenvalues  $\lambda$ , (5-12).

$$\det(A_I - \lambda \cdot I) = 0 \quad (5-12)$$

For stability the damping of all poles needs to be positive, and thus the real part of the eigenvalues needs to be negative,  $Re(\lambda) < 0$ . From this requirement, the limiting values for  $k_p$  and  $k_I$  can be derived, (5-13).

$$k_p \geq \left. \frac{dQ_{Hydro}}{d\Omega} \right|_{\Omega_0} \quad \forall \Omega_0 \in [0, \Omega_{max}] \quad k_I \geq 0 \quad (5-13)$$

With any  $k_p$  and  $k_I$  fulfilling these given conditions, the inner closed-loop is stable for any input value  $\Omega_{req}$  within operational range.

### 5.2.2.2 Outer Closed-Loop Stability

Extending the procedure from the inner closed-loop to the outer closed-loop, the stability is calculated for the full system in the next step, cf. Fig. 5-4. Initially, the set-point curve transfer function  $G_{Q_{el} \rightarrow \Omega_{req}}$  needs to be determined. The above analysis of the inner closed-loop with a constant input value  $\Omega_{req}$  is equivalent to an infinite slow change in the output value of  $G_{Q_{el} \rightarrow \Omega_{req}}$ , showing stability of the full system in this case. It can therefore be suggested that stability is also given with a finite slow change of  $\Omega_{req}$ , which will be confirmed in the next step. Therefore, the transfer function  $G_{Q_{el} \rightarrow \Omega_{req}}$  is composed here of the



set-point curve introduced in Section 5.2.1 to calculate the momentary optimal rotational speed  $\Omega_{opt}$  and a  $PT_1$ -lowpass filter, (5-14), Fig. 5-5, with the time constant  $T_{PT_1}$ .

$$\dot{\Omega}_{req} = \frac{1}{T_{PT_1}} \cdot (\Omega_{opt} - \Omega_{req}) \quad (5-14)$$

The state vector  $\vec{x}$ , used in the inner-closed loop analysis, does not cover the full system and is therefore replaced with a four parameter state vector  $\vec{z}$ , (5-15), based on the requested,  $\Omega_{req}$ , and current rotational speed,  $\Omega$ .

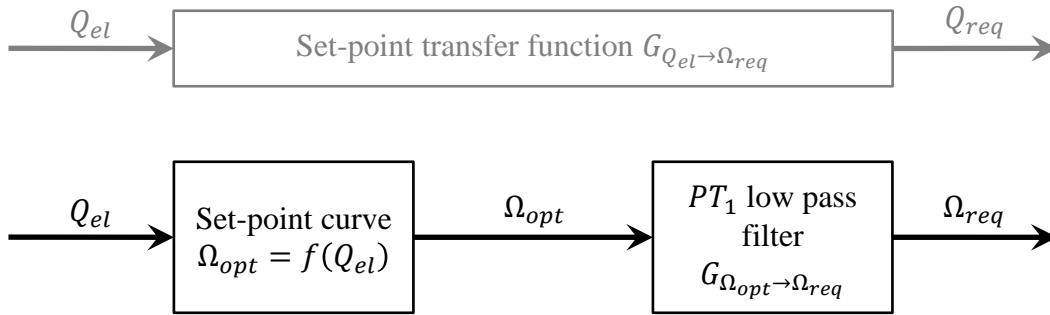


Fig. 5-5: Set point transfer function  $G_{Q_{el} \rightarrow \Omega_{req}}$  resolved

$$\vec{z} = \left[ \int \Omega_{req} dt \quad \Omega_{req} \quad \int \Omega dt \quad \Omega \right]^T \quad (5-15)$$

With this state vector and by linearizing the set-point curve, (5-6), the extended linear set of differential equations  $\dot{\vec{z}} = \mathbf{A}_O \cdot \vec{z} + \vec{b}_O$  for the outer closed-loop can be found, (5-16) ~ (5-17), with the constants  $k_{\Omega Q} = \left. \frac{d\Omega_{opt}}{dQ_{el}} \right|_{\Omega_0}$  and  $k_{Q\Omega} = \left. \frac{dQ_{Hydro}}{d\Omega} \right|_{\Omega_0}$  for the set-point curve slope and the hydrodynamic torque curve slope respectively. The derivation of the equations is shown in Appendix B, p. 149.

$$\mathbf{A}_O = \begin{bmatrix} 0 & 1 & 0 & 0 \\ -\frac{k_I}{T_{PT_1}} \cdot k_{\Omega Q} & -\frac{k_P \cdot k_{\Omega Q} + 1}{T_{PT_1}} & \frac{k_I}{T_{PT_1}} \cdot k_{\Omega Q} & \frac{k_P}{T_{PT_1}} \cdot k_{\Omega Q} \\ 0 & 0 & 0 & 1 \\ \frac{k_I}{J} & \frac{k_P}{J} & -\frac{k_I}{J} & \frac{k_P \cdot k_{Q\Omega}}{J} \end{bmatrix} \quad (5-16)$$

$$\vec{b}_O = \begin{bmatrix} 0 \\ \frac{\Omega_{opt}|_{\Omega_0} + Q_{el}|_{\Omega_0} \cdot k_{\Omega Q}}{T_{PT_1}} \\ 0 \\ \frac{Q_{Hydro}|_{\Omega_0} - \Omega_0 \cdot k_{Q\Omega}}{J} \end{bmatrix} \quad (5-17)$$

The analytical solution for the poles of this set of equations results in extensive formulas, and is thus not feasible for further analysis. Therefore, it is suggested to solve numerically for the pole locations to find the stability limiting value of the  $PT_1$  time constant  $T_{PT_1}$  for each current velocity  $v_1$ . Fig. 5-6 (left) shows an exemplary pole location plot for a representative value of  $v_1$ . As expected, the pole locations converge towards the stable inner closed-loop poles for a rising  $T_{PT_1}$ . For most current speeds the stability limit for the Voith HyTide<sup>®</sup> turbine is at about  $T_{PT_1} \approx 1$  s, Fig. 5-6 (right). However, due to the low value of  $dc_p/d\lambda_{TSR}$  close to the rated point, this value is increased with  $v_1 \approx v_{1rated}$ . For current speeds below rated, the  $PT_1$  filter could be even neglected.

The assumption of a lowpass filter within the set-point curve transfer function, being suitable to achieve stability, was therefore confirmed. With this analysis, the stability of the full system, and thus the feasibility of the underspeed controller are shown.

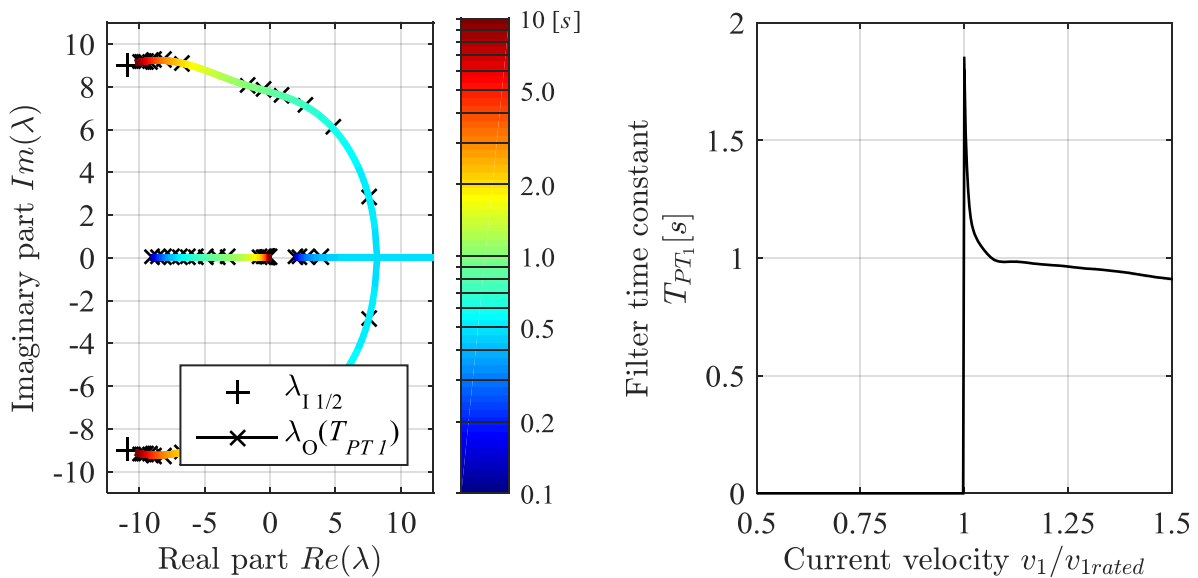


Fig. 5-6: Pole location of  $\mathbf{A}_0$  colored by  $T_{PT_1}$  for an arbitrary above rated point of operation (left) and minimal required value of  $T_{PT_1}$  for stable operation (right)

### 5.2.2.3 Parameter Tuning

The controller parameter  $k_p$ ,  $k_I$  and  $T_{PT_1}$  can be optimized within the calculated ranges to achieve a suitable response behavior to external excitations on the current speed. E.g., a higher value of  $k_I$  would increase the convergence speed, but would also lead to increased power fluctuations as the response of the electrical torque to a disturbance  $\varepsilon \neq 0$  is amplified. Similar, for the  $T_{PT_1}$  parameter a value close to the stability limit would lead to a short but

intense power fluctuation, while a larger value would cause a higher settling time, Fig. 5-7. This value is therefore a trade-off between the turbines reaction time to current velocity changes and spikes in the power, which result on both a voltage fluctuation in the grid, if not mitigated, and temperature fluctuations and thus fatigue in the power electronics.

In the present case of the Voith HyTide<sup>®</sup>1000-13 turbine,  $k_p = 1.1e7$ ,  $k_I = 1e8$  and  $T_{PT_1} = 1.5s$  are suggested. For the inner closed-loop, these values correspond to a natural frequency of  $\omega_{nl} \approx 14.1rad/s$  and a damping ratio of  $\zeta_I \approx 0.77$ , (5-18), chosen based on the recommendations of [39]. For the outer closed-loop this  $T_{PT_1}$  value is a suitable balance of the named issues.

$$\omega_{nl} = \sqrt{\frac{k_I}{J}} \quad \zeta_I = \frac{k_p - \left. \frac{dQ_{Hydro}}{d\Omega} \right|_{\Omega_0}}{2 \cdot \sqrt{k_I \cdot J}} \quad (5-18)$$

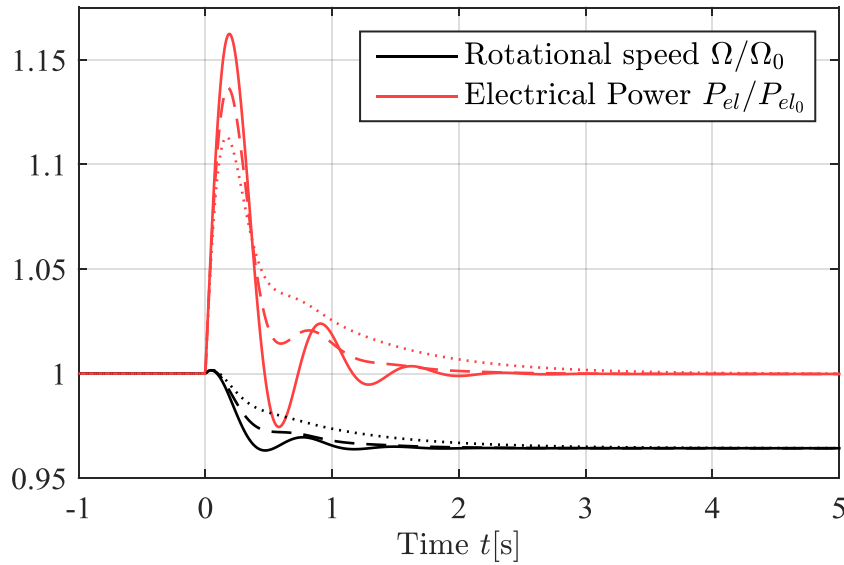


Fig. 5-7: Step response to an current speed increase  $3.5 \rightarrow 3.6 m/s$  at  $t = 0s$  for  $T_{PT_1} = 1.25s$  (solid),  $1.5s$  (dashed) and  $2s$  (dotted)

### 5.2.3 Operational Loads

Based on the controller layout given in the previous sections, the fatigue and ultimate loads are evaluated here in load simulations with turbulent inflow current, and compared to the reference results of the state-of-the-art overspeed controller.

### 5.2.3.1 Simulation Setup

To assess the changes in loads, a simplified method is used here. As discussed in Section 4.3, the main contribution to the dynamics of the turbine results from the tower flexibility. Thus, in the simplified model applied here, only the rotor rotational DoF and the tower fore-aft DoF are taken into account. Therefore, the structural properties of the turbine are reduced to a spring-mass-system. The added mass and rotor hydrodynamics are represented by an actuator point method, applying the loads based on the  $c_p$  and  $c_{th}$  characteristics. The two DoF of the model are therefore coupled by the hydrodynamics as shown in Fig. 5-8 with the current velocity  $v_1$ , rotor speed  $\Omega$ , hydrodynamic thrust  $F_{Hydro}$  and torque  $Q_{Hydro}$  and the tower top velocity  $\Delta\dot{x}$

The system is setup in Matlab Simulink, [48], and the shown subsystem is used to replace the corresponding turbine block in Fig. 5-4. For the input disturbance  $v_1$ , six stochastic current data seeds per current velocity from the TurbSim ‘tidal’-spectrum, [64], are used. To match typical site conditions, the current amplitudes are set to 10% turbulence intensity.

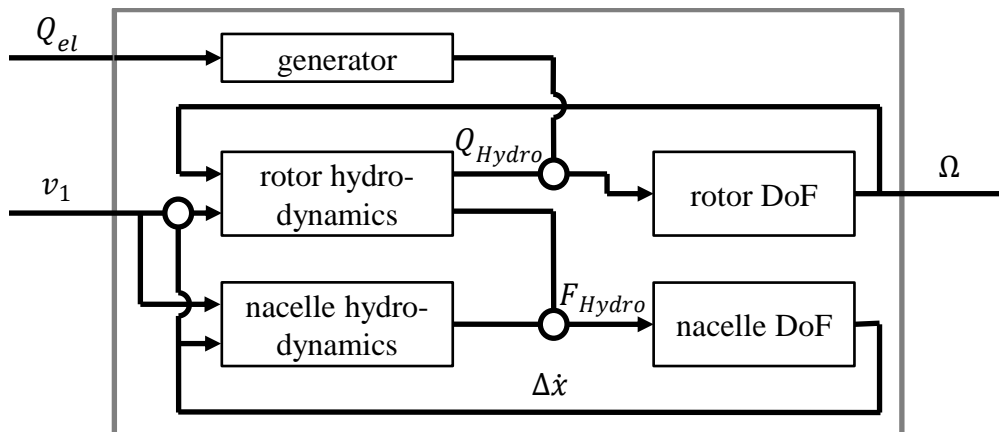


Fig. 5-8: Block diagram of turbine model for controller simulations

### 5.2.3.2 Thrust Loads

The load analysis starts here with the axial hydrodynamic forces,  $F_{Hydro} = F_{thrust} + F_{nacelle}$ , shown in Fig. 5-9. It is clearly visible that the mean, fatigue and ultimate loads are all significantly lower for the underspeed controller. For the mean value, this was the expected result as the steady points of operation feature a lower thrust coefficient compared to the overspeed controller, Section 5.2.1.

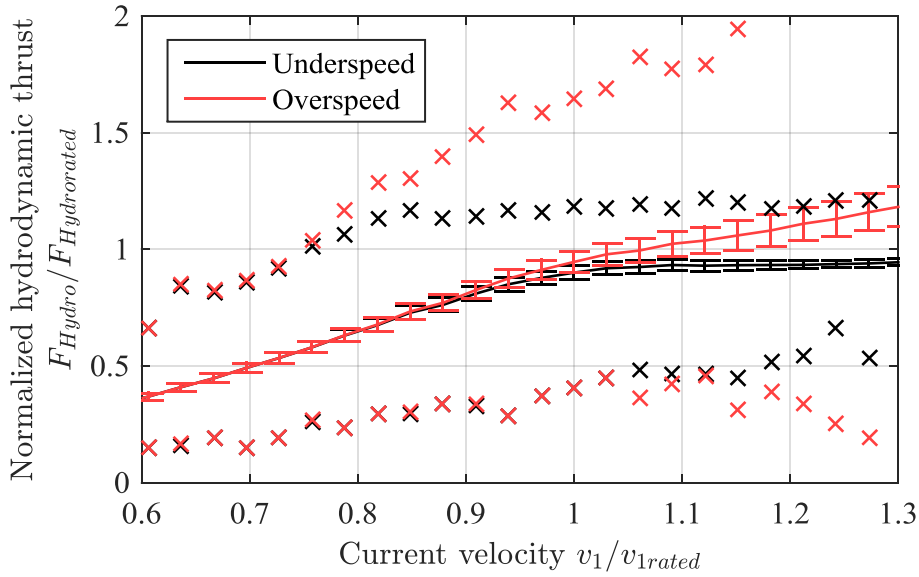


Fig. 5-9: Mean hydrodynamic thrust force  $F_{Hydro}$  (solid) with damage equivalent load  $\pm DEL(F_{Hydro})$  (error bars,  $m = 4$ ,  $N_{ref} = 2e6$ ) and peak loading (x)

For the explanation of the fatigue and ultimate loads, one has to retrieve the discussion of the hydrodynamic damping, Section 5.1.1. The underspeed controller has a larger thrust curve slope  $dc_{th}/d\lambda_{TSR}$ . Thus, in case of a step increase in current velocity the thrust coefficient is reduced stronger compared to overspeed, and the thrust is maintained lower overall. Despite the lower hydrodynamic damping causes on the other hand a higher number of oscillations on the tower motion, the reduction in the excitation outweighs.

This analysis does not consider the tower shadow. The lower rotational speed of the rotor and thus the reduced number of load cycles is therefore not taken into account here. For an operation in tower shadow or non-linear shear, the difference in fatigue damage will therefore be further increased in favor of the underspeed controller.

### 5.2.3.3 Generator Torque and Power Output

On the hydrodynamic torque and electrical power output, Fig. 5-10, the underspeed controller has a lower performance on the mean and ultimate loads. This was expected due to the discussed electrical power peaks required for stable operation, which go up to double the rated power.

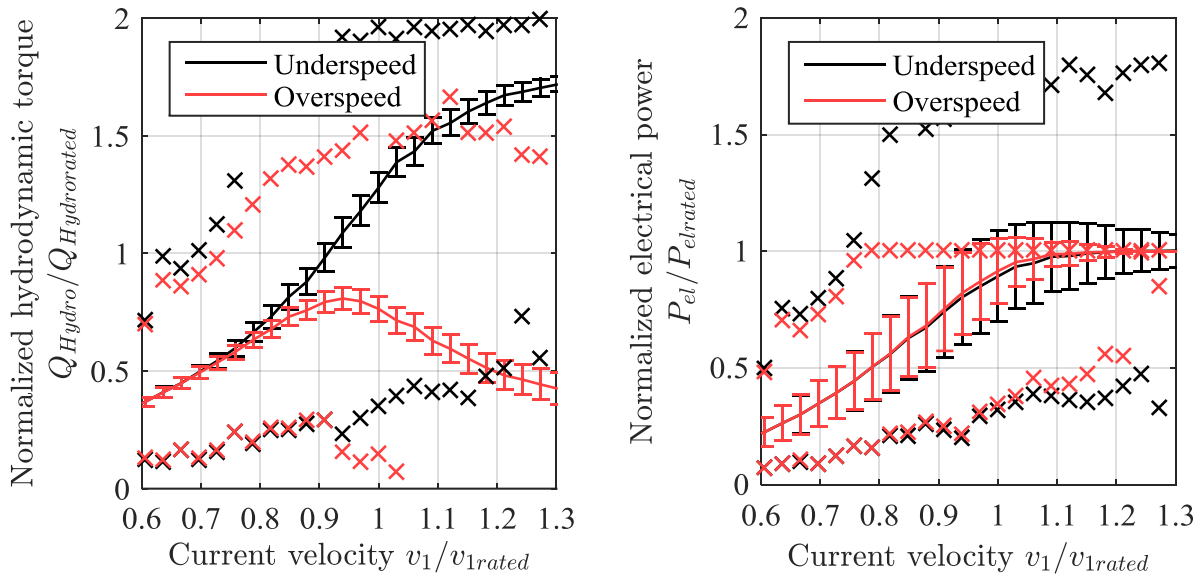


Fig. 5-10: Mean hydrodynamic torque  $Q_{Hydro}$  (left) and mean electrical power  $P_{el}$  (right) with damage equivalent load  $\pm DEL(Q_{Hydro})$  (error bars,  $m = 4$ ,  $N_{ref} = 2e6$ ) resp. standard deviation  $\pm \sigma(P_{el})$  and peak loading (x)

However, it is interesting that the underspeed controller has a lower fatigue load on the hydrodynamic torque  $DEL(Q_{Hydro})$  for high current speeds. The reason for this can be found in the high fluctuations in rotational speed for the overspeed case, which also leads to high fluctuations in the torque. In comparison, the rotational speed for the underspeed turbine is rather constant.

#### 5.2.4 Performance Evaluation of the Underspeed Controller

The comparison of the performance of the underspeed with the baseline overspeed controller shows that the suggested strategy has the potential for reducing the loads on the turbine significantly. Comparing this load reduction to a pitch controller, as introduced by the ‘load reduction concept’ in Section 2.2.3, opens further potential on the generator torque and power output as shown in publication [A 5]. However, this comes on the cost of leaving the ‘robustness concept’ with the risk of increased down times.

Overspeed, underspeed and pitch controllers are therefore three options to deal with the apparent, unavoidable load fluctuations, due to turbulent inflow. Each of those controllers transmits this load to a different part of the turbine system, Fig. 5-11. While the overspeed controller causes high structural loads with lower stress on the electrical components and the actuators, the underspeed controller reduces the structural loads on the cost of the electrical

components. The pitch controller reduces the loads for both, the structural and electrical components, but increases the loads on additionally required pitch actuators. None of the loads can therefore be reduced without increasing the loads for the others. The controller type is subsequently a strategic decision with a high number of variables.

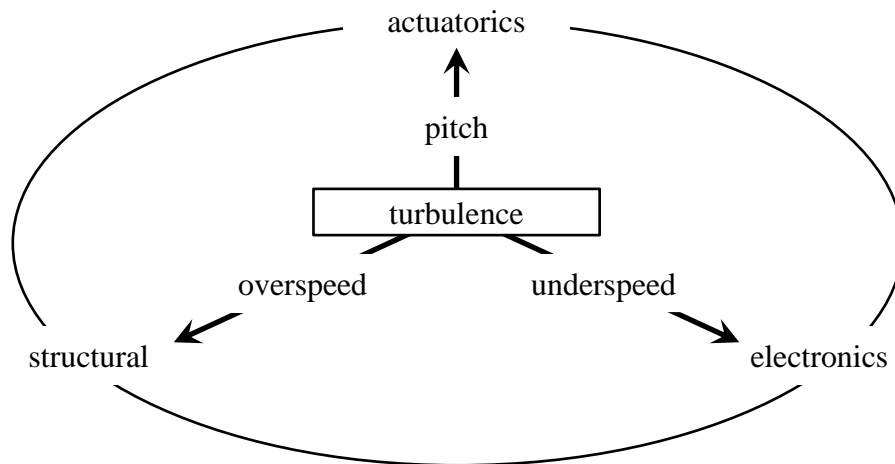


Fig. 5-11: Divisions responsible to deal with turbulence based on the controller concept

A first indication for the optimal strategy can be given by analyzing the masses of the system. On the electrical side, the generator torque is approximately proportional to the generator volume and mass,  $m_{el} \sim Q_{el}$ . On the structural side, assuming quadratic solid beam structures, the mass can be approximate to be  $m_{struct} \sim F^{2/3}$ . Based on the comparison of the ultimate loads, the mass reduction of the system, upon a change from the overspeed concept to the underspeed concept, can be drawn for different mass ratios of electrical and structural components, Fig. 5-12. As can be seen, the higher the structural mass portion of the turbine is, the higher is the potential for mass reductions.

The cost reduction correlates non-linearly to the mass reduction. This conceptual change therefore makes no sense in case of a relatively large or expensive electrical system. It is also difficult to distinguish between electrical or rotating and structural masses for, e.g., the main shaft, and the approximation is only a rough estimation of the possible gain. For the here investigated Voith HyTide<sup>®</sup>1000-13 turbine the mass distribution is approx. 71% of the total system mass on the structural mass and 29% on the rotating mass. This mass distribution leads, based on the above described estimation, to a system mass change of  $\Delta m \approx -13\%$ , which might be further improved with an adapted re-design of the turbine. Further, the very large reduction in fatigue load is not considered in this estimation giving additional potential for cost reduction on the live time analysis.

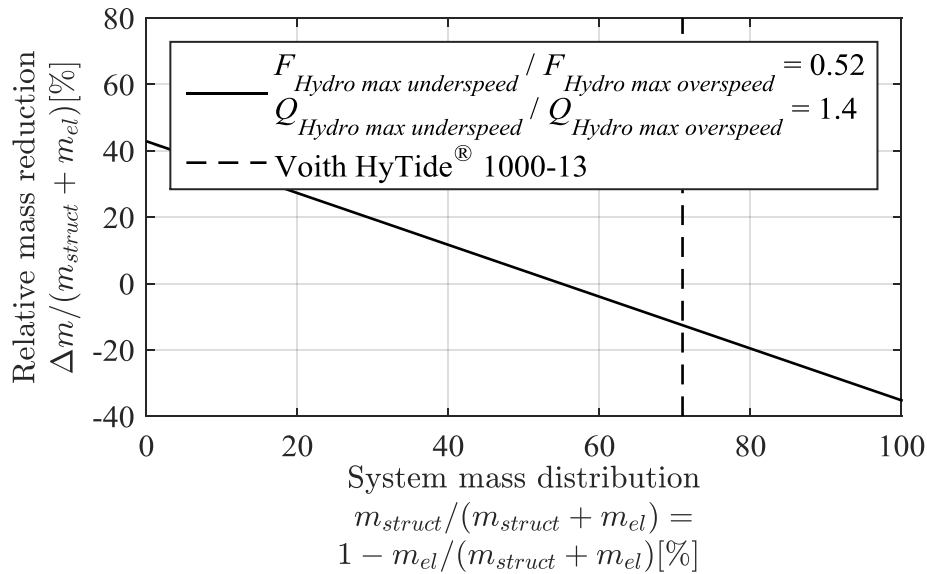


Fig. 5-12: Mass reduction due to change in controller concept from overspeed to underspeed dependent on mass fraction of system and changes in ultimate loads

### 5.3. Hydroelastic Behavior with the Underspeed Controller

The observed load reductions on the underspeed controller, cf. Section 5.2.3, are based on the major assumption of quasi-steady rotor hydrodynamics. This assumption is flawed, due to two issues. The first issue is the inertia of the flow and the dynamic inflow effect, [69]. This effect will lead to increased peaks in the rotor loads and needs to be taken into account for design load simulations. However, in the present comparison it can be neglected, as it applies to both, overspeed and underspeed, in the same way.

The second issue, which will be further investigated here, is of higher importance and leads back to the analysis of the hydroelasticity. Stall is a transient and stochastic phenomenon and may cause broad-band frequency excitations to the blades. Subsequently, the rotor blades are subject to variations in loads, which might lead to vibrations on the complete turbine structure.

The stall behavior depends on the stall regime, Fig. 5-13. While partial or trailing edge stall is often a more stable condition, leading edge stall or full stall causes a more unsteady and stochastic flow, [19]. Further increasing the angle of attack causes the stall vortices to break down and start low frequency shedding from the airfoil surface. This state of shedding vortices is called deep stall. Depending on the geometry, this shedding might result in an



unstable and unsteady but deterministic vortex street as e.g. the Kármán vortex street on a cylinder.

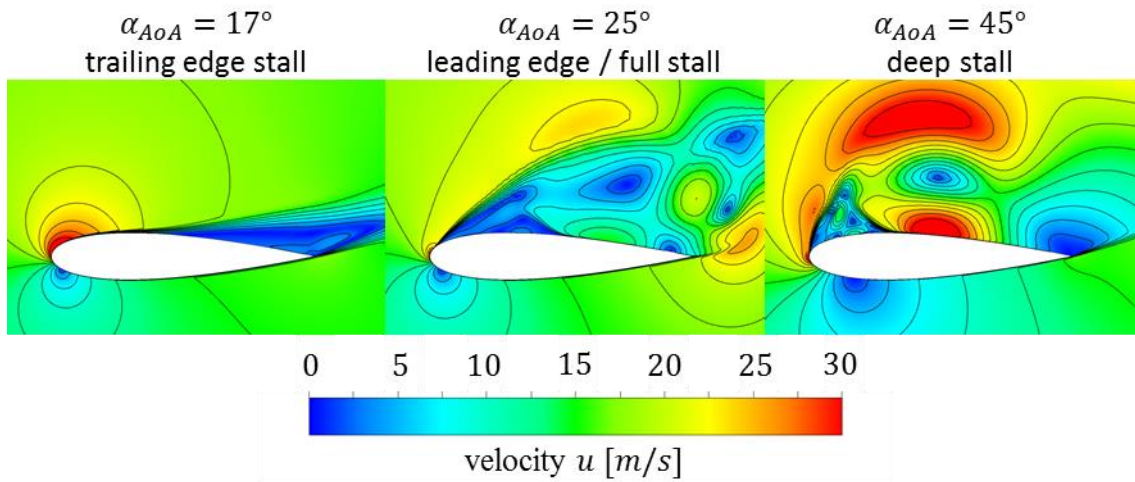


Fig. 5-13: Simulation of partial stall (left), full stall (middle) and deep stall (right) for NACA0018 airfoil with  $Re = 1e6$  in air and SAS turbulence model

The different radial positions along the rotor blade are subject to a combination of those stall patterns, dependent on the tip speed ratio. Therefore, the different modes of the rotor blade are excited on varying intensities and combine to the full response behavior. Below, this behavior in stall operation will be analyzed in case of a rigid structure and with hydroelasticity considered.

### 5.3.1 Simulation Setup

The simulation model for the stall investigations is setup as an adapted version of the model introduced in Section 4.1. The investigation is limited here to the rotor blade performance under constant inflow condition, and thus only a single blade is simulated. However, while the above model was optimized for the simulation of attached flow conditions, for stall simulations a higher grid resolution is required. Therefore, the model has been extended by a grid refinement to ca.  $4 \cdot 10^6$  hexahedral elements in the blade vicinity. Further, the turbulence model has been replaced by the SAS model, which is more suitable for stall simulation than the classic SST model, [53].

### 5.3.2 Hydroelasticity in Stall

As outlined initially the stall patterns depend on the radial position along the blade. Fig. 5-14 shows this behavior for three tip speed ratios. While for  $0.75 \cdot \lambda_{TSR\ opt}$  only minor and steady

trailing edge stall regions occur, the outer part of the rotor blade is for  $\lambda_{TSR\ opt}/2$  in full stall. However, on this point of operation with  $\lambda_{TSR\ opt}/2$  the flow on the inner most part of the blade is still attached. For  $\lambda_{TSR\ opt}/4$  the stall extends to the hub. Among those points of operation, a different stall load is to be expected. While the operation at  $0.75 \cdot \lambda_{TSR\ opt}$  combines a steady vortex structure with a high hydrodynamic damping, load fluctuations coincide with a low hydrodynamic damping especially with  $\lambda_{TSR\ opt}/2$ .

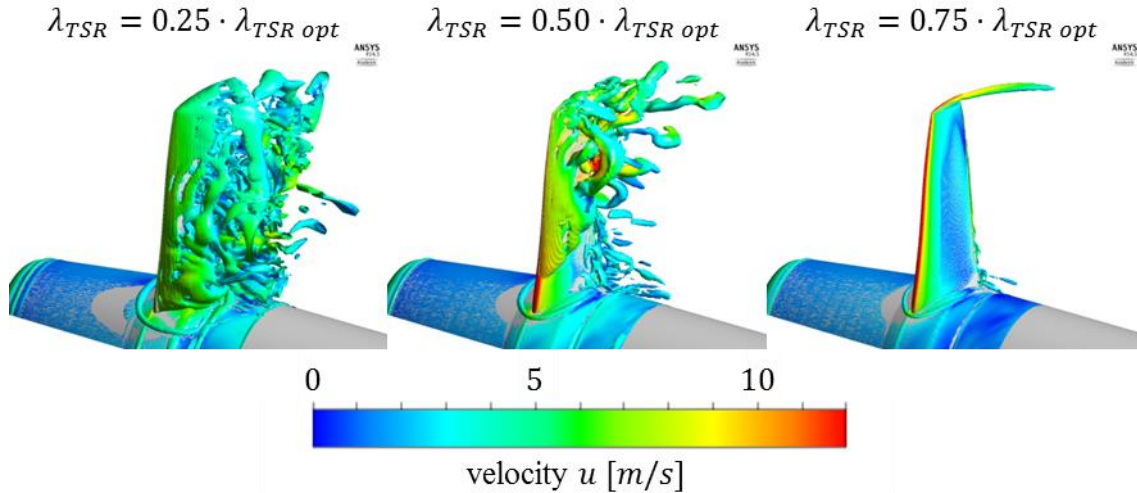


Fig. 5-14: Iso-view on vortex structures on suction side of rotor blade during underspeed operation

This behavior is also shown in Fig. 5-15 for the blade tip motion of the three investigated points of operation. The hydroelastic simulation starts here with the fully onset stall system of a rigid simulation, and activates the blades flexibility then. The resulting free decay to the fully onset hydroelastic stochastics is subject to the individual hydrodynamic damping. For comparison the point of operation in the overspeed region,  $\lambda_{TSR} = 2 \cdot \lambda_{TSR\ opt}$ , which has been investigated above in Section 4.3, is added and has a high hydrodynamic damping ratio. As can be seen, besides the different amplitude of the resulting motion, the cases form two groups. While the thrust coefficient and thus the tip deflection converges to a steady value for  $0.75 \cdot \lambda_{TSR\ opt}$  and  $2 \cdot \lambda_{TSR\ opt}$ , the blade tip remain in motion for the other two. This correlates to the above given discussion of the stall regimes and their stochastic loads.

The impact of the elasticity is further shown for  $\lambda_{TSR\ opt}/2$  in Fig. 5-16 with a time and frequency domain analysis of the blade root loads in comparison of a rigid and a hydroelastic blade. Despite both cases started from the identical initial case, the hydrodynamic loads change differently over time between the two cases. This is a result of the onset of the elastic

motion. However, it indicates also the stochastic nature of stall. Similar to the investigation results for the full turbine shown previously, the flexibility of the rotor blade has a minor impact on the results. The here shown thrust force coefficient at the blade root  $c_{th\ root}$  has the approximately same mean value and standard deviation in both cases.

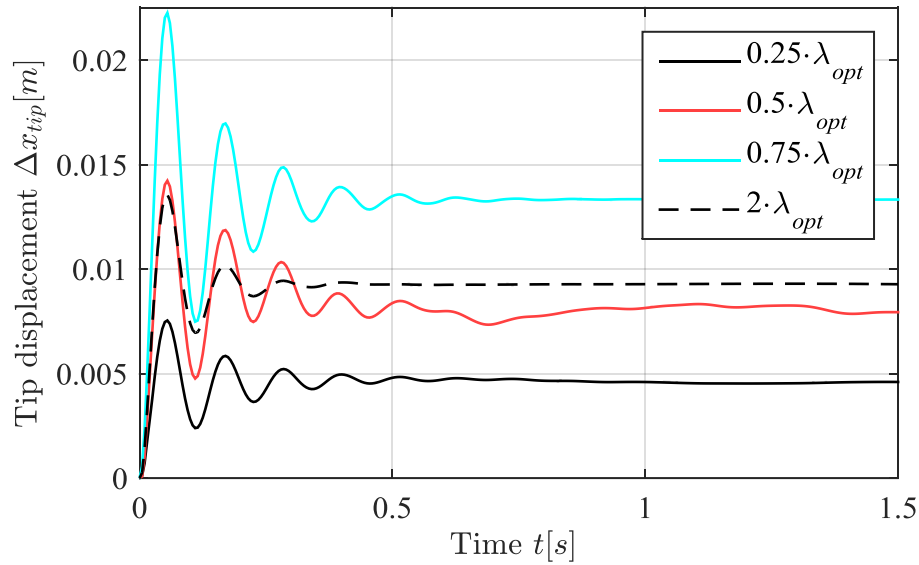


Fig. 5-15: Blade tip displacement  $\Delta x_{tip}$  for  $v_1 = 4\text{ m/s}$  at different tip speed ratios  $\lambda_{TSR}$

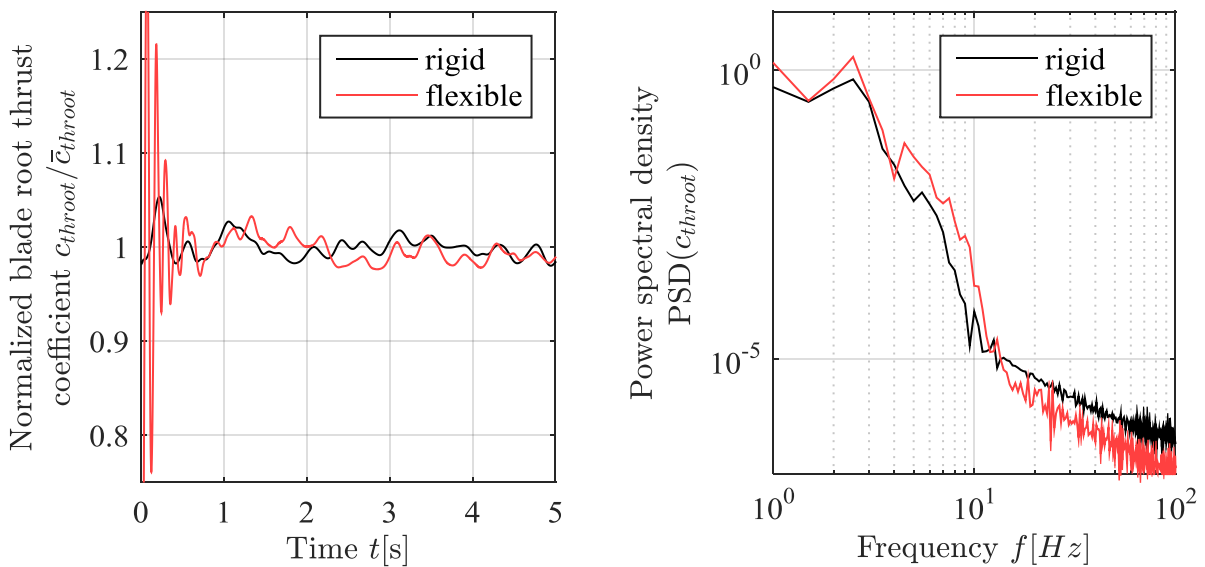


Fig. 5-16: Time series (left) and spectrum (right, later 4s) of blade root thrust force coefficient  $c_{th\ root}$  for  $v_1 = 4\text{ m/s}$  and  $\lambda_{TSR} = \lambda_{TSR\ opt}/2$

Analyzing the frequency domain, a distinct difference can be identified. The flexibility of the rotor blade increases the power spectral density (PSD) on the frequencies close to the blade's

eigenfrequency just below 10Hz. For smaller frequencies the PSD converges between the cases, while for higher frequencies the load is reduced by the flexibility, cf. Section 5.1.

Nevertheless, on none of the frequencies and points of operation investigated here a negative damping or low speed flutter occurred. Also the observed load amplitude due to stall is quite small and at least one order of magnitude smaller than the load variations due to the turbulent inflow and tower wake operation. Therefore, the issue of stall causing additional fatigue loads in underspeed operation can be confirmed to exist by the observed load oscillations in Fig. 5-16, but is shown to be acceptable small in comparison to the gained performance increase presented above.

#### **5.4. Discussion of the Conceptual Strategy**

Within this chapter, different approaches to improve the conceptual strategy for the Voith HyTide<sup>®</sup> turbine have been analyzed. These can be grouped into four design advices listed below:

1. Change the controller strategy to an underspeed operation: The central issue with fatigue, high loads and resonance occurs due to high rotational speeds. These can be avoided by changing the controller strategy towards operation in stall with increased hydrofoil drag coefficients to limit the power, and with significantly reduced loads. The additional loads from stochastic stall vibrations are acceptable small.
2. Reduce the tower wake: The main impact on the magnitude of the tower wake is the shape of the transition piece. Heading for an elliptical structure here would significantly reduce the load variations in downstream operation.
3. Avoid design flaws: Namely, designing the eigenfrequencies to be in resonance with any point operation should be avoided. Obviously, this has already been done as far as possible, but it is listed here, as it needs to be kept in mind on any other system changes.
4. Manage the hydrodynamic damping: For this value, a balance needs to be found between a too low value, causing an excessive number of oscillations, and a too high value, which would lead to high excitations in unsteady and inhomogeneous environments. This balance can be influenced mainly by the rotor blade design.

---

## 6. CONCLUSIONS

Within this research, a simulation method for the hydroelastic response and fluid-structure-interaction of tidal current turbines has been developed. This toolchain is applied to the Voith HyTide<sup>®</sup>1000-13 turbine to identify the key components, which are relevant for the hydroelastic response, and reveal their effect and optimization potential.

### 6.1. Summary

Tidal current energy offers the unique possibility of a reliable and long-term predictable renewable energy source. The present thesis started with an analysis of this resource and showed the complexity of the technology. Compared to wind turbines, despite the same technological approach being used, the tidal current turbine differs strongly from a wind turbine in its geometries and conceptual approaches. Regardless, many assumptions for the design of the systems are transferred between the technologies. The present research challenges one of those assumptions, which states that the fluid-structure-interaction is dominated by the rotor blades and the tower, and evaluates the influence of the different components on the turbine's hydroelastic response. This is carried out with simulations of the Voith HyTide<sup>®</sup>1000-13 tidal current turbine, a turbine conceptually designed to maximize the reliability.

The initial research focuses on analyzing the available tools for the simulation of tidal current turbines, which proved to be unsuitable for the present application. The optimal toolchain is identified to be a combination of CFD and multibody-methods, as these offer a balance of level of detail, flexibility and required resources suitable for the investigations. Following this evaluation, a fluid-multibody-interaction method (FMBI) is developed based on the commercial tools Ansys CFX and Simpack. Compared to the FSI methods based on CFD and FEM the FMBI approach breaks down the communication to a discrete number of locations instead of surface coupling. From these discrete locations, the corresponding surface values are interpolated with transformation splines. This increased the efficiency of the method, however limits its application to beam-like objects, e.g. tower and rotor blades of a tidal current turbine. Surface buckling for example can not be simulated.

The next step of the present research is the validation of the FMBI. This was not performed with the usually used model validation approach, but with a code validation methodology. In

comparison to the model validation approach, the code validation concludes bottom-up from the validity of each tool within the toolchain to the validity of the toolchain, instead of the top-down direction of the model validation, leading to small, affordable and specific validation experiments. The comparison of the results confirmed the validity of the toolchain. However, for the application of the tidal current turbine, the required site-measured data to validate the tower shadow in the CFD model is not available. Therefore, the computed load amplitudes within the present research should only be compared to each other, and shall not be taken as absolute values, as the tower shadow is not validated in detail here.

By simulating the rotor-foundation-interaction of the tidal current turbine first in a rigid setup, the vortex structures and loads on the tidal turbine are analyzed. From these results, a deterministic load case with a high current speed and a tip speed ratio close to the run-away condition is identified to be most relevant for the hydroelastic investigations. Therefore, this single point of operation is simulated in a large variety of combinations of component flexibilities to identify the load driving components, which have the largest impact on the changes in loads due to their hydroelastic response. This investigation shows that the drivetrain's flexibilities of the shaft, rotor blades, etc. have a minor influence on the loads, while the fixed-structure's flexibilities of foundation, tower, nacelle, etc. dominate the hydroelasticity. The tower and the nacelle nodding flexibility were found to be of particular relevance. The rotor blades, which are of high importance for wind turbines and are often investigated in literature for tidal current turbines, did not show a significant impact for the Voith HyTide<sup>®</sup> turbine, due to the rather high eigenfrequencies of the rotor blades in this design.

The investigation covers also further resonance points of operation in the tower fore-aft eigenfrequency. These simulations show the severeness of the deterministic resonance event with e.g. the tower bottom bending load amplitude increasing by a factor of five. However, this was observed to be only a local load increase, as at the very same point of operation, the load amplitude of the axial hub force only changes marginally. Furthermore, a transient riding-through of the point of resonance within 2s was simulated. This limitation of the duration of resonance reduces the load amplitude increase of the tower bottom bending moment to a factor of four. This shows that the operation in the resonance region requires detailed investigations to evaluate the loads and these points of operation should be, if possible, avoided.

---

Based on the results of the hydroelastic simulations and an analysis of the potential of different conceptual design strategies, two central recommendations for the Voith HyTide<sup>®</sup> turbine were concluded: Building the system stiff to avoid resonance frequency excitations, and changing the current overspeed controller to an underspeed controller. While the state-of-the-art overspeed controller limits the power production by increasing the tip speed ratio, the underspeed controller drives the turbine into a controlled state of stall. This results in significantly lower ultimate and fatigue loads at the same mean power output. However, the generator torque has a higher mean value and a higher fluctuation. Based on the ultimate loads on the system, a rough estimation of the system mass shows a reduction of about 13% compared to the overspeed system.

The present research concludes with connecting the investigation of the underspeed controller to the hydroelastic simulations. Additional hydroelastic simulations in the stall conditions showed that the load variations and vibrations due to stall are small for a tidal current turbine compared to the gained load reduction from underspeed controlled operation.

Overall, the present research introduces an effective method to simulate the hydroelastic response of a tidal current turbine and the method has been applied exemplarily to the Voith HyTide<sup>®</sup> turbine. The results of these simulations are used to identify the tower and nacelle to be the load driving components when considering the hydroelastic response. The research concludes with an evaluation of the future potential of the turbine concept.

## **6.2. Future Work and Recommendations**

The most urgent step in future work on this topic is the validation of the tower shadow. This can be done with either lab experiments or field measurements, which were both beyond the scope of the present project. Based on this reference data, the absolute scale of the load and motion amplitudes can then be evaluated, increasing the fidelity to the results.

From an analysis point of view, the present thesis leaves one question unanswered – how do the results on the hydroelasticity change, when not only deterministic but also stochastic, turbulent inflow conditions are considered? To answer this, the simulation study of Section 4 needs to be re-run with turbulent inflow. However, this would consume massive amounts of computational resources, as the required spatial and temporal resolution will increase to prevent numerical damping of the incoming turbulence. The simulated time duration would also need to be extended to achieve convergence of the loads' statistical parameters. The

complexity further increases considering that, operating under stochastic inflow, the variable speed controller changes also the rotor speed. This is beyond the scope of the present research, but makes sense to be investigated in the future with the tools developed here.

The second recommendation requiring further work is to develop the turbine concept towards an underspeed controlled system. Despite the fact that stall causes minor high frequency vibrations, the possible performance increase of the system regarding ultimate and fatigue loading is significant and offers the possibility to reduce the system mass. As a first step this controller concept should be brought to lab tests based on the analytical proof-of-concept given here. The second step would then be to bring it into the turbulent stochastic environment of prototype testing. This could also be done at a down-rated point of operation on existing overspeed prototypes. Based on the shown results, the underspeed control approach can be a highly competitive conceptual decision for future fixed-pitch tidal current turbines.

### **6.3. Concluding Remarks**

Tidal current energy is, despite the great advances over the last years, still a very young approach to renewable energy. Research is driving this technology forward, but the economic breakthrough is still missing because of the demand for proof of viability. Here the risk of the research giants, supersized projects beyond the current technological possibilities, which nearly destroyed the wind energy technologies in their early years, still exists. Therefore, the final recommendation goes to all who are working in the tidal energy sector: Get the tidal current energy to the market quickly, but do not overdo it. Bring tidal current turbines into the water at as many sites as possible, in order to understand the technologies under different conditions, but do not head for the  $1GW$  till the  $100MW$  is fully understood and do not head for the  $100MW$  before the  $10MW$  is fully understood. A single, large-scale failure might still destroy the faith in this technology from the customers' point of view. So, do one step at a time and do not risk that one fatal mistake.



---

## REFERENCES

- [1] Allmark, M., Prickett, P., Grosvenor, R., Frost, C. (2015), "Time-Frequency Analysis of TST Drive Shaft Torque for TST Blade Fault Diagnosis", 11<sup>th</sup> European Wave and Tidal Energy Conference, EWTEC 2015, Nantes, France
- [2] Altair HyperWorks (2015), "AcuSolve", Böblingen, Germany
- [3] Atlantis Resources Ltd. (2016), website: <http://atlantisresourcesltd.com>
- [4] Alscher, S. (2011), "Validierung der strömungsmechanischen Simulation eines Gezeitenströmungsrotors mit experimentellen Modellversuchen", Diploma thesis, University Stuttgart, Germany
- [5] Ansys Inc. (2015), "Ansys CFD User Manual", Canonsburg, USA
- [6] Ansys Inc. (2015), "AQWA User Manual", Canonsburg, USA
- [7] Arnold, J., Krüger, W., Einarsson, G. (2010), "Coupling of MBS and CFD: an Oscillating Aeroelastic Wing Model", Simpack News September 2010, pp. 22-24
- [8] Atherton, T., Kerbyson, D. (1999), "Size invariant circle detection", Journal of Image and Vision Computing, Vol. 17, No. 11, pp. 795-803
- [9] Avitabile, P. (2006), "Model Reduction Techniques", University of Massachusetts Lowell, USA
- [10] Bachmann, H., et.al. (1995), "Vibration Problems in Structures", ISBN 978-3-0348-9955-0
- [11] Batten, W., Bahaj, A., Molland, A., Chaplin, J. (2008), "The prediction of the hydrodynamic performance of marine current turbines", Journal of Renewable Energy, Vol. 33, pp. 1085-1096
- [12] Betz, A. (1926), "Wind-Energie und ihre Ausnutzung durch Windmühlen", Vandenhoeck & Ruprecht, Göttingen, Germany
- [13] Beyer, F., Arnold, M., Cheng, P.W. (2013), "Analysis of Floating Offshore Wind Turbine Hydrodynamics Using Coupled CFD and Multibody Methods", 23<sup>rd</sup> International Ocean and Polar Engineering Conference, ISOPE 2013, Anchorage, USA
- [14] Biskup, F., Daus, P., Arlitt, R. (2011), "Auslegung und Evaluierung eines Rotordesigns für Gezeitenströmungsanlagen", 34<sup>th</sup> Dresdner Wasserbaukolloquium, Germany, ISBN 978-3-86780-198-0
- [15] Bittencourt, C., Zarraonandia, G., Vinogradov, A., Cocho, M. (2014), "The first Standard for Certification of Horizontal Axis Tidal Turbine (HATT): The Application of Risk Based Approach", 33<sup>rd</sup> International Conference on Ocean, Offshore and Arctic Engineering, OMAE 2014, San Francisco, USA
- [16] Blevins, R. (1979), "Formulas for natural frequency and mode shape", ISBN 0-442-20710-7, Van Nostrand Reinhold Company, USA

- 
- [17] Bluewater (2016), website: <http://www.bluewater.com>
- [18] Boussinesq, J. (1877), “Essai sur la théorie des eaux courantes”, Mémoires présentés par divers savants à l’Académie des Sciences, Paris, France
- [19] Broeren, A., Bragg, M. (2011), “Spanwise Variation in the Unsteady Stalling Flowfields of Two-Dimensional Airfoil models”, AIAA Journal, Vol. 21, No.4, pp. 1067-1078
- [20] Bundesamt für Seeschifffahrt und Hydrographie (BSH), Bundesministerium für Wirtschaft und Energie (BMWi), Projektträger Jülich (PTJ) (2015), research project FINO, website: [www.bsh.de/en/Marine\\_data/Projects/FINO](http://www.bsh.de/en/Marine_data/Projects/FINO)
- [21] Burton, T., Sharpe, D., Jenkins, N., Bossanyi, E. (2011), “Wind Energy Handbook, 2<sup>nd</sup> Edition”, ISBN 978-0-470-69975-1, John Wiley & Sons, England
- [22] Cheng, P.W. (2015), “Entwurf von Windenergieanlagen I”, Lecture script, University Stuttgart, Germany
- [23] Cordes, U., Kampers, G. (2015), “Gust Load Alleviation through Enhanced Fluid-Structure Interaction“, 11<sup>th</sup> EAWE PhD Seminar on Wind Energy in Europe, Stuttgart, Germany
- [24] Deruntz, J., Geers, T. (1978), “Added Mass Computation by the Boundary Integral Method“, International Journal for Numerical Methods in Engineering, Vol. 12, pp. 531-549
- [25] Dietz, S. (2013), “SIMBEAM Reloaded“, Simpack News, July 2013, pp. 32-35
- [26] Dietz, S., Knothe, K. (1997), “Reduktion der Anzahl der Freiheitsgrade in Finite-Element-Substrukturen“, ILR-Mitteilungen, Vol. 315, Technische Universität Berlin, Germany
- [27] DLR (2015), “FLOWer User Handbook“, Braunschweig, Germany
- [28] European Marine Energy Centre (EMEC) Ltd. (2015), website: [www.emec.org.uk](http://www.emec.org.uk)
- [29] Fischer, A. (2012), “Untersuchung der Rotorblatt-Modellierungstiefe auf das dynamische Verhalten einer modernen 5MW-Windenergieanlage“, Diploma thesis, University Stuttgart, Germany
- [30] Fischer, T. (2012), “Mitigation of Aerodynamic and Hydrodynamic Induced Loads of Offshore Wind Turbines“, PhD-Thesis, University Stuttgart, Germany, ISBN 978-3-84401501-0
- [31] Förster, C., Wall, W., Ramm, E. (2006), “The Artificial Added Mass Effect in Sequential Staggered Fluid-Structure Interaction Algorithms“, ECCOMAS CFD, Delft, Netherlands
- [32] Faudot, C., Dahlhaug, O., Holst, M. (2013), “Tidal turbine blades in runaway situation: experimental and numerical approaches“, 10<sup>th</sup> European Wave and Tidal Energy Conference, EWTEC 2013, Aalborg, Denmark

- 
- [33] Garrad Hassan & Partners Ltd. (2013), “Tidal Bladed V4.4 – Theory Manual“, Bristol, England
- [34] Gasch, R., Twele, J. (2007), “Windkraftanlagen – Grundlagen, Entwurf, Planung und Betrieb“, ISBN 978-3-8351-0136-4, Teubner, Germany
- [35] Gracie, K., Nevalainen, T., Johnstone, C., Murray, R., Doman, D., Pegg, M. (2015), “Development of a blade design methodology for overspeed power-regulated tidal turbines”, 11<sup>th</sup> European Wave and Tidal Energy Conference, EWTEC 2015, Nantes, France
- [36] Hauptmann, S., Mulski, S., Cosack, N., Kühn, M., Mauer, L. (2006), “Aero-elastic Simulation of a Wind Turbine and Drive Train Resonance Analysis Using the Multi-Body Simulation Code Simpack“, DEWEK 2006, Bremen, Germany
- [37] Hauptmann, S., Matha, D., Hecquet, T. (2010), “Aeroelastic Load Simulations and Aerodynamic and Structural Modeling Effects“, Simpack Conference: Wind and Drivetrain, Hamburg, Germany
- [38] Jo, C.-H., Kim, D.-Y., Rho, Y.-H., Lee, K.-H., Johnstone, C. (2013), “FSI analysis of deformation along offshore pile structure for tidal current power“, Journal of Renewable Energy, Vol. 54, pp. 248-252
- [39] Jonkman, J. (2007), “Dynamics Modeling and Loads Analysis of an Offshore Floating Wind Turbine“, NREL/TP-500-41958, PhD-thesis, NREL, USA
- [40] Jonkman, J., Buhl Jr., M. (2005), “FAST User’s Guide“, NREL/EL-500-29798, Colorado, USA
- [41] Kaufer, D., Cheng, P.W. (2014), “Validation of an Integrated Simulation Method with High-Resolution Load Measurements of the Offshore Wind Turbine Repower 5M at AlphaVentus“, Journal of Ocean and Wind Energy, Vol. 1, No. 1, pp. 30-40
- [42] Kim, B.-S., Bae, S.-Y., Kim, M.-K., Kim, W.-J., Lee, S.-L. (2012), “Performance Prediction and Structural Integrity Assessment of 50-kW Tidal Turbine Using Unidirectional FSI Method“, 22<sup>nd</sup> ISOPE 2012, Rhodes, Greece
- [43] Kreuzwirth, G., Resch, T. (2012), “Rotor Dynamic and Bearing Analysis of an Instream Tidal Energy Converter“, AVL internal report CC0494
- [44] Lemmer, F., Amann, F., Azcona, J., Munduate, X., Bottaso, C.L., Campagnolo, F., Bredmose, H., Manjock, A., Pereira, R., Robertson, A. (2016), “Model Building and Scaled Testing of 5MW and 10MW Semi-Submersible Floating Wind Turbines“, 13<sup>th</sup> EERA DeepWind’2016, Trondheim, Norway
- [45] Lenz, D. (2014), “Untersuchung instationärer aerodynamischer Effekte an Windenergieanlagen mittels Free Vortex Methoden“, BSc-Thesis, University Stuttgart, Germany
- [46] Lienhart, H., Gomes, J. (2006), “Experimental Study on a Two-Dimensional Fluid-Structure Interaction Reference Test Case“, European Conference on Computational Fluid Dynamics, ECCOMAS CFD, Delft, Netherlands

- [47] Matha, D., Hauptmann, S., Hecquet, T., Kühn, M. (2010), "Methodology and Results of Loads Analysis of Wind Turbines with Advanced Aeroelastic Multi-Body Simulation", DEWEK 2010, Bremen, Germany
- [48] MathWorks Inc. (2015), "Matlab - Simulink", website: [www.mathworks.com](http://www.mathworks.com)
- [49] Marine Energy Matters Ltd. (2015), "Marine Energy – Global Technology Review 2015", annual review, Newton Abbot, England
- [50] Marine Renewables Canada (2013), "Marine Renewable Energy in Canada & in the Global Context – State of the Sector Report - 2013", website: [www.marinerenewables.ca](http://www.marinerenewables.ca), Canada
- [51] McCann, G., Rawlinson-Smith, R., Argyriadis, K. (2006), "Load Simulation for Tidal Turbines using Wind Turbine Experience", International Conference on Ocean Energy, ICOE 2006, Bremerhaven, Germany
- [52] Menter, F. (1993), "Zonal Two Equation  $k-\omega$  Turbulence Models for Aerodynamic Flows", 23<sup>rd</sup> Fluid Dynamics, Plasmadynamics, and Lasers Conference, Orlando, USA
- [53] Menter, F., Egorov, Y. (2010), "The Scale-Adaptive Simulation Method for Unsteady Turbulent Flow Predictions. Part 1: Theory and Model Description", Journal of Flow, Turbulence and Combustion, Vol. 85, No. 1, pp. 113-138
- [54] Meister, K. (2015), "Numerische Untersuchung zum aerodynamischen und aeroelastischen Verhalten einer Windenergieanlage bei turbulenter atmosphärischer Zuströmung", PhD-Thesis, University Stuttgart, Germany
- [55] Mok, D. (2001), "Partitionierte Lösungsansätze in der Strukturdynamik und der Fluid-Struktur-Interaktion", PhD-Thesis, University Stuttgart, Germany
- [56] Morison, J. R., O'Brien, M. P., Johnson, J. W., Schaaf, S. A. (1950), "The force exerted by surface waves on piles", Journal of Petroleum Technology, Vol. 2, No. 5, pp. 149-154
- [57] Morris, C. (2014), "Influence of Solidity on the Performance, Swirl Characteristics, Wake Recovery and Blade Deflection of a Horizontal Axis Tidal Turbine", PhD-thesis, Cardiff University, England
- [58] Müller, A.v., Daus, P., Schwarz, P., Jeschke, P. (2011), "Characterization of the Turbulent Flow Field at a Site for Tidal Turbine Installation Based on Acoustic Doppler Current Profiler Measurements", Diploma thesis, RWTH Aachen, Germany
- [59] Munz, C.-D., Westermann, T. (2005), "Numerische Behandlung gewöhnlicher und partieller Differenzialgleichungen", ISBN 3-540-29867-3, Springer, Heidelberg, Germany
- [60] Nevalainen, T., Johnstone, C., Grant, A. (2015), "An Unsteady Blade Element Momentum Theory for Tidal Stream Turbines with Morris Method Sensitivity Analysis", 11<sup>th</sup> European Wave and Tidal Energy Conference, EWTEC 2015, Nantes, France

- 
- [61] Newman, J. (1977), "Marine Hydrodynamics", ISBN 978-0-262-14026-3, The MIT Press, USA
- [62] Nicholls-Lee, R. (2011), "Adaptive Composite Blades for Horizontal Axis Tidal Turbines", PhD-Thesis, University of Southampton, England
- [63] National Oceanic and Atmospheric Administration (NOAA), Center for Operational Oceanographic Products and Services (2015), website: <http://tidesandcurrents.noaa.gov>
- [64] National Renewable Energy Laboratory (NREL), Office of Energy Efficiency and Renewable Energy (2015), "TurbSim", website: [nwtc.nrel.gov/TurbSim](http://nwtc.nrel.gov/TurbSim)
- [65] Oberkampf, W., Trucano, T. (2002), "Verification and Validation in Computational Fluid Dynamics", SAND2002-0529, Albuquerque, USA
- [66] Oka, S., Ishihara, T. (2009), "Numerical study of aerodynamic characteristics of a square prism in a uniform flow", Journal of Wind Engineering and Industrial Aerodynamics, Vol. 97, No. 11, pp. 548-559
- [67] OpenHydro Group Ltd. (2016), website: [www.openhydro.com](http://www.openhydro.com)
- [68] Pang, A., Skote, M., Lim, S.Y. (2013), "Turbulence Modeling Around Extremely Large Cylindrical Bluff Bodies", 23<sup>rd</sup> International Ocean and Polar Engineering Conference, ISOPE 2013, Anchorage, USA
- [69] Pitt, D., Peters, D. (1983), "Rotor dynamic inflow derivatives and time constants from various inflow models", 9<sup>th</sup> European Rotorcraft Forum, Stresa, Italy
- [70] Pugh, D. (1987), "Tides, Surges and Mean Sea-Level", ISBN 0-471-91505-X, John Wiley & Sons, Great Britain
- [71] Ruopp, A., Daus, P., Ruprecht, A., Riedelbauch, S. (2013), "A Two-Dimensional Finite Volume Shallow Water Model for Tidal Current Simulations Using OpenFOAM – Numerical Validation and High-Resolution Ocean Modelling Case", 10<sup>th</sup> European Wave and Tidal Energy Conference, EWTEC 2013, Aalborg, Denmark
- [72] Robertson, A. (2015), "Introduction to the OC5 Project, an IEA Task Focused on Validating Offshore Wind Modelling Tools", 12<sup>th</sup> EERA DeepWind'2016, Trondheim, Norway
- [73] Robertson, A., et.al. (2014), "Offshore Code Comparison Collaboration Continuation Within IEA Wind Task 30: Phase II Results Regarding a Floating Semisubmersible Wind System", 33<sup>rd</sup> International Conference on Ocean, Offshore and Arctic Engineering, OMAE 2014, San Francisco, USA
- [74] Santos, L., Avila, S., Shzu, M., Morais, M., Pereira, W. (2013), "Structural Control of wind turbine tower using a tuned mass damper via finite element method", 2013 ESSS Conference & Ansys Users Meeting, Atibaia, Brasil
- [75] Schaper, U. (2015), "Schwingungsdämpfende Regelung der Pendel- und Schwenkdynamik von Hafenmobilkranen", PhD-Thesis, University Stuttgart, Germany, ISBN 978-3-8440-3519-3

- [76] Simms, D., Schreck, S., Hand, M., Fingersh, L.J. (2001), "NREL Unsteady Aerodynamics Experiment in the NASA Ames Wind Tunnel: A Comparison of Predictions to Measurements", NREL/TP-500-29494, Colorado, USA
- [77] Simpack (2013), "Simpack Assistant 9.4 - Documentation", Gilching, Germany
- [78] Sohankar, A., Norberg, C., Davidson, L. (1998) "Low Reynolds Number Flow Around a Square Cylinder at Incidence: Study of Blockage, Onset of Vortex Shedding and Outlet Boundary Condition", *International Journal for Numerical Methods in Fluids*, Vol. 26, No. 1, pp. 39-56
- [79] Starzmann, R., Baldus, M., Groh, E., Lange, N. A., Scholl, S. (2013), "Full-Scale Testing of a Tidal Energy Converter Using a Tug Boat", 10<sup>th</sup> European Wave and Tidal Energy Conference, EWTEC 2013, Aalborg, Denmark
- [80] Streiner, S. (2010), "Beitrag zur numerischen Simulation der Aerodynamik und Aeroelastik großer Windkraftanlagen mit horizontaler Achse", PhD Thesis, University Stuttgart, Germany
- [81] Tatum, S.C., Frost, C.H., Allmark, M., O'Doherty D.M. Mason-Jones, A., Prickett P.W. Grosvenor, R.I., Byrne, C.B. O'Doherty T. (2015), "Wave-current interaction effects on tidal stream turbine performance and loading characteristics", *International Journal of Marine Energy*, <http://dx.doi.org/10.2016/j.ijome.2015.09.002>
- [82] Tsalicoglou, C., Jafari, S., Chokani, N., Abhari, R. (2013), "RANS Computations of MEXICO Rotor in Uniform and Yawed Inflow", *Journal of Engineering for Gas Turbines and Power*, Vol. 136, No. 1,
- [83] Turek, S., Hron, J. (2006), "Proposal for Numerical Benchmarking of Fluid-Structure Interaction Between an Elastic Object and Laminar Incompressible Flow", *Fluid-Structure Interaction: Modelling, Simulation, Optimization, Lecture Notes in Computational Science and Engineering*, Vol. 53, pp. 371-385
- [84] Voith Hydro Ocean Current Technologies GmbH & Co. KG (2015), website: [www.voith.com](http://www.voith.com)
- [85] Voith Hydro Ocean Current Technologies GmbH & Co. KG (2012), "Load analysis EMEC design loads c003 velocity 3.0 m/s (shut-off criteria)", Voith internal report 0478-03
- [86] Voith Hydro Ocean Current Technologies GmbH & Co. KG (2015), "EMEC Load Assessment EMEC01", Voith internal report 2-01052203
- [87] Waugh, J., Ellis, A. (1969), "Fluid-Free-Surface Proximity Effect on a Sphere Vertically Accelerated from Rest", *Journal of Hydronautics*, Vol. 3, No. 4, pp. 175-179
- [88] Ye, L., Yi-Hsiang, Y. (2012), "A Synthesis of Numerical Methods for modeling Wave Energy Converter-Point Absorbers", NREL/JA-5000-52115, Colorado, USA

- [89] Zarraonandia, G., Bittencourt, C. (2016), "Identification of the Uncertainties for the Calibration of the Partial Safety Factors for Load in Tidal Turbines", *Journal of Marine Science and Engineering*, Vol. 4, No. 1, paper 20
- [90] Zierath, J., Rachholz, R., Woernle, C., Müller, A. (2014), "Load Calculation on Wind Turbines: Validation of Flex5, Alaska/Wind, MSC.Adams and Simpack by means of Field Tests", 2014 ASME International Design Engineering Technical Conferences & Computers and Information in Engineering Conference, Buffalo, USA





---

## LIST OF PUBLICATIONS

The present thesis is based on the author's research during his time at the Stuttgart Wind Energy (SWE) and within the research project 'Voith Tidal Hydroelasticity'. Parts of this research and of the results have been published previously in journals and on conferences. A list of these publications is given below.

- [A 1] Arnold, M., Biskup, F., Cheng, P.W. (2015) "Load Reduction Potential of Variable Speed Control Approaches for Fixed Pitch Tidal Current Turbines", *International Journal of Marine Energy, IJOME*, doi: 10.1016/j.ijome.2016. 04.012 (presented at EWTEC 2015)
- [A 2] Arnold, M., Biskup, F., Cheng, P.W. (2015) "Impact of Structural Flexibility on Loads on Tidal Current Turbines", Accepted by *International Journal of Marine Energy, IJOME* (presented at EWTEC 2015)
- [A 3] Arnold, M., Kretschmer, M., Biskup, F., Koch, J., Cheng P.W. (2015) "A Validation Method for Fluid-Structure-Interaction Simulations Based on Submerged Free Decay Experiments" , *Journal of Ocean and Wind Energy, JOWE*, Vol. 2 No. 4 November 2015, pp. 202-212 (presented at ISOPE 2015)
- [A 4] Arnold, M., Biskup, F., Cheng, P.W. (2015) "Impact of Structural Flexibility on Loads on Tidal Current Turbines", 11<sup>th</sup> European Wave and Tidal Energy Conference, EWTEC 2015, Nantes, France
- [A 5] Arnold, M., Biskup, F., Cheng, P.W. (2015) "Load Reduction Potential of Variable Speed Control Approaches for Fixed Pitch Tidal Current Turbines", 11<sup>th</sup> European Wave and Tidal Energy Conference, EWTEC 2015, Nantes, France
- [A 6] Arnold, M., Kretschmer, M., Biskup, F., Koch, J., Cheng P.W. (2015) "A Validation Method for Fluid-Structure-Interaction Simulations Based on Submerged Free Decay Experiments", 25<sup>th</sup> International Ocean and Polar Engineering Conference, ISOPE 2015, Kona, USA
- [A 7] Biskup, F., Arnold, M., Daus, P., Engbroks, L. (2015) "Actuator Disc Model of a Tidal In-Stream Energy Converter – Voith HyTide", 25<sup>th</sup> International Ocean and Polar Engineering Conference, ISOPE 2015, Kona, USA
- [A 8] Moisel, C., Carolus, T., Banzhaf, H.-U., Biskup, F., Arlitt, R., Arnold, M. (2015) "Air Turbine for using Energy from Sea", European Patent, No. 13796060.5-1610
- [A 9] Arnold, M., Daus, P., Biskup, F., Cheng, P.W. (2014) "Tidal Current Turbine Wake and Park Layout in transient Environments", ASME 33<sup>rd</sup> International Conference on Ocean, Offshore and Arctic Engineering, OMAE 2014, San Francisco, USA

- [A 10] Arnold, M., Biskup, F., Cheng, P.W. (2014) "Simulation of Fluid-Structure-Interaction on Tidal Current Turbines based on coupled Multibody and CFD Methods", Journal of Ocean and Wind Energy, JOWE, Vol. 1 No. 2 May 2014, pp. 119-126 (presented at ISOPE 2013)
- [A 11] Markus, D., Arnold, M., Wüchner, R., Bletzinger, K.-U. (2014) "A Virtual Free Surface (VFS) Model for efficient wave-current CFD simulations of fully submerged structures", Journal of Coastal Engineering, JSCE, Vol. 89, pp. 95-98
- [A 12] Beyer, F., Arnold, M., Cheng, P.W. (2014) "Simulation of Ocean Waves for Load Assessment of Surface Piercing and Fully Submerged Bodies with Ansys CFX", 32<sup>nd</sup> Ansys Customer and User Meeting, ACUM 2014, Nuernberg, Germany
- [A 13] Beyer, F., Matha, D., Arnold, M., Luhmann, B., Cheng, P.W. (2014) "Coupled CFD and Vortex Methods for Modelling Hydro- and Aerodynamics of Tidal Current Turbines and On- and Offshore Wind Turbines", Simpack User Meeting 2014, Augsburg, Germany
- [A 14] Arnold, M., Biskup, F., Cheng, P.W. (2013) "Simulation of Fluid-Structure-Interaction on Tidal Current Turbines based on coupled Multibody and CFD Methods", 23<sup>rd</sup> International Ocean and Polar Engineering Conference, ISOPE 2013, Anchorage, USA
- [A 15] Arnold, M., Biskup, F., Matha, D., Cheng, P.W. (2013) "Simulation of Rotor-Foundation-Interaction on Tidal Current Turbines with Computational Fluid Dynamics", 10<sup>th</sup> European Wave and Tidal Energy Conference, EWTEC 2013, Aalborg, Denmark
- [A 16] Arnold, M., Cheng, P.W. (2013) "Simulation of Fluid-Structure-Interaction on Tidal Current Turbines with flexible Multibody Systems and Ansys CFX", 31<sup>st</sup> Ansys Customer and User Meeting, ACUM 2013, Mannheim, Germany
- [A 17] Beyer, F., Arnold, M., Cheng, P.W. (2013) "Analysis of Floating Offshore Wind Turbine Hydrodynamics using coupled CFD and Multibody Methods", 23<sup>rd</sup> International Ocean and Polar Engineering Conference, ISOPE 2013, Anchorage, USA
- [A 18] Markus, D., Wüchner, R., Arnold, M., Bletzinger, K.-U., Hojjat, M. (2013) "a reduced modeling Methodology for efficient Ocean Wave CFD Simulation of fully submerged Structures", ASME 32<sup>nd</sup> International Conference on Ocean, Offshore and Arctic Engineering, OMAE 2013, Nantes, France
- [A 19] Biskup, F., Arnold, M., Daus, P., Arlitt, R., Hohberg, M. (2013) "Effects of Rotor Blade Tip Modifications on a Tidal In-Stream Energy Converter – Voith HyTide", 10<sup>th</sup> European Wave and Tidal Energy Conference, EWTEC 2013, Aalborg, Denmark
- [A 20] Arnold, M., Cheng, P.W. (2012) "Fluid-Structure-Interaction on Tidal Current Turbines", 8<sup>th</sup> PhD Seminar on Wind Energy in Europe, Zürich, Swiss

## LIST OF FIGURES

Fig. 1-1: Spectrum of the absolute value of current velocity $u_{current}$ sketched (left) and based on measured data from the Fino 1 met mast, [20] (period: 02.2004–12.2006, resolution: 10 minutes, missing data interpolated)	2
Fig. 2-1: Lunar tide (grey) and solar tide (white) due to earth-moon-sun alignment	7
Fig. 2-2: Co-tidal map of Atlantic ocean, [62], and tidal data for three exemplary locations for 1 <sup>st</sup> till 7 <sup>th</sup> Nov 2015, reproduced from [63]	8
Fig. 2-3: Current velocity in Fall of Warness, Orkney, from simulation (left), [71], and aerial view on Muckle Green Holm Island in south-east of simulation (right), [28]	10
Fig. 2-4: Stream tube model of axial velocities ahead, $v_1$ , in the rotor disc, $v_2$ , and far behind, $v_3$ , (left) and airfoil theory for lifting rotor blades (right)	12
Fig. 2-5: Examples for tidal current turbine devices – Voith HyTide <sup>®</sup> 110 (left), [84], OpenHydro (middle), [67], and BlueTEC (right), [17]	12
Fig. 2-6: Fish swarm approaching the nacelle of the Voith HyTide <sup>®</sup> 1000-13 tidal current turbine at EMEC during operation with $n \approx 8.1rpm$ to feed from the marine growth, [84], Sept. 2014	15
Fig. 2-7: Number of tidal current turbine technologies for different types of turbines, reproduced from [49]	17
Fig. 2-8: CAD image of Voith HyTide <sup>®</sup> 1MW tidal current (left, [84]) and conceptual sketch of turbine (right)	18
Fig. 3-1: Slender body theory applied to an ellipsoid perpendicular to main axis	23
Fig. 3-2: Comparison of DNS, RANS and URANS on an artificial velocity time series	25
Fig. 3-3: Basic structure of the FMBI coupling code	30
Fig. 3-4: Data flow structure of time step iterations	31
Fig. 3-5: Surface mapping strategy from FEM (tetra) to CFD (quad) grid (left) and spline interpolation method (right)	34
Fig. 3-6: Change of angle between adjacent objects with different spline definitions under deformation	36
Fig. 3-7: Mapping strategy for interconnecting beam-shaped objects	38

Fig. 3-8: Relative error $\varepsilon$ due to change in relative position of associated communication markers and surface regions on a cantilever beam example (left: $n_{marker} = 2$ )	39
Fig. 3-9: Workflow of moderator script in FMBI coupling	41
Fig. 3-10: Experimental setup for pendulum experiments	45
Fig. 3-11: Validation procedure based on the free decay pendulums and detected location of bugs in case of deviation	46
Fig. 3-12: Image of experimental setup for spring pendulum (left) and bending pendulum (right) in air (basin not yet filled with water)	47
Fig. 3-13: Sketch of the experimental setups for validation (not to scale)	48
Fig. 3-14: Surface deviation $\Delta$ from design geometry of pendulum objects	49
Fig. 3-15: Image processing steps for optical measurement system	50
Fig. 3-16: Grid for spring and gravity pendulum	51
Fig. 3-17: Comparison of the spring pendulum position $x$ , normalized with the initial amplitude, (left) and the gravity pendulum position $\varphi$ (right) between experiment and simulation	54
Fig. 3-18: Comparison of the tip displacement $x$ of the bending pendulum between experiment and simulation	55
Fig. 4-1: Sketch of global grid topology	60
Fig. 4-2: Turbine grid (top) and close up views to the blade and blade tip grid (bottom)	61
Fig. 4-3: Sketch of artificial added mass instability in an explicit coupled simulation	63
Fig. 4-4: Sketch of the MBS model topology (left) and visualization of the tidal turbine in Simpack (right)	65
Fig. 4-5: Sketch of the interpolation system (left) and surface discretization of the CFD grid (right)	66
Fig. 4-6: Turbine power $P$ and tip speed ratio $\lambda_{TSR}$ over normalized current velocity $v_1$	68
Fig. 4-7: Normalized current velocity on the turbine mid plane for luv (top) and lee (bottom) operation at $v_1 = 2.2m/s$ , $\lambda_{TSR} = \lambda_{TSR\ opt}$	70
Fig. 4-8: Normalized current velocity on turbine mid plane for luv (top) and lee (bottom) operation at $v_1 = 4m/s$ , $\lambda_{TSR} = 2 \cdot \lambda_{TSR\ opt}$	71
Fig. 4-9: Swirl deflected transition piece wake in side (left) and rear view (right)	72

Fig. 4-10: Horseshoe vortex origin at tower-nacelle connection in side (left) and rear view (right)	72
Fig. 4-11: Rotor inflow velocity field 5m after tower center in front view	72
Fig. 4-12: Blade thrust coefficient $c_{th\ blade}$ during revolution in lee operation	73
Fig. 4-13: Impact of numerical, spatial and temporal resolution on the blade thrust coefficient $c_{th\ blade}$ (left) and on corresponding amplitude $\Delta c_{th\ blade}$ spectrum (right)	75
Fig. 4-14: Fully flexible turbine in motion colored by displacement	77
Fig. 4-15: Tower top motion over time, case V (Table 4-3)	78
Fig. 4-16: Axial hub force $F_{x\ Hub}$ with varying drivetrain flexibility normalized with mean value $\bar{F}_{x\ Hub} _{rigid}$	80
Fig. 4-17: Hub torque $Q_{x\ Hub}$ with varying drivetrain flexibility normalized with mean value $\bar{Q}_{x\ Hub} _{rigid}$	81
Fig. 4-18: Tower bottom bending moment $M_{y\ TowerBottom}$ with varying drivetrain flexibility normalized with mean value $\bar{M}_{y\ TowerBottom} _{rigid}$	82
Fig. 4-19: Axial hub Force $F_{x\ Hub}$ (left) and tower bottom bending moment $M_{y\ TowerBottom}$ with varying blade structural flexibility normalized with mean value $\bar{F}_{x\ Hub} _{rigid}$ and $\bar{M}_{y\ TowerBottom} _{rigid}$ respectively	83
Fig. 4-20: Hub torque $Q_{x\ Hub}$ with varying fixed-structure flexibility normalized with mean value $\bar{Q}_{x\ Hub} _{rigid}$	84
Fig. 4-21: Axial hub force $F_{x\ Hub}$ with varying fixed-structure flexibility normalized with mean value $\bar{F}_{x\ Hub} _{rigid}$	84
Fig. 4-22: Axial tower top load $F_{x\ TowerTop}$ with varying fixed-structure flexibility normalized with mean value $\bar{F}_{x\ TowerTop} _{rigid}$	85
Fig. 4-23: Tower top torsional load $Q_{z\ TowerTop}$ with varying fixed-structure flexibility normalized with mean value $\bar{Q}_{z\ TowerTop} _{rigid}$	86
Fig. 4-24: Tower bottom bending moment $M_{y\ TowerBottom}$ with varying fixed-structure flexibility normalized with mean value $\bar{M}_{y\ TowerBottom} _{rigid}$	87
Fig. 4-25: Amplitude response ratio $A/A_0$ of tower bottom bending moment $M_{y\ TowerBottom}$ to excitation ratios $f/f_{tower}$	88
Fig. 4-26: Tower bottom bending moment $M_{y\ TowerBottom}$ for $\lambda_{TSR} = 2 \cdot \lambda_{TSR\ opt}$ in fully flexible (dashed) and rigid (solid) setup normalized with the corresponding mean values $\bar{M}_{y\ TowerBottom} _{rigid}(v_1)$	89

- Fig. 4-27: Axial tower top load  $F_{x\ TowerTop}$  (left) and axial hub force  $F_{x\ Hub}$  (right) for  $\lambda_{TSR} = 2 \cdot \lambda_{TSR\ opt}$  in fully flexible (dashed) and rigid (solid) setup normalized with the corresponding mean values 89
- Fig. 4-28: Linear deceleration of rotational speed for passage of resonance 91
- Fig. 4-29: Tower bottom bending moment  $M_{y\ TowerBottom}$  (left) and axial tower top load  $F_{x\ TowerTop}$  (right) during passage of resonance normalized with the corresponding mean values at  $t > 6s$  91
- Fig. 4-30: Response of hub torque  $Q_{x\ Hub}$  to deceleration of generator rotational speed normalized with the mean value at  $t > 6s$  92
- Fig. 5-1: Load amplitude response ratio (left) through a spring-mass-damper-system (right) with varying damping ratios  $0.1 \leq \zeta \leq 1$  in logarithmic row 95
- Fig. 5-2: 2-dimensional simulation results for the time averaged wake velocity  $u$  with  $v_1 = 4m/s$  of four different transition piece cross-sections each shown as half field 99
- Fig. 5-3: Steady operation for the overspeed and underspeed controller in the rotor performance curve with an exemplary set point (left) and the generator set point curve (right) 102
- Fig. 5-4: Cascaded structure of underspeed controller 103
- Fig. 5-5: Set point transfer function  $G_{Q_{el} \rightarrow \Omega_{req}}$  resolved 105
- Fig. 5-6: Pole location of  $A_O$  colored by  $T_{PT_1}$  for an arbitrary above rated point of operation (left) and minimal required value of  $T_{PT_1}$  for stable operation (right) 106
- Fig. 5-7: Step response to an current speed increase  $3.5 \rightarrow 3.6\ m/s$  at  $t = 0s$  for  $T_{PT_1} = 1.25s$  (solid),  $1.5s$  (dashed) and  $2s$  (dotted) 107
- Fig. 5-8: Block diagram of turbine model for controller simulations 108
- Fig. 5-9: Mean hydrodynamic thrust force  $F_{Hydro}$  (solid) with damage equivalent load  $\pm DEL(F_{Hydro})$  (error bars,  $m = 4$ ,  $N_{ref} = 2e6$ ) and peak loading (x) 109
- Fig. 5-10: Mean hydrodynamic torque  $Q_{Hydro}$  (left) and mean electrical power  $P_{el}$  (right) with damage equivalent load  $\pm DEL(Q_{Hydro})$  (error bars,  $m = 4$ ,  $N_{ref} = 2e6$ ) resp. standard deviation  $\pm \sigma(P_{el})$  and peak loading (x) 110
- Fig. 5-11: Divisions responsible to deal with turbulence based on the controller concept 111

---

Fig. 5-12: Mass reduction due to change in controller concept from overspeed to underspeed dependent on mass fraction of system and changes in ultimate loads	112
Fig. 5-13: Simulation of partial stall (left), full stall (middle) and deep stall (right) for NACA0018 airfoil with $Re = 1e6$ in air and SAS turbulence model	113
Fig. 5-14: Iso-view on vortex structures on suction side of rotor blade during underspeed operation	114
Fig. 5-15: Blade tip displacement $\Delta x_{tip}$ for $v_1 = 4m/s$ at different tip speed ratios $\lambda_{TSR}$	115
Fig. 5-16: Time series (left) and spectrum (right, later 4s) of blade root thrust force coefficient $c_{th\ root}$ for $v_1 = 4m/s$ and $\lambda_{TSR} = \lambda_{TSR\ opt}/2$	115
Fig. A-1: Selected junctionbox locations in CFX (Figure reproduced and simplified from [5])	141
Fig. A-2: Workflow of moderator script in FMBI coupling	143
Fig. B-1: Sketch of blending scheme for prescribed deformation $\Delta x_{blended}$ in rotor domain	146





---

## LIST OF TABLES

Table 2-1: Summary of Voith HyTide <sup>®</sup> tidal current turbine concept	19
Table 2-2: Voith HyTide <sup>®</sup> 1000-13 turbine data	19
Table 3-1: List of validation experiments	45
Table 3-2: Standalone added mass validation results for CFX	53
Table 3-3: Standalone drag validation results for CFX with Reynolds number $Re = 200$	53
Table 4-1: List of MBS-model components	64
Table 4-2: Matrix of points of operation for the simulation of rotor-foundation- interaction	68
Table 4-3: Number of Eigenmodes in each simulated combination	79
Table A-1: List of FMBI communication files	140
Table A-2: File Header for the *.cfx2spck and *.spck2cfx files	140
Table A-3: List of FMBI-UserFortran routines	142



## APPENDIX A) DETAILS ON THE IMPLEMENTATION OF THE FMBI

The following appendix presents further details on the implementation of the FMBI coupling in CFX and Simpack. This is still limited here to the structure of the code. The full details of the implementation are part of the codes and the code documentation.

### Transfer Memory

As defined in the main body of the thesis, the transfer memory is based on files either on a physical or virtual hard drive. The data is thereby split into five files as shown in Table A-1. Each filename starts with an identification string used to determine whether a file belongs to the current simulation or not. Within the simulation, each file is then identified by the 2<sup>nd</sup> part of the filename.

While the two `*.ready` files are empty files transferring information by their existence, the `*.cfx2spck` and `*.spck2cfx` files are the data carriers. Each of those files is used unidirectional. After each coefficient loop of CFX, the fluid loads are written to the `*.cfx2spck` file. During that step the structural side of the simulation is in a pause waiting for the `*.cfxready` file, which is written after the `*.cfx2spck` file has been closed. The moderator then adapts the loads for relaxation, acknowledges this by deleting the `*.cfxready` file and starts the Simpack integrator. The integrator reads the new loads from the `*.cfx2spck` file and the file `*.cfx2spck_t_minus_1`, which is a copy of the converged result of the previous time step required for interpolation of the loads for the inner integrator time steps. After finishing the integration, Simpack outputs the `*.spck2cfx` and the `*.spckready` file is generated to give CFX the clearance for the next coefficient loop, which is acknowledged by deleting the `*.spckready` file.

Each data carrier file consists of single line ASCII data values. Those data values form two blocks: A 10-line header, and a data field containing the communicated data. As shown in Table A-2 the header contains information relevant for the simulation control. The data block consists of six lines per marker containing the forces  $F_x, F_y, F_z$  and moments  $Q_x, Q_y, Q_z$  in case of the `*.cfx2spck` file and the translations  $\Delta x, \Delta y, \Delta z$  and rotations  $\alpha, \beta, \gamma$  respectively in case of the `*.spck2cfx` file.

Table A-1: List of FMBI communication files

No.	Filename	Responsible coupling partner
1	*.cfx2spck	CFX (Moderator adds relaxation)
2	*.cfxready	CFX
3	*.spck2cfx	Simpack
4	*.spckready	Simpack
5	*.cfx2spck_t_minus_1	Moderator

Table A-2: File Header for the \*.cfx2spck and \*.spck2cfx files

Line	*.cfx2spck	*.spck2cfx
1	Flag for status (1: ok, -1: error )	
2	Current time value $t$	
3	Number of time step $n_{current\ time\ step}$	
4	Simulation time step	Communication time step
5	Number of coefficient loop $n_{coeff\ loop}$	Always 1.0
6	Flag for predictor corrector method (used during development)	
7-10	Reserved for future developments	

### CFX-UserFortran

CFX is a closed code dedicated to be used in industry without custom changes to the code. However, there are two interfaces in CFX for application of custom codes (UserFortran), which are used to implement the present coupling: The command expression language (CEL) functions, which are evaluated during the solution step on each element of the grid, and junctionbox routines, which can be executed at different locations within the solver process, Fig. A-1. Both types of UserFortran functions have access to the memory management system (MMS), a virtual filesystem containing the RAM of the solver run. Based on these options the coupling needs to be split into a total of four routines each with a specific location as listed in Table A-3.

All communications are pooled in the first junctionbox routine. At the beginning of each coefficient loop this routine sends the loads measured at the previous coefficient loop to the structural solver and awaits the new deformations to store them in the MMS. This routine is

executed in case of a parallel run only on the master partition, however CFX automatically synchronizes the data stored in the MMS after this junctionbox location is finished. The CEL function is executed on each parallel partition and calculates the local surface deformation with the spline based interpolation. Also, this routine is used to transmit requested data to the monitoring process of the CFX solver. After the coefficient loop has finished, the 3<sup>rd</sup> routine integrates the hydrodynamic loads with the build-in functions of CFX. Those functions are executed on each partition of the parallel solver run and automatically synchronize the calculated results over the parallel environment. The loads are then stored in the MMS to be send out to Simpack on the start of the next coefficient loop.

The 4<sup>th</sup> routine runs only once at the end of a simulation to stop the coupled solver system.

Special attention was required to the convergence process. CFX monitors the convergence of the fluid solver and jumps to the next time step, or ends the solver run based on the residual value respectively. However, this is only the residual of the fluid and a converged fluid solution does not necessarily involve a converged coupling solution. Therefore, the internal convergence indicators of CFX are overwritten by the communication junctionbox, based on the header values received from the moderator.

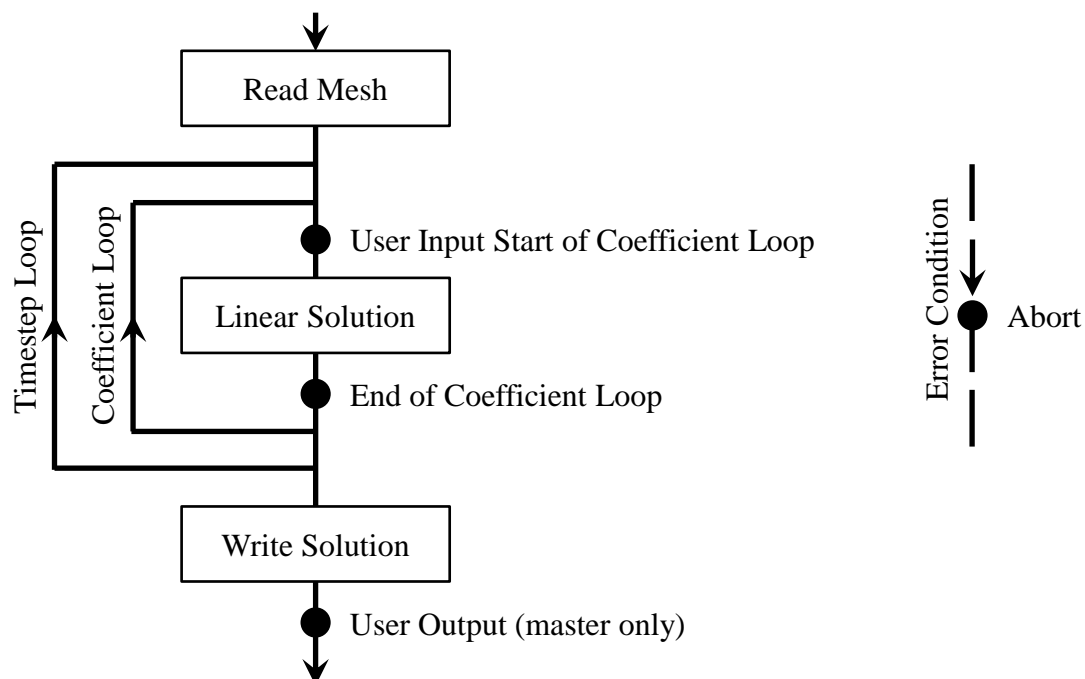


Fig. A-1: Selected junctionbox locations in CFX (Figure reproduced and simplified from [5])

Table A-3: List of FMBI-UserFortran routines

No.	Function	Type	Location
1	Sending and receiving data	Junctionbox	“User input start of coefficient loop”
2	Spline based interpolation	CEL	During solution on grid locations
3	Integration of loads	Junctionbox	“End of coefficient loop”
4	Abort of simulation	Junctionbox	“Abort”, “User output”

### **Simpack-UForce**

Simpack is similar to CFX a closed code, but also offers an interface for user specified Fortran code. These UForce functions are treated by Simpact as additional force elements applied to the system. The UForce is therefore repeatedly evaluated during each inner integration step. The operation during the time integration is split in three parts. If the UForce is called first time on the beginning of the integration the hydrodynamic loads at the start (\*.cfx2spck\_t\_minus\_1) and end of the time step (\*.cfx2spck) are read from the communication interface. On the following calls, the applied load is interpolated according to the time value and transformed with the structural translator, as defined in Section 3.2.3. At the last call of the UForce, the deformations are measured and send to the coupling.

For applying the load to the system, a standard function (SPCK\_DV\_ForceAtMarker) for the UForce is prepared by Simpact. However, this function showed some issues in some Versions of Simpact in combination with flexible bodies with 0 modes active and 0-DoF-joints calculating wrong joint loads. Therefore, the applied loads are output in the present implementation to the outvalues of the UForce intended for monitoring and applied with secondary force elements to the system. Theoretically, this is the same, but it prevents the mentioned bug on the cost of increased effort for setting up the model.

### **Moderator-Script**

The moderator is the heart of the coupling and controls the procedure and convergence. It is written as a Perl-script. As shown in Fig. A-2 the moderator script contains two loops: One for the relaxation of the implicit solution within each time step, and one for the transient simulation. Both operations are based on reading, interpreting and modifying the files in the transfer memory, which can be implemented straight forward in the Perl syntax.

Besides its tasks during the coupled simulation run, the moderator script also stores copies of all converged time step communications during the simulation. Those are used to perform a final Simpack integration ranging over the full time span of the coupled simulation, when it is stopped. This is not relevant for the coupled simulation itself, but gives the advantage of a single result file from Simpack for post processing instead of one result file per time step.

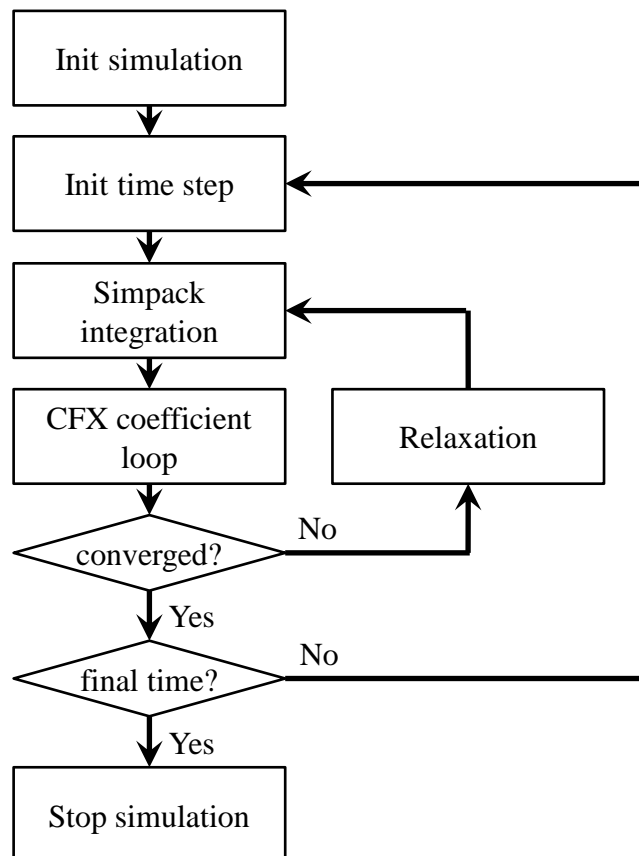


Fig. A-2: Workflow of moderator script in FMBI coupling





## APPENDIX B) DERIVATION OF EQUATIONS

Within this appendix the derivation of some equations is shown, which are only sketched in the main body of the thesis.

### Interpolation Scheme for Prescribed Rotor Grid Deformation

The build-in grid deformation algorithms of Ansys CFX are not able to calculate the grid deformations correctly for large rotational displacements of the rotor. Such large rotational displacements occur, e.g., for the simulation with a variable rotor speed, which is described as a relative motion to a fixed baseline rotational speed. Thus, to prevent a folded, invalid grid in the simulation of the transient resonance riding-through, Section 4.4.2, it is required to interpolate the deformations for the volume grid of the rotor domain from the FMBI deformation data for the nacelle,  $\Delta\vec{x}_N$ , the spinner and hub,  $\Delta\vec{x}_S$ , the three rotor blades,  $\Delta\vec{x}_{B1} \dots \Delta\vec{x}_{B3}$ , and the rotor rotation,  $\varphi_R$ . For this interpolation, blending schemes are introduced here, which define the area of impact for each communication spline set. Thus, for each of the deformations  $\Delta\vec{x}$  a weighting factor  $k$  is defined, which is limited to  $0 < k < 1$ .

First, the blending for the rotor blades and spinner system is applied, resulting in the deformations of the rotor system,  $\Delta\vec{x}_{SB}$ . For this blending, an elliptical distance from each blade,  $r_{B1 \dots 3}$ , at its angular position,  $\varphi_{01 \dots 3}$ , is defined, (B-1).

$$y_{Bn} = \cos(\varphi_{0n}) \cdot y - \sin(\varphi_{0n}) \cdot z$$

$$r_{Bn} = \begin{cases} \sqrt{2 \cdot (x - x_B)^2 + y_{Bn}^2} & 0 < \sin(\varphi_{0n}) \cdot y + \cos(\varphi_{0n}) \cdot z \\ \infty & else \end{cases} \quad (\text{B-1})$$

With this elliptical area, the blade deformations are then linearly blended to the spinner deformation in the range from  $r_{Bstart}$  to  $r_{Bend}$ , (B-2).

$$k_{Bn} = 1 - \frac{r_{Bn} - r_{Bstart}}{r_{Bend} - r_{Bstart}} \Big| 0 < k_{Bn} < 1$$

$$\Delta\vec{x}_{SB} = \sum_{n=1}^3 k_{Bn} \cdot \Delta\vec{x}_{Bn} + \left(1 - \sum_{n=1}^3 k_{Bn}\right) \cdot \Delta\vec{x}_S \quad (\text{B-2})$$

This combined deformation is then blended in the axial direction to the nacelle deformation,  $\Delta\vec{x}_N$ , across the gap between rotor and nacelle from  $x_{Gstart}$  to  $x_{Gend}$ , and to the rotor rotation,  $\varphi_R$ , from  $x_{Rstart}$  to  $x_{Rend}$ , (B-4). The latter is transferred here from the rotational

deformation of the spinner on the rotor axis,  $\varphi_R = \gamma_S = \Delta\vec{\alpha}_S(3)$ , and transformed to its deformation vector,  $\Delta\vec{x}_R$ , (B-3).

$$\Delta\vec{x}_R = \begin{bmatrix} 0 \\ y - (\cos(\varphi_R) \cdot y - \sin(\varphi_R) \cdot z) \\ z - (\sin(\varphi_R) \cdot y + \cos(\varphi_R) \cdot z) \end{bmatrix} \quad (\text{B-3})$$

$$k_N = 1 - \frac{x - x_{G \text{ start}}}{x_{G \text{ end}} - x_{G \text{ start}}} \Big| 0 < k_N < 1$$

$$k_{\varphi x} = \frac{x - x_{R \text{ start}}}{x_{R \text{ end}} - x_{R \text{ start}}} \Big| 0 < k_{\varphi x} < 1 \quad (\text{B-4})$$

$$\Delta\vec{x}_{N,SB,\varphi} = k_N \cdot \Delta\vec{x}_N + k_{\varphi x} \cdot \Delta\vec{x}_R + (1 - k_N - k_{\varphi x}) \cdot \Delta\vec{x}_{SB}$$

In the final blending step,  $\Delta\vec{x}_{N,SB,\varphi}$  is then blended in the radial direction to  $\Delta\vec{x}_R$  in the range from  $r_{start}$  to  $r_{end}$ , to result in the final deformation vector for the rotor domain  $\Delta\vec{x}_{blended}$ , (B-5).

$$k_r = \frac{\sqrt{y^2 + z^2} - r_{start}}{r_{end} - r_{start}} \Big| 0 < k_r < 1 \quad (\text{B-5})$$

$$\Delta\vec{x}_{blended} = k_r \cdot \Delta\vec{x}_R + (1 - k_r) \cdot \Delta\vec{x}_{N,SB,\varphi}$$

The resultant interpolation and blending scheme is sketched in Fig. B-1.

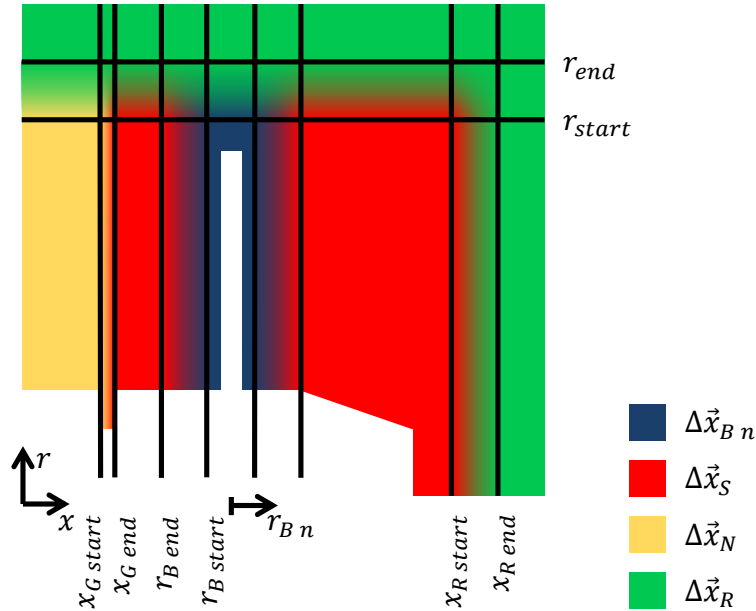


Fig. B-1: Sketch of blending scheme for prescribed deformation  $\Delta\vec{x}_{blended}$  in rotor domain

Due to the high number of spline operations for the evaluation of  $\Delta\vec{x}_{blended}$ , this scheme requires more resources than the build-in methods of CFX. However, the calculation of  $\Delta\vec{x}_{blended}$  is much more stable and thus suitable in cases the build-in methods can not handle.

## Hydrodynamic Damping

The hydrodynamic damping is introduced in Section 5.1.1.2. Within this appendix, the derivation of the critical values for  $dc_{th}/d\lambda_{TSR}|_{\zeta=0}$  and  $dc_l/d\alpha_{AoA}|_{\zeta=0}$  will be shown.

### Hydrodynamic Damping with $v_{fa} \ll v_1$

The critical value for the thrust curve slope  $dc_{th}/d\lambda_{TSR}|_{\zeta=0}$  is derived here from the definition of the thrust of a rotor, calculated by (B-6) with the structural fore-aft velocity of the rotor  $v_{fa}$ , the fluid density  $\rho$ , rotor radius  $R$  and current velocity  $v_1$ .

$$F_{th} = \frac{\rho}{2} \pi R^2 \cdot (v_1 + v_{fa})^2 \cdot c_{th} \quad (\text{B-6})$$

The thrust coefficient  $c_{th}$  depends on the relative tip speed ratio  $\lambda'_{TSR}$ , which is calculated with (B-7) from the rotor speed  $\Omega$ .

$$\lambda'_{TSR} = \frac{\Omega \cdot R}{v_1 + v_{fa}} \quad (\text{B-7})$$

With this definition the thrust coefficient curve  $c_{th}(\lambda_{TSR})$  is then linearized at the point of operation  $\lambda_{TSR}$ , (B-8), with the thrust curve slope  $dc_{th}/d\lambda_{TSR}$ . This linearization relies on the assumption of small motion velocities,  $v_{fa} \ll v_1$ , a constant rotor speed  $\Omega$  and quasi-static hydrodynamics,  $\partial c_{th}/\partial t = 0$ .

$$F_{th} = \frac{\rho}{2} \pi R^2 \cdot (v_1 + v_{fa})^2 \cdot \left( c_{th}|_{\lambda_{TSR}} + \left. \frac{dc_{th}}{d\lambda_{TSR}} \right|_{\lambda_{TSR}} \cdot (\lambda'_{TSR} - \lambda_{TSR}) \right) \quad (\text{B-8})$$

The critical value for a neutral hydrodynamic damping  $\zeta \rightarrow 0$  occurs for a constant thrust force independent of  $v_{fa}$ , (B-9).

$$F_{th} \neq f(v_{fa}) \Rightarrow F_{th}(v_1) = F_{th}(v_1 + v_{fa}) \quad (\text{B-9})$$

Thus, the thrust value with the velocity  $v_1$  is equal to the thrust value at  $v_1 + v_{fa}$ , (B-10).

$$\frac{\rho}{2}\pi R^2 \cdot v_1^2 \cdot c_{th}|_{\lambda_{TSR}} = \frac{\rho}{2}\pi R^2 \cdot (v_1 + v_{fa})^2 \cdot \left( c_{th}|_{\lambda_{TSR}} + \frac{dc_{th}}{d\lambda_{TSR}} \Big|_{\zeta=0} \cdot (\lambda'_{TSR} - \lambda_{TSR}) \right) \quad (\text{B-10})$$

With the abbreviation  $\tilde{v} = v_{fa}/v_1$ , this equation can be solved for  $dc_{th}/d\lambda_{TSR}|_{\zeta=0}$ .

$$c_{th}|_{\lambda_{TSR}} = (1 + \tilde{v})^2 \cdot \left( c_{th}|_{\lambda_{TSR}} + \frac{dc_{th}}{d\lambda_{TSR}} \Big|_{\zeta=0} \cdot \lambda_{TSR} \cdot \left( \frac{1}{1 + \tilde{v}} + 1 \right) \right) \quad (\text{B-11})$$

$$\frac{dc_{th}}{d\lambda_{TSR}} \Big|_{\zeta=0} = \frac{c_{th} \cdot ((1 + \tilde{v})^2 - 1)}{\lambda_{TSR} \cdot \tilde{v} \cdot (1 + \tilde{v})}$$

The value for  $dc_{th}/d\lambda_{TSR}|_{\zeta=0}$  decreases with increasing  $\tilde{v}$ . However, for small values of  $\tilde{v}$ , the critical value for the thrust curve slope  $dc_{th}/d\lambda_{TSR}$  can be derived by further eliminating the rotor fore-aft velocity with  $\lim_{\tilde{v} \rightarrow 0} (dc_{th}/d\lambda_{TSR}|_{\zeta=0})$ , (B-12).

$$\lim_{\tilde{v} \rightarrow 0} \frac{c_{th} \cdot ((1 + \tilde{v})^2 - 1)}{\lambda_{TSR} \cdot \tilde{v} \cdot (1 + \tilde{v})} = \frac{c_{th}}{\lambda_{TSR}} \cdot \lim_{\tilde{v} \rightarrow 0} \frac{\tilde{v} \cdot (2 + \tilde{v})}{\tilde{v} \cdot (1 + \tilde{v})} \quad (\text{B-12})$$

$$\frac{dc_{th}}{d\lambda_{TSR}} \Big|_{\zeta=0, \tilde{v} \rightarrow 0} = \frac{2 \cdot c_{th}}{\lambda_{TSR}}$$

### Hydrodynamic Damping with $v_{fa} \gg 0$

Similar to the previous derivation, the limiting value for the lift curve slope  $dc_l/d\alpha_{AoA}|_{\zeta=0}$  is derived from the basic definition of the forces on a rotor blade. With the assumption of a high local relative tip speed ratio  $\lambda'_{TSR} = \Omega \cdot r / (v_1 + v_{fa}) \gg 1$  and thus a small inflow angle  $\alpha_2 \rightarrow 0$ , (B-13), the thrust load  $F_{th}$  of a rotor section  $dr$  at radius  $r$  is approximately equal to the lift force  $F_l$ , (B-14) with the rotor speed  $\Omega$ .

$$\alpha_2 = \text{atan} \left( \frac{v_2 + v_{fa}}{\Omega \cdot r} \right) = \text{atan} \left( \frac{\tilde{v} - a + 1}{\lambda'_{TSR}} \right) \quad (\text{B-13})$$

$$F_{th} \approx F_l \cdot \cos(\alpha_2) \approx F_l \quad (\text{B-14})$$

The independency of the thrust load from the fore-aft velocity, used in the previous section, therefore can be translated into an independency of the lift force, (B-15). Taking also the dynamic inflow phenomenon and the inertia of the fluid into account, the induction factor  $a$  and thus the local velocity  $v_2$  can be approximated to be constant, (B-16).

$$F_{th} \approx F_l \cdot \cos(\alpha_2) \approx F_l \neq f(v_{fa}) \quad (\text{B-15})$$

$$v_2 = v_1 \cdot (1 - a) = \text{const} \quad (\text{B-16})$$

Applying those assumptions to the definition of the lift force  $F_l$  with the linearized lift curve, the equation for the critical value of the lift curve slope  $dc_l/d\alpha_{AoA}|_{\zeta=0}$  can be assembled, (B-17) with the fluid density  $\rho$  and chord length  $t_{chord}$ .

$$F_l = \frac{\rho}{2} t_{chord} dr \cdot (v_2^2 + (\Omega r)^2) \cdot c_l = \frac{\rho}{2} t_{chord} dr \cdot \left( (v_2 + v_{fa})^2 + (\Omega r)^2 \right) \cdot \left( c_l + \frac{dc_l}{d\alpha_{AoA}} \Big|_{\zeta=0} \cdot \left( \text{atan} \left( \frac{v_2 + v_{fa}}{\Omega \cdot r} \right) - \text{atan} \left( \frac{v_2}{\Omega \cdot r} \right) \right) \right) \quad (\text{B-17})$$

This equation can then be solved for the critical value of the lift curve slope  $dc_l/d\alpha_{AoA}|_{\zeta=0}$ , (B-18).

$$\frac{dc_l}{d\alpha_{AoA}} \Big|_{\zeta=0} = \frac{-\left(\tilde{v}^2 + 2 \cdot \tilde{v} \cdot (1 - a)\right) \cdot c_l}{\left(\text{atan} \left( \frac{\tilde{v} + 1 - a}{\lambda'_{TSR}} \right) - \text{atan} \left( \frac{1 - a}{\lambda'_{TSR}} \right)\right) \cdot \left((\tilde{v} - a + 1)^2 + \frac{1}{\lambda'_{TSR}{}^2}\right)} \quad (\text{B-18})$$

## Outer Closed-Loop Stability for Underspeed Controlled Operation

The derivation of the system equations for the underspeed controller's outer closed-loop is an extension of the derivation of the inner closed-loop's stability analysis, Section 5.2.2.1. To describe the system behavior, a linear set of differential equations  $\dot{\vec{z}} = \mathbf{A}_O \cdot \vec{z} + \vec{b}_O$  is set up, with the state vector  $\vec{z}$ , (B-19).

$$\dot{\vec{z}} = \left[ \int \Omega_{req} dt \quad \Omega_{req} \quad \int \Omega dt \quad \Omega \right]^T \quad (\text{B-19})$$

The requested rotational speed  $\Omega_{req}$  and the current rotational speed  $\Omega$  are the input and output of the inner closed-loop. The dynamics of the inner closed-loop therefore need to be translated into this set of variables for the PI-controller, (B-20), and the rotational DoF of the rotor, (B-21), with the PI-parameters  $k_p$  and  $k_I$ .

$$Q_{el} = k_p \cdot (\Omega - \Omega_{req}) + k_I \cdot \left( \int \Omega dt - \int \Omega_{req} dt \right) \quad (\text{B-20})$$

$$\dot{\Omega} = \frac{1}{J} \cdot \left( Q_{Hydro} \Big|_{\Omega_0} + k_{Q\Omega} \cdot (\Omega - \Omega_0) - Q_{el} \right) \quad (\text{B-21})$$

(B-21) includes the linearization of the rotor hydrodynamic torque  $Q_{Hydro}$  with the abbreviation  $k_{Q\Omega} = dQ_{Hydro}/d\Omega|_{\Omega_0}$  and the drivetrain inertia  $J$ . Inserting (B-20) to (B-21) results in the inner-closed loop characteristics, described by the variables of the state vector  $\vec{z}$ , (B-22).

$$\dot{\Omega} = \frac{1}{J} \cdot \left( Q_{Hydro}|_{\Omega_0} + k_{Q\Omega} \cdot (\Omega - \Omega_0) - k_p \cdot (\Omega - \Omega_{req}) + k_I \cdot \left( \int \Omega dt - \int \Omega_{req} dt \right) \right) \quad (\text{B-22})$$

The same procedure and linearization can be applied to the outer cascade, consisting of the set-point curve  $\Omega_{opt} = f(Q_{el})$ , (B-23), with the generator torque  $Q_{el}$ , the abbreviation  $k_{\Omega Q} = d\Omega_{opt}/dQ_{el}|_{\Omega_0}$  and the  $PT_1$ -lowpass filter, (B-24), with the time constant  $T_{PT_1}$ .

$$\Omega_{opt} = \Omega_{opt}|_{\Omega_0} + k_{\Omega Q} \cdot (Q_{el} - Q_{Hydro}|_{\Omega_0}) \quad (\text{B-23})$$

$$\dot{\Omega}_{req} = \frac{1}{T_{PT_1}} \cdot (\Omega_{opt} - \Omega_{req}) \quad (\text{B-24})$$

Inserting (B-20) and (B-23) to (B-24), then results in the description of the outer cascade based on the variables used for the state vector  $\vec{z}$ , (B-25).

$$\dot{\Omega}_{req} = \frac{1}{T_{PT_1}} \cdot \left( \Omega_{opt}|_{\Omega_0} + k_{\Omega Q} \cdot \left( k_p \cdot (\Omega - \Omega_{req}) + k_I \cdot \left( \int \Omega dt - \int \Omega_{req} dt \right) - Q_{Hydro}|_{\Omega_0} \right) - \Omega_{req} \right) \quad (\text{B-25})$$

Sorting (B-25) and (B-22) to the state vector variables, (B-19), then results in the system matrices according to the linear set of equations  $\dot{\vec{z}} = \mathbf{A}_O \cdot \vec{z} + \vec{b}_O$ , (B-26) – (B-27).

$$\mathbf{A}_O = \begin{bmatrix} 0 & 1 & 0 & 0 \\ -\frac{k_I}{T_{PT_1}} \cdot k_{\Omega Q} & -\frac{k_p \cdot k_{\Omega Q} + 1}{T_{PT_1}} & \frac{k_I}{T_{PT_1}} \cdot k_{\Omega Q} & \frac{k_p}{T_{PT_1}} \cdot k_{\Omega Q} \\ 0 & 0 & 0 & 1 \\ \frac{k_I}{J} & \frac{k_p}{J} & -\frac{k_I}{J} & \frac{k_p \cdot k_{Q\Omega}}{J} \end{bmatrix} \quad (\text{B-26})$$

$$\vec{b}_O = \begin{bmatrix} 0 \\ \frac{\Omega_{opt}|_{\Omega_0} + Q_{el}|_{\Omega_0} \cdot k_{\Omega Q}}{T_{PT_1}} \\ 0 \\ \frac{Q_{Hydro}|_{\Omega_0} - \Omega_0 \cdot k_{Q\Omega}}{J} \end{bmatrix} \quad (\text{B-27})$$

## CURRICULUM VITAE



### Matthias Arnold

Address: Wiesenstraße 15  
26603 Aurich, Germany  
Email: Arnold@ifb.uni-stuttgart.de  
Birthday: July 8<sup>th</sup> 1986 (Heidelberg)  
Nationality: German

#### Personal statement

I am an engineer and researcher partially finishing my PhD with the present document. My original field of expertise is the fluid dynamics, however I see myself as being an engineer understanding any system as the interaction of disciplines.

During all projects I trained my skills by analyzing the methods, issues and solutions of all disciplines contributing to the whole system. On this basis, I have a high ability in acquiring knowledge and find my way into new projects and topics fast. Despite an old cliché states 'knowledge is power', in my personal experience only upon sharing such knowledge in a team, great things can arise.

#### Professional and academic career

Since 08/2016      Wobben Research and Development GmbH  
(Aurich, Germany)

Positions:      Expert for system aerodynamics

Fields of Activity:      CFD and FSI simulations for wind turbines, system analysis for wind turbines, development of simulation models

01/2012 – 06/2016      Stuttgart Wind Energy (SWE) at University Stuttgart

Positions:      Researcher and PhD candidate

Fields of activity:      CFD, Multibody and FSI simulations, development of simulation methods, system analysis for wind and tidal current turbines, workshop supervisor, project management, teaching in lectures and tutorials

10/2008 – 11/2011      Voith Hydro Ocean Current Technologies GmbH & Co. KG  
(Heidenheim, Germany)

Positions:      Diploma thesis, student worker and internship

Fields of Activity:      CFD simulations for tidal current turbines and wave energy systems, development of analytical and numerical simulation models, controller development

10/2006 – 11/2011      University Stuttgart

Field of studies:      Aeronautics and space technology engineering